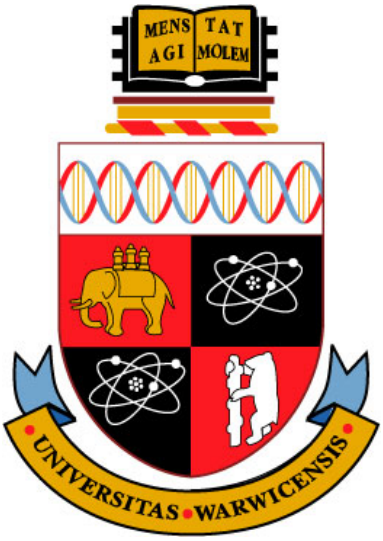

Quasi-periodic pulsations in solar flares

by

Andrew R. Inglis

Thesis

Submitted to the University of Warwick

for the degree of

Doctor of Philosophy

Physics Department

September 2009

THE UNIVERSITY OF
WARWICK

Contents

List of Figures

Acknowledgments

I would like to thank Prof. Valery Nakariakov for his support and supervision throughout the course of my PhD. Special thanks also go to Dr Tom Van Doorsselaere for many helpful discussions.

This thesis was typeset with LaTeX 2$_\varepsilon$[1] by the author.

[1] LaTeX 2$_\varepsilon$ is an extension of LaTeX. LaTeX is a collection of macros for TeX. TeX is a trademark of the American Mathematical Society. The style package *wnewthesis* was used.

Declarations

I declare that this thesis is my own work except where indicated. This thesis has not been submitted for a degree at another university. Some of the work presented in this thesis has also been published in the following peer-reviewed journal articles:

- A. R. Inglis, V. M. Nakariakov and V. F. Melnikov, Multi-wavelength spatially resolved analysis of quasi-periodic pulsations in a solar flare, A&A, 487, 1147-1153, 2008.
- A. R. Inglis and V. M. Nakariakov, A multi-periodic oscillatory event in a solar flare, A&A, 493, 259-266, 2009.
- A. R. Inglis, T. Van Doorsselaere, C. S. Brady and V. M. Nakariakov, Characteristics of magnetoacoustic sausage modes, A&A, 503, 569-575, 2009.

I would like to explicitly acknowledge the contribution of Dr T. Van Doorsselaere to the study of the cut-off wavenumber in Chapter 3, namely the result contained in Equation 3.15 and Figure 3.8. Also in Chapter 4 the radio data from the Nobeyama Radiopolarimeters shown in the bottom panel of Figure 4.1 was provided by Dr V. Melnikov.

Abstract

For several decades, quasi-periodic pulsations (QPP) in flares have been a signature feature of solar dynamics. In the last fifteen years, the advent of new observational instruments has led to a much-improved scope for studying and understanding such phenomena. These events are particularly relevant to the field of coronal seismology, where impulsive events are used as diagnostic tools to estimate the physical parameters of the solar atmosphere remotely.

In this thesis we investigate quasi-periodic pulsations in flares from both a numerical and observational perpective, mostly in terms of magnetohydrodynamic (MHD) waves. It has long been suggested that MHD modes may be the cause of QPP in flares as they are capable of modulating a wide range of observable quantities. We study one such mode in detail: the sausage mode. For a model including significant gas pressure, the characteristic period, the ratio of the mode harmonics and the behaviour of the wavenumber cutoff are all considered. Although the period and wavenumber are only marginally affected by this gas pressure, the density contrast ratio and length are important factors.

An observational study of a flaring QPP event was undertaken, where new techniques were developed in an attempt to successfully diagnose the QPP mechanism. Cross-correlation mapping was applied to spatially resolved radio data, showing how the strength and phase relationship of a flaring oscillation can be mapped in space. Using this information, we were able to exclude many mechanisms as possible drivers for this event, and suggest that an MHD sausage mode is the likely candidate.

A second flaring QPP event was considered, based on the possibility of multiple harmonic oscillations. A sequential spectral peak filtering method was used to demonstrate the presence of multiple significant periods in the flare. Analysis of the harmonic ratios indicated that an MHD wave such as a kink mode was the probable cause.

Finally we explore the potential of a new technique in the context of the solar corona, the combination of empirical mode decomposition (EMD) and the Hilbert spectrum. It was established that, under certain circumstances, this method compared favourably with existing analysis techniques such as the Morlet wavelet, and may lead to significant future observational results.

Chapter 1

Introduction

1.1 Structure of the Sun

The Sun is a huge ball of highly ionised gas, or *plasma*, with a radius over 100 times that of Earth. It consists mostly of hydrogen which is undergoing a continuous thermonuclear reaction at its centre. Hydrogen isotopes in the core, heated to millions of degrees, combine via nuclear fusion to form helium, releasing energy in the process.

The Sun's internal structure can be divided into several distinct layers. The innermost and hottest region, where nuclear fusion occurs, is the core, where the temperature is believed to be around 16 MK. Here the temperature and density are so high that the kinetic energy of the hydrogen nuclei, with the assistance of quantum tunnelling effects, is sufficient to overcome the repulsive electrical force pushing them apart, leading to sufficient collisions for a stable fusion process. The core is surrounded by a thick radiative zone, which transports the energy generated in the core to the outer regions of the sun and the solar system beyond via photons. The travel time of photons from the beginning of the radiative zone to the convection zone is around 1 million years, as they are scattered so many times. The temperature of the radiative zone also decreases steadily with increasing radius, down to around 2 MK at the boundary with the convection zone. The convection zone occupies the outer portion of the solar interior, from

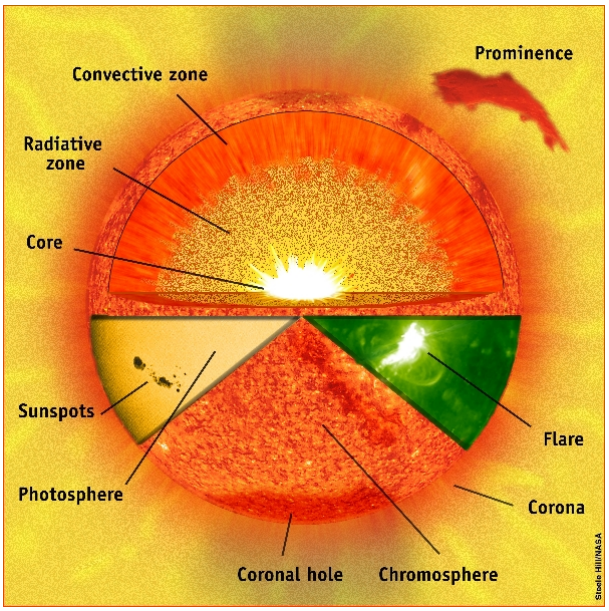

Figure 1.1: Schematic of the solar interior. Courtesy of SOHO (ESA and NASA).

around 0.7 solar radii to the base of the photosphere, which is the beginning of the solar atmosphere. In the convection zone the bulk motions of the Sun's plasma become the dominant method of transporting the energy from the core outwards.

Above the convection zone are the Sun's atmospheric layers; the photosphere, chromosphere, and the corona. These are the regions which can be directly observed by satellites and Earth-based instruments. The lowest of these regions, the photosphere, is the visible surface of the Sun that can be directly viewed from Earth. It is actually a layer of gas around 100 km thick, and its mean temperature is around 5700 K, i.e. very cool compared to the solar interior. The photosphere is also where features such as sunspots and granules are observed. The chromosphere (literally "colour sphere") is a layer above the photosphere where the temperature rises from 5700 K to approximately 20,000 K. The reasons for this temperature change are not well understood. Without optical aids it is difficult to detect the emission from the chromosphere, as it is dominated by radiation from the lower photosphere. Special narrow band filters are used to observe emission e.g.

from the H-alpha line, and thus observe the chromosphere. Between the chromosphere and the corona lies a thin transition region, so-called because the temperature rises rapidly from 20,000 K to over 1 MK. The cause of this large temperature change is unknown, and is referred to as the *coronal heating problem* [see De Moortel et al., 2008, for a recent review on this subject]. The corona is the outermost region of the solar atmosphere and is much hotter than the other atmospheric layers, reaching up to 10 - 20 million K. Radiation from the corona is strong in the EUV and X-ray bands because of this high temperature. Many phenomena such as solar flares, solar prominences and coronal mass ejections (CMEs) are observed in the solar corona. At a height of several solar radii the corona gradually gives way to the solar wind. This solar wind streams out from the Sun in all directions as charged particles escape from the Sun's gravity due to the high temperature of the corona. The solar wind can be effectively described as a plasma, like much of the rest of the Sun.

1.2 The solar activity cycle

The surface and coronal activity of the Sun follows a well-known (but not well understood) 22-year activity cycle. This activity is thought to be linked to the magnetic field structure of the Sun. As the Sun experiences differential rotation and the magnetic field is generally "frozen" into the plasma (see Section 2.1), the magnetic field becomes more complicated over time. Eventually the magnetic field becomes so twisted that it reaches a new configuration with its polarity reversed. This occurs every 11 years and the process repeats, thus after 22 years the Sun returns to an identical activity state. This phenomenon is believed to be caused by a solar dynamo [e.g. Tobias, 2002; Ossendrijver, 2003]. This cycle is manifest in the number of sunspots observed in the photosphere, as well as the number of solar flares and larger CMEs which are observed at the Sun's surface, as illustrated by Figure 1.2. In the early part of an activity cycle, sunspots are generally concentrated in mid-latitude regions of the solar surface. As the cycle progresses, the locations of newly-formed sunspots tend towards the equator.

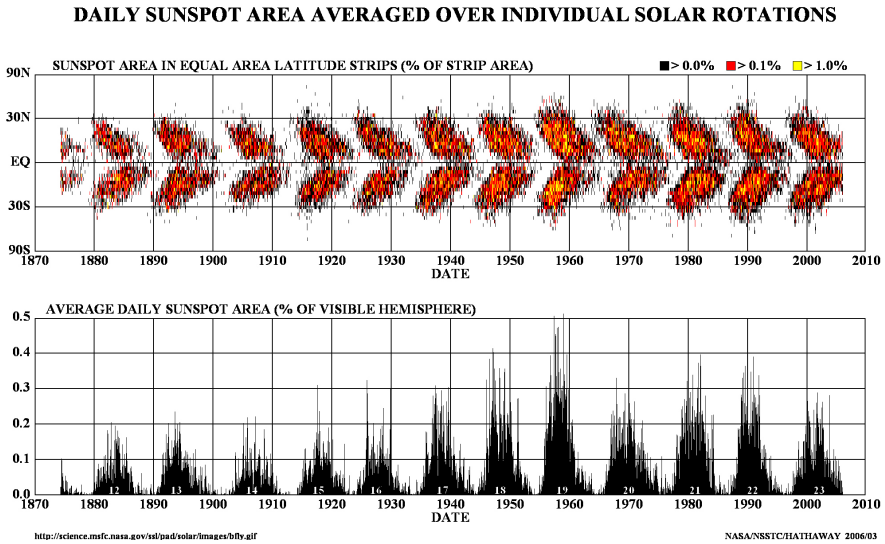

Figure 1.2: Butterfly diagram showing the sunspot number and location as a function of time. Courtesy of NASA.

Plotted as a function of time (see Figure 1.2) this sunspot distribution has a distinct shape and is consequently often referred to as a butterfly diagram.

The Sun is not the only star to experience an activity cycle. Stellar observations have identified many other stars that experience the same behaviour, with a wide range of characteristic periods. Perhaps more interestingly, many stars have also been shown to exhibit no cyclical activity at all. This poses questions about the very fundamentals of stars, and theories explaining why some stars experience activity cycles and others do not deserve further development. Current models of the solar dynamo indicate that the role of the tachocline - the transition layer between the convective and radiative zones - is critical. Hence, the lack of a tachocline is one explanation for observations of non-cyclical stars. This could happen if the star in question is fully convective, i.e. there is no radiative zone.

The Sun also occasionally experiences a prolonged period of very little activity. The last such period is referred to as the **Maunder minimum** [Eddy, 1976, for example].

It occurred around the 17th century, where very few sunspots were observed between 1650 and 1700. The reasons for such behaviour are unclear, although it is not believed to be the result of a lack of observational capability.

1.3 Solar flares and coronal mass ejections

Solar flares are powerful, unpredictable releases of energy frequently observed at the surface of the Sun. Flares can release up to 10^{32} ergs in just a few minutes, and are often associated with even more powerful coronal mass ejections (CMEs), the most powerful phenomena in the solar system. The causes of flares are believed to involve release of energy stored in the magnetic fields present in the solar corona. Consequently, flares are closely associated with sunspots, which occur where the magnetic field protrudes from the Sun's surface.

The frequency of flares is directly correlated with the 22-year solar activity cycle. At the maximum of the cycle the Sun is very active, resulting in frequent X-class flares (the largest classification, see for example Aschwanden [2005]), regular CMEs and a large number of sunspots. By contrast, at solar minimum the Sun is relatively placid, with few flares and sunspots observed. The locations of flares and CMEs are also dependent on the solar dynamo. Early in a new cycle, sunspots - and by extension flares and CMEs - appear mostly in mid-latitude regions. As the cycle progresses, sunspots not only become more frequent, but also become more concentrated near the equator. This can be illustrated using the butterfly diagram shown in the top panel of Figure 1.2.

1.3.1 The standard flare model

Solar flares are thought to be formed when bundles of magnetic flux, distinct from the background magnetic field, are pushed up through the Sun's photosphere into the outer atmospheric layers. These field structures are a consequence of both the Sun's internal dynamo process and the differential rotation and convective motion of the atmosphere. Sunspots - regions with lower temperatures than the surrounding photosphere - form in

the regions where the magnetic field is strong. Since the corona, like many plasmas, can be considered as an *ideal plasma* (i.e. the resistivity is negligible), the magnetic flux is 'frozen' into the plasma and forms persistent loop structures. Plasma can become trapped by the magnetic field and fill such structures, the result being field-aligned enhancements in density. This is then observed in the EUV and soft X-ray bands via a combination of thermal brehmsstrahlung and ion emission. These structures are what we refer to as *coronal loops*.

The exact process that causes the energy release we associate with flares is unknown, but is believed to involve magnetic reconnection, which can be triggered when the magnetic field structure develops an instability. The widely-accepted model of flares and CMEs in such terms is known as the CSHKP model after the five scientists behind its basic development: Carmichael, Sturrock, Hiroyama, Kopp and Pneuman [Carmichael, 1964; Sturrock, 1966; Hirayama, 1974; Kopp and Pneuman, 1976]. The model has seen numerous modifications over the years, some of which are summarised in Figure 1.3, but the fundamentals remain intact. In this model, the reconnection site is located at a magnetic null point above the loop apex. When reconnection occurs, some of the energy stored in the field is released and particles are accelerated to relativistic, nonthermal energies. Many of these particles are ejected from the atmosphere altogether and propagate into space, a particularly large effect in the case of CMEs. However, some of these particles travel downwards along magnetic field lines towards the flare footpoints - the regions where the loop structure encounters the chromosphere. When these accelerated particles encounter the much denser chromosphere they interact with the plasma, causing non-thermal bremsstrahlung emission. This is observed as hard X-ray sources at or near the visible footpoints. White light emission is also often observed at these footpoints, although it is not thought to be a direct result of non-thermal brehmsstrahlung.

X-ray emission spectra from solar flares (see Figure 1.4) can be quantified therefore in terms of three main components [Aschwanden, 2005]. The first is thermal emis-

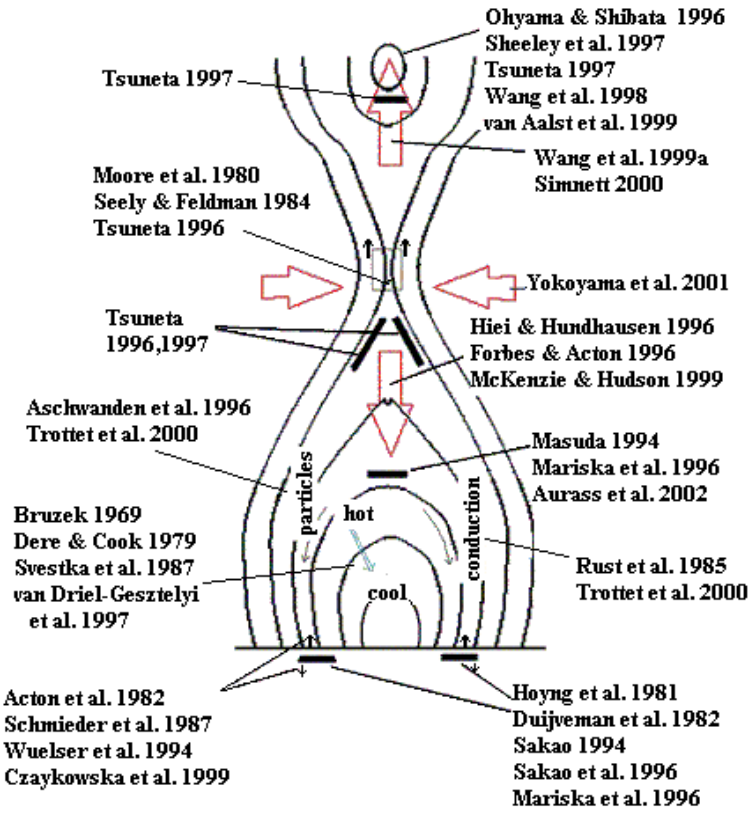

Figure 1.3: Illustration of the standard flare model and some of the many supporting observations [McKenzie, 2002].

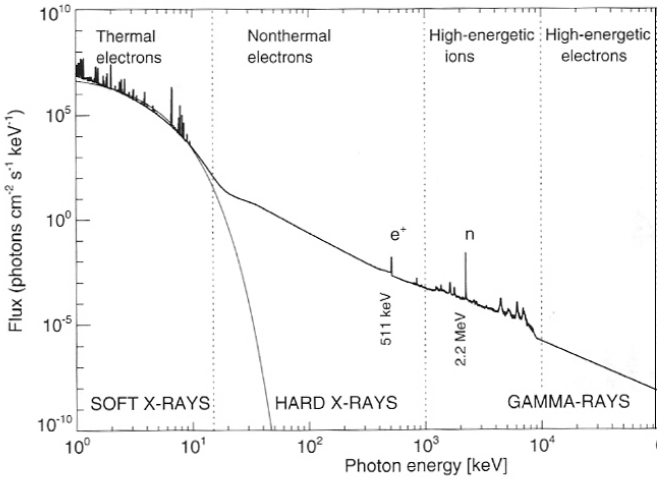

Figure 1.4: Example of a typical flare spectrum at X-ray energies, showing the three main components of emission: thermal brehmstrahlung, non-thermal electrons, and ion-ion interactions. Courtesy of Aschwanden [2005].

sion, which is a result of bremsstrahlung radiation from the hot plasma particles. This emission takes the form of a Gaussian distribution in energy, and dominates typically in EUV and X-rays up to around 30 keV. The second component is the non-thermal bremsstrahlung associated with the accelerated particles from the flare footpoints. This regime follows a power law distribution and tends to dominate at X-ray energies above 30 keV. Only the largest flares release much detectable energy above the 100 keV range. For these flares, a third spectral regime becomes important; ion-ion interactions (as opposed to electron-proton interactions) sometimes result in energy release in the gamma ray range. This is usually manifest as a plethora of narrow emission lines which correspond to specific nuclear interactions.

Flares also output energy in the radio and microwave wavelengths. One of the main regimes that causes this is the gyrosynchotron mechanism [Ramaty, 1969; Dulk and Marsh, 1982], whereby mildly-relativistic electrons accelerated by a flare interact with

the background magnetic field, for example when travelling downwards along loop legs. Gyrosynchotron emission is frequency dependent, and is also a function of the plasma concentration, the line-of-sight (LOS) observation angle and the power law index and concentration of non-thermal electrons. This mechanism is discussed further in Section 2.4.3.

1.4 Observational instruments

The Sun is under constant observation from a variety of different scientific instruments, both space-borne and ground-based. The majority of these probe the solar atmosphere in an attempt to gain insight into the physical mechanisms behind solar activity, e.g. flares, prominences and CMEs.

1.4.1 Nobeyama Radioheliograph

The Nobeyama Radioheliograph[1] [Nakajima et al., 1994] is a ground-based radio interferometer located in Japan. Construction was completed in 1992 and it has been taking daily observations of the Sun since then. The Radioheliograph consists of 84 parabolic detectors with individual diameters of 80cm arrayed in north-south and east-west lines. This arrangement allows observations to be spatially resolved on the solar surface. The instrument observes at two frequencies: 17 GHz and 34 GHz. The maximum spatial resolution is 5 arcseconds at 34 GHz and 10 arcseconds at 17 GHz. More precisely, the given resolutions are the full-width half-maximum (FWHM) values of the instrument beam size. This beam size is determined by the lengths of the lines of parabolic antennae (see Figure 1.5). Perhaps the most straightforward description of the beam size is that a radio point source on the sun would be detected by the Nobeyama Radioheliograph as a circular source with a diameter of 10 arcseconds at 17 GHz.

As the instrument is a radio interferometer, it does not produce images directly. Instead, spatial images are obtained using a Fourier reconstruction process. The best

[1] http://solar.nro.nao.ac.jp/norh/

Figure 1.5: The Nobeyama Radioheliograph in Japan. Courtesy of NoRH.

feature of the Radioheliograph is its excellent temporal resolution; it is capable of making observations with a frame rate as low as 0.1s. This is offset by a relatively modest maximum spatial resolution, which compares rather poorly to space-based observatories such as TRACE and Hinode XRT, which are capable of approximately 1 arcsecond resolution. The most obvious disadvantage of course is that the Nobeyama Radioheliograph can only make observations during daylight hours, which can be as little as 8 hours per day in winter months.

1.4.2 The Reuven Ramaty High Energy Solar Spectroscopic Imager (RHESSI)

The RHESSI satellite[2] [Lin et al., 2002] was named after the late Reuven Ramaty and was launched in 2002. It is located in low-Earth orbit and makes regular observations of the Sun. RHESSI was designed to perform detailed spectroscopy, but is coincidentally an excellent imager. Its nine photometric detectors operate in the X-ray and gamma-ray regimes and can provide a spatial resolution as high as around 2.5 arcseconds.

[2] http://hesperia.gsfc.nasa.gov/hessi/

Figure 1.6: The RHESSI satellite. Courtesy of Spectrum Astro Inc.

It is also theoretically capable of recording the time and energy information of every photon incident on its detectors. The maximum energy resolution of RHESSI is as low as approximately 0.3 keV, meaning that any photon impacting the detectors can be pinpointed in both time and energy.

RHESSI orbits the Earth several times per day. While it is obscured from the Sun it transmits the data stored in memory down to the operations centre on Earth, thus ensuring the satellite's memory is free in case of a particularly large event. RHESSI's detectors are also mounted with attenuators which are programmed to slide in front of the detectors in the event of particularly high count rates, e.g. during a powerful solar flare. This prevents detector dead-time from becoming a problem, avoids filling the on-board memory too quickly, as well as accounting for pulse pile-up.

The disadvantage of RHESSI is a consequence of its low-earth orbit. Although this makes it far easier to download large quantities of data from the satellite, it also means that the satellite experiences frequent night-times. In fact, a 'daytime' observation for RHESSI lasts for only 75 minutes and is followed by 35 minutes of night, making continuous long-term observations of the Sun impossible. This problem is compounded by a phenomenon known as the South Atlantic Anomaly (SAA), a region of

the Earth's atmosphere containing particularly energetic particles. This region interferes with RHESSI observations and may even damage its on-board equipment. Thus whenever RHESSI passes through this region its instruments are deactivated to prevent damage.

1.4.3 The Solar and Heliospheric Observatory (SOHO)

The Solar and Heliospheric Observatory[3] [Domingo et al., 1995] was an ESA and NASA collaboration and was launched in 1995, making it one of the older satellites currently in operation. However it is also among the most successful and celebrated. SOHO orbits the Sun in the Sun-Earth line, where it sits at the Lagrangian (L1) point, approximately 1.5 million kilometers away from Earth. This allows for uninterrupted observations of the Sun. SOHO houses 12 different instruments, including an Extreme Ultraviolet Imaging Telescope (EIT), a Coronal Diagnostic Spectrometer (CDS), a Michelson Doppler Imager (MDI), and multiple coronographs (C1, C2, C3) for tracking CMEs. Despite the satellite's age, almost all of the original instruments remain fully operational. The EIT and MDI instruments in particular are among the most widely used in the solar physics community, an indication of the impressive contribution of SOHO.

1.4.4 Other instruments and future missions

Amongst the newest instruments to join the solar observational network are Hinode and STEREO, both launched in 2006, and Coronas-Photon, a Russian satellite launched in 2009. Hinode houses a Solar Optical Telescope (SOT), an X-ray Telescope (XRT), and an Extreme Ultraviolet Imaging Spectrometer (EIS) similar to the EIT on board SOHO. The SOT is capable of an unprecedented spatial resolution of 0.2 arcesconds, while the XRT and EIS are both class-leading instruments in their own right, designed for imaging and spectroscopy of high temperature thermal emission respectively. STEREO consists of two nearly identical satellites, one orbiting the Sun in front of the Earth, the other

[3] http://sohowww.nascom.nasa.gov/

behind. Thus for the first time 3-dimensional images of solar events are possible. One of its main instruments is a Heliospheric Imager (HI), a wide angle imaging device designed for tracking CMEs. Other instruments currently in use include the Transition Region and Coronal Explorer (TRACE), the solar wind observing ACE and WIND satellites, as well as numerous ground-based observatories.

Several future missions and projects exist in various stages of development. Principal among these is the Solar Dynamics Observatory (SDO). SDO is at an advanced stage and is currently scheduled for launch in the autumn of 2009. The Observatory will house three instruments. Firstly, a Helioseismic and Magnetic Imager (HMI) will act to compliment and ultimately replace the MDI on board SOHO. The Extreme Ultraviolet Variability Experiment (EVE) will image the Sun in the ultraviolet range with excellent spectral and temporal resolution. However, perhaps the most anticipated of the new instruments is the Atmospheric Imaging Assembly (AIA) , which will take regular images of the Sun at multiple wavelengths.

A different approach will be undertaken by ESA's Solar Orbiter, a mission planned for launch between 2015 - 2017. Unlike most instruments, the Orbiter's mission profile is for close-in observations of the Sun. It will approach as close as 48 solar radii, and spend a significant time observing the solar poles because of its orbit.

Chapter 2

Magnetohydrodynamic oscillations and waves in the corona

2.1 Magnetohydrodynamics

Plasma behaviour can be described in a number of ways. Large scale, slow evolution of plasma can be described by the well-established theory of Magnetohydrodynamics (MHD), a combination of Maxwell's equations and the Navier-Stokes equations of fluid dynamics. In MHD, the description of the plasma is subject to a number of simplifications and assumptions, modifications which are often necessary to allow the possibility of numerical simulations. Here we examine the basic properties of MHD.

Firstly, in MHD the plasma is treated as a single electrically conducting fluid, rather than considering ion and electron species separately. It is also assumed by extension that the plasma is neutral, i.e. that there are equal numbers of electrons and ions in the plasma. This allows the expression for continuity to be written for the entire MHD plasma as a single fluid, as shown in Equation 2.1. Also, MHD is a theory designed to describe large scale, relatively slow dynamics of plasma. Thus MHD is usually only valid when the plasma is sufficiently collisional, i.e. the characteristic time of the studied process is much greater than the mean free path time in the plasma. Similarly,

the characteristic size of the system must be much greater than the Larmor radius and the mean free path length in the plasma. MHD additionally assumes that velocities are non-relativistic. Another underlying assumption is that the plasma has a Maxwellian distribution, a necessary condition for the concept of temperature to be introduced.

Despite all these assumptions, MHD has proven to be a robust theory with a wide range of applications in both laboratory and astrophysical plasmas. The governing equations of MHD can be summarised as:

$$\frac{\partial \rho}{\partial t} + \nabla.(\rho \mathbf{V}) = 0, \tag{2.1}$$

$$\frac{\partial \mathbf{B}}{\partial t} = \nabla \times (\nabla \times \mathbf{B}) + \eta \nabla^2 \mathbf{B}, \tag{2.2}$$

$$\rho \frac{\partial \mathbf{V}}{\partial t} = -\frac{1}{\mu} \mathbf{B} \times (\nabla \times \mathbf{B}) - \nabla p, \tag{2.3}$$

$$\frac{\rho^\gamma}{\gamma - 1} \frac{d}{dt} \left(\frac{p}{\rho^\gamma} \right) = -L. \tag{2.4}$$

These equations are the Continuity, Induction, Euler, and Energy equations respectively. The quantity ρ is the total plasma density, $\mathbf{B}$ is the magnetic field, $\mathbf{V}$ is the bulk velocity of the plasma, η measures the resistivity of the plasma, p is pressure and L is a function combining non-adiabatic effects, radiation, thermal conduction, Ohmic heating, and sometimes a 'coronal heating' term. The energy equation shown is not unique; its form depends on the assumptions made about the physical system. These equations form a closed set connecting the magnetic field $\mathbf{B}$, the bulk velocity of the plasma $\mathbf{V}$, the mass density ρ and the gas pressure p. Thus they are extremely useful in furthering our understanding of the key parameters in astrophysical plasmas.

The equations of MHD can be further simplified by assuming that the convective term in the induction equation dominates with respect to the diffusive term, i.e. by assuming that the plasma is perfectly conducting. This is called the *ideal plasma approximation*, and means that magnetic field lines behave as if they move with the plasma.

This is also referred to as *ideal MHD*. A further simplification is the *cold plasma approximation*, where β, which is the ratio of the gas pressure to the magnetic pressure, is assumed to be very small. The cold plasma approximation is used to characterise certain parts of the solar atmosphere, such as the corona.

2.2 MHD waves

An important property of MHD is the existence of wave solutions which can be derived in both bounded and unbounded cases. In fact, recent observations have led to the realisation that MHD waves are ubiquitous in solar plasmas as well as laboratory plasmas. Thus understanding of the wave mode mechanisms is crucial.

In an unbounded uniform plasma there are three types of MHD waves, whose properties are markedly different. These are **Alfvén** waves, **fast** magnetoacoustic waves and **slow** magnetoacoustic waves. Alfvén waves are incompressible and locally supported. This means that they do not cause density variations, and propagate along magnetic surfaces without interacting with neighbouring surfaces. Alfvén waves are also dispersionless. As a consequence they can propagate over very large distances in the solar corona, depositing energy far from wave sources.

Fast and slow magnetoacoustic waves on the other hand are both compressible, i.e. they perturb the density of the plasma. Fast waves are not constrained by the magnetic field direction and may propagate in almost any direction, unlike Alfvén waves. Slow wave propagation direction constitutes a narrow cone in the direction of the magnetic field. Under coronal conditions slow waves propagate at the sound speed, in contrast with their fast and Alfvén counterparts, which propagate at or above the Alfvén speed. The different speeds of slow mode propagation and their differing observational properties allows them to be observationally distinguished from their fast and Alfvén counterparts with relative ease.

The presence of these waves in the solar corona provides a powerful opportunity for remote diagnostics of the Sun. This technique is known as MHD coronal seismology

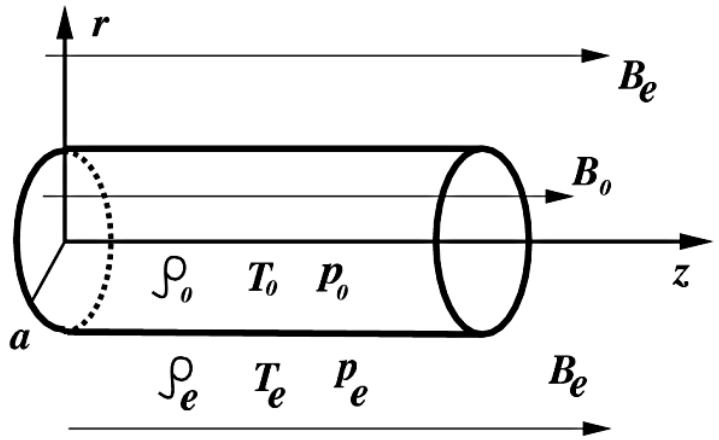

Figure 2.1: The straight cylinder model of a plasma structure [Nakariakov and Verwichte, 2005].

and has become a popular tool in recent years, although it is not a new idea; it was proposed as early as 1970 [Uchida, 1970]. However, only in recent years have the requisite observational instruments become available.

2.2.1 MHD modes of a magnetic cylinder

One of the most useful generalised plasma structures is the straight cylinder model. This model is frequently applied to coronal loop studies and flare studies and has proven a robust theoretical tool. We consider a cylinder of radius a filled with a plasma with uniform density ρ_0. The gas pressure inside the cylinder is p_0 and the magnetic field strength is B_0, and acts only in the z-direction. The external medium is also considered to be uniform, with density ρ_e, gas pressure p_e and magnetic field strength B_e, also acting in the z-direction. Curvature of the structure, although a factor that should be accounted for in the application of this model to loops and flares, is considered a second order effect, thus the cylinder is assumed to be straight for simplicity. Gravity is also neglected.

For such a structure to be stable the total pressure must be balanced at the boundary, hence:

$$p_o + \frac{B_o^2}{2\mu} = p_e + \frac{B_e^2}{2\mu}. \tag{2.5}$$

Using this condition, it is possible to derive a wave equation for the plasma by considering linearised perturbations of the MHD equations, and additionally assuming that the normal component of velocity and the total pressure are continuous across the boundary. A perturbation with frequency ω, longitudinal wavenumber k_z and azimuthal wavenumber m which are localised near the cylinder are described by the dispersion relation [Edwin and Roberts, 1983]

$$\rho_e \left(\omega^2 - k_z^2 C_{Ae}^2\right) m_o \frac{I_m'(m_o a)}{I_m(m_o a)} + \rho_o \left(k_z^2 C_{Ao}^2 - \omega^2\right) m_e \frac{K_m'(m_e a)}{K_m(m_e a)} = 0, \tag{2.6}$$

where I_m and K_m are Bessel functions of order m, and I_m' and K_m' are the derivatives of those functions with respect to x. The parameters m_e and m_o are the radial wavenumbers in the external plasma and the internal plasma respectively, and are given by:

$$m_i^2 = \frac{\left(k_z^2 C_{si}^2 - \omega^2\right)\left(k_z^2 C_{Ai}^2 - \omega^2\right)}{\left(C_{si}^2 + C_{Ai}^2\right)\left(k_z^2 C_{Ti}^2 - \omega^2\right)}. \tag{2.7}$$

Here C_{Ae} and C_{Ao} are the Alfvén speeds in the external and internal media respectively. C_{si} is the sound speed in the media, where the index $i = o, e$. For convenience the tube speed C_{Ti} is also introduced, where:

$$C_{Ti} = \frac{C_{si} C_{Ai}}{\sqrt{C_{si}^2 + C_{Ai}^2}}. \tag{2.8}$$

Thus, equation 2.6 allows us to find the frequency of an MHD oscillation given knowledge of the mode numbers m, k_z, and the radial number l. Further, the mode numbers determine the structure of the MHD oscillation. The case where $m = 0$

is known as the $sausage$ mode, which is symmetric about the cylinder axis. If instead $m = 1$ we have the $kink$ mode, which is asymmetric, and for $m \geq 2$ we have $ballooning$ modes. For each value of m, there are an infinite number of wave harmonics available, corresponding to different values of the radial number l and the longitudinal wavenumber k_z. The parameter l is connected with the number of oscillation maxima located inside the cylinder in the radial direction.The modes with the longest period, i.e. where the wavelength is twice the plasma cylinder length, are known as $global$ modes.

Hence, for given integer mode numbers, the dispersion relation can be used to determine the frequency ω of the mode. This is illustrated in Figure 2.2. The fast modes occupy the region between the internal Alfvén speed C_{A0} and the external Alfvén speed C_{Ae}, while the slow modes are grouped together close to the internal sound speed C_{s0}.

In the dispersion diagram, the sausage modes (m=0) are indicated by the solid lines. The kink modes (m=1) are the dotted lines. Higher mode numbers (m=2,3,...) are indicated by the dot-dashed and dashed lines. The diagram illustrates that in the cylindrical model all the fundamental modes exist for all ka with the notable exception of the sausage mode, which approaches a cut-off value. This cut-off is given by:

$$k_z = \frac{j_0}{a}\left[\frac{\left(C_{so}^2 + C_{Ao}^2\right)\left(C_{Ae}^2 - C_{To}^2\right)}{\left(C_{Ae}^2 - C_{Ao}^2\right)\left(C_{Ae}^2 - C_{so}^2\right)}\right]^{1/2}, \tag{2.9}$$

where $j_o \approx 2.40$ is the first zero of the Bessel function $J_o(x)$. The periods of the global sausage and kink modes can also be found. For a loop of length L the period of the global sausage mode is [Nakariakov and Verwichte, 2005]:

$$P_{saus} = \frac{2L}{C_p}, \tag{2.10}$$

where C_p is the phase speed of the mode. Similarly, the global kink mode period is given by:

$$P_{kink} = \frac{2L}{C_k}, \tag{2.11}$$

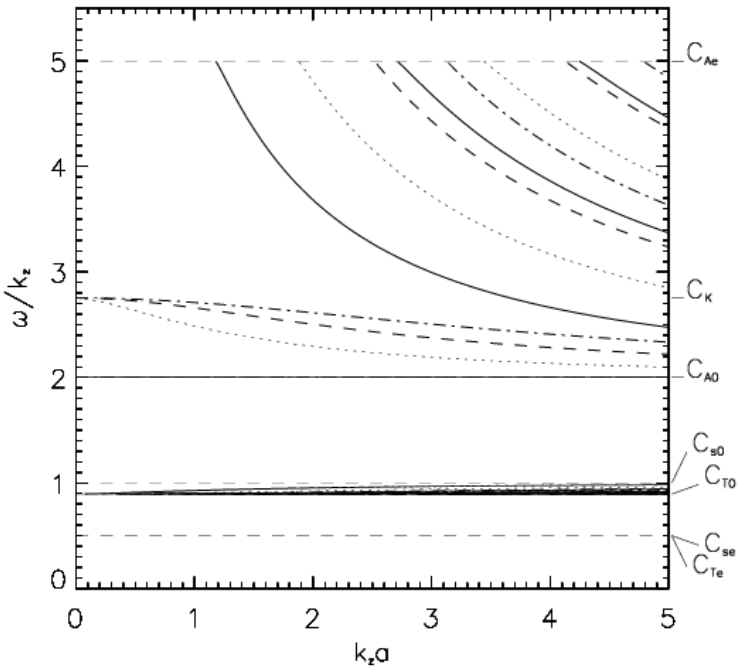

Figure 2.2: Dispersion diagram for a magnetic cylinder under coronal conditions [Nakariakov and Verwichte, 2005]. The solid lines correspond to m=0, the dotted lines to m=1, the dashed lines to m=2 and the dot-dashed lines to m=3. The different groups of these lines correspond to different values of the radial wavenumber l.

where C_k is the kink speed, defined as:

$$C_k = \left(\frac{\rho_o C_{Ao}^2 + \rho_e C_{Ae}^2}{\rho_o + \rho_e} \right)^{1/2}. \tag{2.12}$$

The phase speeds of all the other global modes except the sausage mode tend to this kink speed in the long wavelength $(ka \to 0)$ limit.

This model of MHD waves should be considered with a proviso. The extra condition $m_e > 0$ has been assumed. This corresponds to only allowing solutions for which the modes are oscillatory inside the tube structure, and evanescent outside. Only these modes, known as *body modes*, are shown in Figure 2.2. This condition is also known as *mode localisation*. The dispersion diagram also shows the existence of an Alfvén wave mode, denoted by a single solid line at C_{Ao}. This mode is non-dispersive unlike the fast magnetoacoustic modes and propagates at the Alfvén speed of the internal medium. The implication is that Alfvén modes can propagate extremely long distances, transporting energy and momentum, making them an important tool for understanding coronal heating mechanisms and flare structures.

2.3 Quasi-Periodic Pulsations in Flares

Quasi-periodic pulsations (QPP) have been seen in emission from solar flares for several decades [see Nakariakov, 2007, for a review]. In a typical event, the emission intensity from a solar flare is observed to oscillate with a characteristic period, sometimes stably for several minutes, other times in short bursts. One of the most prominent examples of flaring QPP is the famous 'Seven Sisters flare' [Kane et al., 1983], which occurred on 7th June 1980 (see Figure 2.3). The oscillation periods in flaring QPP have been observed to vary from a few seconds up to several minutes. In some cases oscillations with more than one characteristic period occur simultaneously [Melnikov et al., 2005]. QPP can also take the form of periodic Doppler shift or Doppler broadening observations. A number of such events were observed using the Bragg Crystal Spectrometer (BCS) on

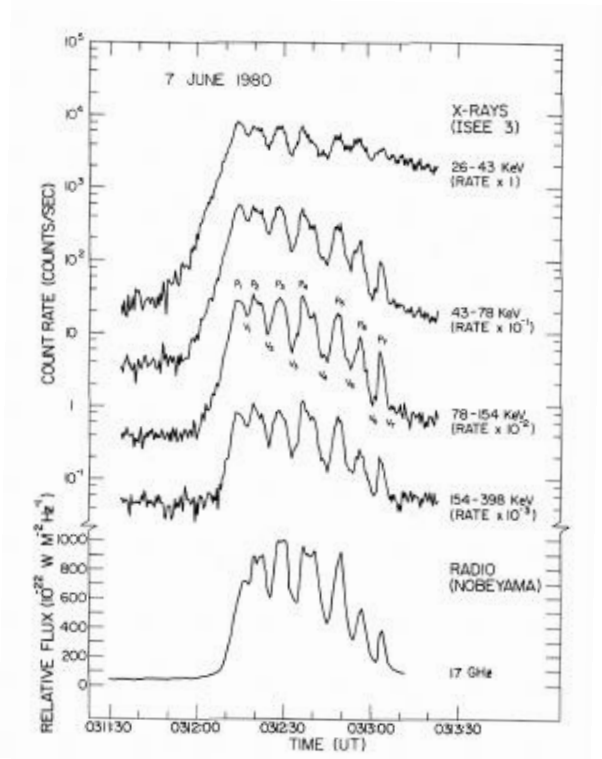

Figure 2.3: The well-known 'Seven Sisters' QPP event from 7th June 1980, observed in multiple energy channels [Kane et al., 1983].

board Yohkoh and are described in Mariska [2006].

Presently, the interest in flaring QPP is connected mainly with the development of coronal seismological techniques for determining physical conditions and processes operating in flaring active regions. Also, the understanding of flaring QPP in the solar corona will open up very interesting perspectives for the diagnostics of stellar coronae (e.g. Mathioudakis et al. [2003]; Mitra-Kraev et al. [2005]). In the stellar context, coronal seismological methods are able to give additional constraints on the physical parameters, compensating for the lack of spatial resolution [Nakariakov, 2007].

Recent articles in the literature suggest that the correct identification of the mechanism responsible for QPP should be based upon spatially resolved analysis [Grech-

nev et al., 2003] and [Nakariakov et al., 2003], although only in the last decade has the necessary technological capability existed. Spatially resolved analysis includes examination of amplitudes and phase relationships of oscillations in different parts of the flaring loop. In particular, the presence of several different MHD modes with different spatial structure and periods was established in Melnikov et al. [2005]. The leading instrument used in these studies is the Nobeyama Radioheliograph (NoRH), which allows one to detect the spatial distribution of the microwave emission of non-thermal electrons, caused by the gyrosynchrotron mechanism, along the flaring loop. In addition, hard X-ray instruments which have comparable spatial and temporal resolution allow one to observe the footpoints of the flaring loop or arcade and sometimes the region above the loop apex.

2.4 Mechanisms for emission modulation

Various suggestions have been made regarding possible causes of QPP in solar flares. Since QPP is manifest at many different wavelengths and energy ranges, it is a difficult question to categorially resolve. Not only must the modulation of the plasma parameters such as density and temperature be considered (observed in thermal emission), but also variations in the rate of electron acceleration (leading to white light, hard X-ray and gyrosynchotron emission) as well as rates of magnetic reconnection itself. However, one popular and enduring mechanism is the modulation of physical parameters of the emitting plasma by magnetohydrodynamic (MHD) modes of the flaring plasma structure. All four kinds of MHD modes can produce modulation: torsional [Tapping, 1983], longitudinal [Nakariakov and Melnikov, 2006], kink [Grechnev et al., 2003] and sausage [Nakariakov et al., 2003]. In addition, sausage modes can modulate the precipitation rate of the non-thermal electrons accelerated by the flare via periodic change of the magnetic mirror ratio [Zaitsev and Stepanov, 1982]. Also, in Foullon et al. [2005] and later Nakariakov et al. [2006], it has been suggested that QPP in a solar flare might be caused by MHD oscillations in another loop situated near the flare site but magnetically

disconnected from the flaring region. The fast waves leaking from the oscillating loop can reach the flaring site and periodically trigger the process of magnetic reconnection. This mechanism can explain the observed periodic variation of the flaring emission in terms of the periodic acceleration of non-thermal electrons. The mechanisms connected with the modulation of the precipitation rate and the periodic triggering of reconnection can explain the observed correlation in time of hard X-ray and microwave QPP.

2.4.1 Modulation of thermal emission by compressible waves

Thermal emission, captured in soft X-ray and EUV bands, can in theory be modulated by density perturbations in a sufficiently hot plasma. This intensity variation can be approximated by:

$$I \sim (\rho_0 + \tilde{\rho})^2 \approx \rho_0^2 + 2\rho_0\tilde{\rho}, \tag{2.13}$$

where the density perturbation $\tilde{\rho}$ is small. Thus a weak density perturbation causes an intensity perturbation which is twice as large.

Density perturbations are characteristic of some MHD modes, most notably the sausage mode, which is essentially compressible and displaces the plasma symmetrically about the loop axis. Similarly, longitudinal (also known as slow magnetoacoustic) modes also naturally produce density variations. However, observed thermal emission intensity is also proportional to the column depth of the emitting plasma along the line-of-sight (LOS). Thus an incompressible perturbation is also capable of modulating the emission intensity by periodically changing the angle between the LOS and the loop axis. Studies by Cooper et al. [2003] showed that the kink mode can cause this effect.

2.4.2 Modulation of the electron precipitation rate

Pulsations in solar flares are often observed not just in soft X-ray or EUV bands, but in hard X-ray bands and white light. Such oscillations can be produced by periodic modulation of the electron precipitation rate. Essentially the hot loops in flaring plasma

act as traps for accelerated electrons, due to the associated magnetic fields. Those electrons with a large pitch angle bounce between the magnetic mirrors created by the magnetic flux tube at the loop legs. The pitch angles of the electrons are determined by the magnetic fields at the loop apex and the footpoints. The critical pitch angle below which electrons can escape is given by:

$$cot^2\alpha < \frac{B_{foot} - B_{apex}}{B_{apex}}. \tag{2.14}$$

Magnetoacoustic oscillations, such as the MHD sausage mode, can periodically vary the strength of the loop top magnetic field. Hence the pitch angle at which electrons can escape from the plasma will also modulate and particles will escape towards the loop footpoints. These electrons interact with the denser plasma encountered in the photosphere and result in the observed white light and hard X-ray oscillations at the loop footpoints via bremsstrahlung [Zaitsev and Stepanov, 1982]. The rate of electron precipitation can also be modulated by time variations of the acceleration process itself.

2.4.3 Modulation of gyrosynchotron emission via MHD oscillations

Oscillations in flares are also frequently observed in the microwave range, for example with the Nobeyama Radioheliograph in Japan. In general, microwave emission during flares is generated by the gyrosynchotron mechanism, where accelerated electrons interact with the background magnetic field. The gyrosynchotron spectrum is well understood and features a single turnover frequency. Above this frequency the emission is optically thin and obeys a power law. As shown by Dulk and Marsh [1982], the intensity of optically thin gyrosynchotron radiation at frequency f can be approximately determined by the value of the magnetic field B in the plasma and the angle θ between the line-of-sight and the magnetic field, as follows:

$$I_f \approx \frac{BN}{2\pi} \times 3.3 \times 10^{-24} \times 10^{-0.52\delta} \left(\sin\theta\right)^{-0.43+0.65\delta} \left(\frac{f}{f_B}\right)^{1.22-0.90\delta} \tag{2.15}$$

where δ is the power law spectral index of the electrons, N is the concentration of nonthermal electrons with energies higher than 10 keV, B is the magnetic field strength (measured in Gauss), f_B is the gyrofrequency and θ is the angle between the magnetic field and the line of sight. This empirical approximation is only considered valid when $2 \leq \delta \leq 7$, $\theta \geq 20^\circ$ and $f/f_B \geq 10$. Variations in the magnetic field strength B can be easily associated with both the sausage and kink MHD modes.

2.4.4 Periodic triggering of flares by nearby MHD oscillations

Recently, Foullon et al. [2005] and Nakariakov et al. [2006] developed a model which can explain quasi-periodic pulsations of flares in some cases. In this model it was suggested that pulsations observed in a flaring loop are caused by MHD oscillations in a nearby, non-flaring loop. This nearby loop is not magnetically linked to the flaring loop. An important point is that these MHD oscillations do not cause the flaring energy release itself, but are instead responsible for a periodic triggering effect. The external oscillations affect the flaring loop via their evanescent or leaky component. The arrival of the wave modes - which appear like fast magnetoacoustic waves from the point of view of the reconnection site - is supposed to lead to current instabilities, high resistivity and hence trigger magnetic reconnection. The result is charged particle acceleration, hence quasi-periodic pulsations in X-ray, white light and radio bands are observed at the flare site.

The first observational example of this type of event was analysed by Foullon et al. [2005] using the RHESSI satellite. In this study long period oscillations were observed in thermal X-rays from the flaring activity of 5th - 6th February 2003. The detected periods were of the order 8 - 12 minutes. Based on the fact that the flaring loop itself was extremely long, this loop was not considered able to support the relevant MHD modes with the required period. It was subsequently shown that a nearby transequatorial loop was present which was of the size capable of causing the observed oscillations.

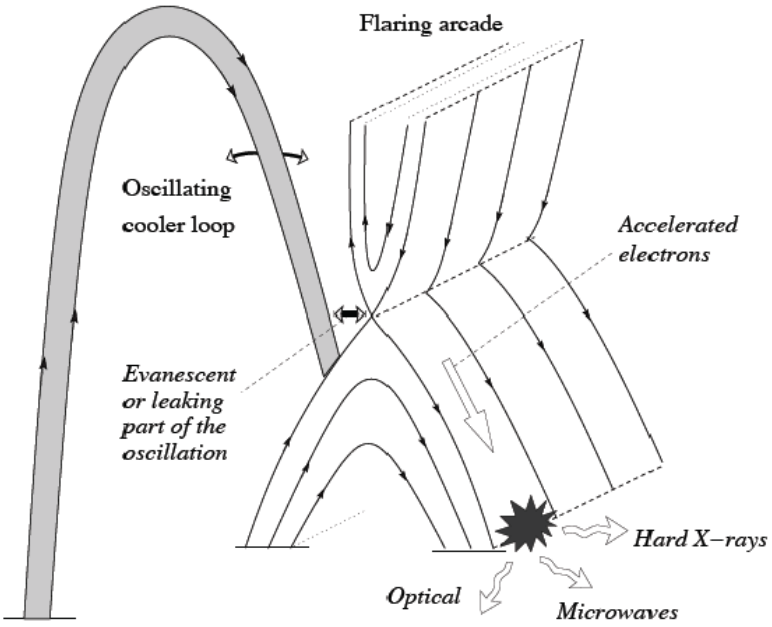

Figure 2.4: Illustration of the interaction of a nearby oscillating loop with a flaring region, including periodic microwave and hard X-ray emission [Nakariakov et al., 2006].

2.4.5 Emission modulation via periodic magnetic reconnection

Magnetic reconnection has long been a central tenet of solar theory. First of all it is widely accepted as the mechanism by which solar flares emit energy; complex magnetic field systems in the pre-flare reconnect into a simpler system, thus releasing some of the energy stored in the field. By extension therefore, magnetic reconnection can be considered as a possible cause for oscillations in flaring emission. Recently, numerical studies have demonstrated that magnetic reconnection can occur in an oscillatory fashion [McLaughlin et al., 2009], especially in the context of plasma jets [Murray et al., 2009]. However, a quantitative theory describing modulation via reconnection is yet to be formulated. This makes it difficult to exclude this mechanism or prove its presence in any observational study of QPP.

Chapter 3

Characteristics of magnetoacoustic sausage modes

3.1 Introduction

The sausage mode (also known as peristaltic or $m = 0$ mode) is a symmetric perturbation of the loop minor radius, in the form of periodic broadening and narrowing of the plasma tube (see Figure 3.1). This mode, with typical periods in the range 5-30 s, is believed to be detected in the microwave and hard X-ray emission associated with flaring solar loops [e.g. Nakariakov et al., 2003; Melnikov et al., 2005; Inglis et al., 2008], and also possibly in H_α emission from cool, post-flare loops [Srivastava et al., 2008]. The sausage mode is essentially compressible, with the density perturbations being in phase with the perturbations of the magnetic field and in anti-phase with the perturbations of the loop minor radius. This mode is also a robust collective disturbance of a plasma structure, which is practically insensitive to small scale irregularities of the plasma [Pascoe et al., 2007b]. The sausage mode can be manifest in both standing and travelling form. It is highly dispersive, with a pronounced dependence of the phase and group speeds upon the wave number. In the standing regime, this makes the spectrum of the resonant frequencies of different spatial harmonics non-equidistant. Long wavelength

(in comparison with the minor radius of the oscillating loop) sausage modes are subject to a cut-off, in contrast with all other magnetoacoustic modes (see Chapter 2). Modes with wavelengths longer than the cut-off are leaky, resulting in damped oscillations inside the loop structure while energy escapes into the surroundings. In this scenario, the phase speed of the mode is slightly higher than the external Alfvén speed [Pascoe et al., 2007a]. For shorter wavelengths, sausage modes are trapped in the guiding structure, and have phase speeds in the range between the internal and external Alfvén speeds (see Figure 2.2). This cut-off wavelength is dependent on the density contrast between the loop and its surroundings. As flaring loops (that is, loops that are present at a flare site during the release of energy) are sometimes dense and compact, both trapped and leaky regimes can occur. One mechanism allowing such loops to become dense is chromospheric evaporation. This will only occur once the flaring energy release has begun, however for a sufficiently compact loop the loop may become filled rather quickly, since the characteristic time of the process depends on the sound speed. The main properties of the sausage mode are derived from the straight cylinder or slab model introduced in Section 2.2.1. Clearly, the slab and the cylindrical cases are not identical, as has been discussed in Kopylova et al. [2007]. In particular, Terradas et al. [2006] demonstrated the important difference in the wave leaking between these geometries. However, the difference in geometry should not be the principal difference in the resonant periods of sausage modes, as the behaviour of this particular mode is known to be almost identical in the slab and cylinder geometries in the trapped regime.

As a result of its compressibility, the sausage mode can be readily seen in microwave, EUV and soft X-ray bands, provided sufficient time resolution is available. Also, this mode is capable of modulating the population of non-thermal electrons via changes in the magnetic mirror ratio in the flaring loop, leading to periodic precipitation of electrons to the loop footpoint (see Section 2.4.2).

The seismological potential of the sausage mode is connected with estimating the magnetic field outside the oscillating plasma structure [Pascoe et al., 2007a], and with

determining the transverse profile of the plasma density in the flaring loop [Nakariakov et al., 2004]. Also, in the case when the microwave spectrum is generated by the gyrosynchrotron mechanism and is spatially resolved, this mode provides a promising basis for combined MHD-microwave diagnostics of flaring plasmas. As the oscillations in lightcurves generated by the sausage mode are often very pronounced, it also opens up possibilities for the diagnostics of stellar coronae [Nakariakov, 2008].

One popular topic of MHD coronal seismology is the use of the ratios of global (or fundamental) modes and their second harmonics (variously referred to as the $P_1/2P_2$ ratio or P_2/P_1 ratio) for the determination of the longitudinal profile of the plasma parameters in the oscillating loop. Andries et al. [2005] noticed that for the kink mode the discrepancy between the observed $P_1/2P_2$ ratio and that theoretically calculated with the use of the straight cylinder model could be attributed to the variation of the plasma density along the loop, e.g. because of gravitational stratification. There have been several attempts to account for this stratification in the theoretical model [see Dymova and Ruderman, 2006; Donnelly et al., 2006; McEwan et al., 2008; Verth and Erdélyi, 2008], and also to extend this study to longitudinal modes [e.g. Díaz and Roberts, 2006]. One of the difficulties with the full scale implementation of the $P_1/2P_2$-based technique in MHD coronal seismology is due to the rare detection of the higher harmonics of the kink mode. This is primarily a result of insufficient temporal resolution of solar EUV imagers.

As the sausage mode is usually observed with the instruments which have very high time resolution (e.g. 0.1 or 1 s in the case of the Nobeyama Radioheliograph), it is possible to detect several harmonics of this mode [Nakariakov et al., 2003; Melnikov et al., 2005]. However, as in contrast with the kink mode the sausage mode is highly dispersive, the identification of the sausage mode harmonic number is a non-trivial task. This is partly due to a significant departure of the $P_1/2P_2$-ratio from unity because of the dispersive modification of the phase speed even in the absence of longitudinal stratification. It becomes especially difficult when spatial resolution is not available.

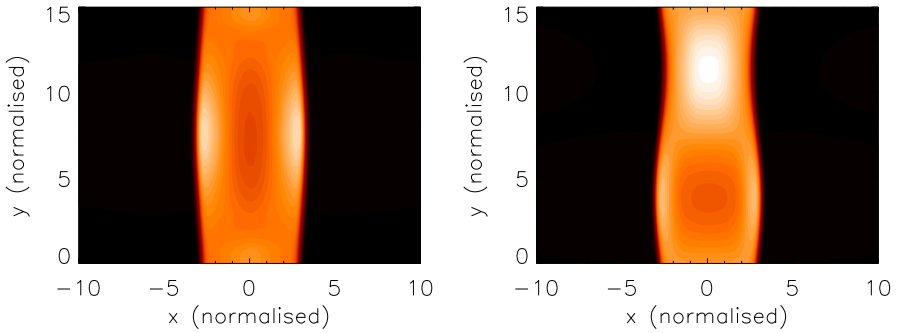

(a) The global sausage mode (b) The second (longitudinal) harmonic

Figure 3.1: Illustrations of a) The global sausage mode and b) The second (longitudinal) harmonic of the sausage mode, shown as filled density contours. In both cases the perturbation is symmetric about the loop axis, which remains unperturbed.

Hence there is need for detailed theoretical modelling of various regimes of the sausage mode dynamics.

In flaring loops the density scale height is usually large because of the associated high temperature, hence it is unlikely that the sausage mode is affected by gravitational stratification in such loops. The effect of the variable cross-section of the flaring loop on the resonant periods of the standing sausage mode was recently considered by Pascoe et al. [2009]. It was established that the sausage mode continued to be supported despite variations in the loop cross-section. It was also shown that the characteristic periods of the global mode and higher harmonics were affected, but weakly so. A similarly small variation in parameters was found when investigating the effects of twist in loops [Erdélyi and Fedun, 2006]. However, the high temperatures and densities of flaring loops also lead to the increase of the plasma-β inside loops [Shibasaki, 2001]. This could potentially cause a significant deviation of the resonant periods and cut-offs from the results obtained in the zero-β approximation studied in Cooper et al. [2003] and Pascoe et al. [2007a].

The purpose of this chapter is to establish the effect of finite plasma-β on

the resonant periods of the sausage mode by full numerical MHD modelling. This includes the behaviour of the fundamental period, the period ratio of the fundamental and higher harmonics, and the cut-off wavenumber. In Section 3.2 we describe the standard theoretical approach to modelling wave modes in a magnetic slab geometry. Section 3.3 details the numerical methods used for the modelling. In Section 3.4 we present our results, which are then discussed in more detail in Section 3.5. The results of this analysis were published in Inglis et al. [2009].

3.2 Sausage modes in a magnetic slab

Following the standard approach [Edwin and Roberts, 1982], we model magnetoacoustic oscillations in a coronal loop as perturbations of a field aligned enhancement in plasma density. The magnetic field is taken to be in the y-direction. The density profile is uniform in the y-direction. In the transverse direction the density is given by the profile [Nakariakov and Roberts, 1995b]:

$$\rho(x) = (\rho_0 - \rho_e)\,\mathrm{sech}^2\left[\left(\frac{x}{a}\right)^n\right] + \rho_e, \tag{3.1}$$

where ρ_e is the external density far from the loop, ρ_0 is the density at the loop apex and a is a characteristic length governing the width of the loop. Here, $n = 1$ corresponds to the symmetric Epstein profile (see Figure 3.2) which allows for analytical treatment [Nakariakov and Roberts, 1995b]. Increasing values of n lead to a steeper profile, meaning that with a large enough exponent ($n \to \infty$) Equation (3.1) can be considered as an approximate step function, also with a known analytical solution for fast magnetoacoustic modes [Edwin and Roberts, 1982]. Most importantly, the use of the profile in Equation (3.1) avoids steep gradients that may lead to strong artificial shocks in numerical simulations.

The equilibrium condition is the total pressure balance between the internal and external plasmas. This may be written as [Edwin and Roberts, 1982]:

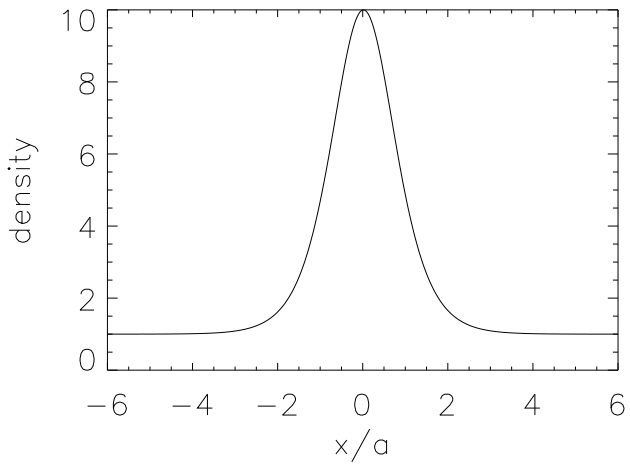

Figure 3.2: Symmetric Epstein profile of the equilibrium plasma density with $\rho_0 = 10\rho_e$.

$$\frac{\rho_e}{\rho_0} = \frac{2C_{\mathrm{s0}}^2 + \gamma C_{\mathrm{A0}}^2}{2C_{\mathrm{se}}^2 + \gamma C_{\mathrm{Ae}}^2}, \tag{3.2}$$

where $\gamma = \frac{5}{3}$ is the adiabatic index, C_{A0} and C_{Ae} are the internal and external Alfvén speeds, and C_{s0} and C_{se} are the internal and external sound speeds.

For a symmetric Epstein profile, the solutions describing the perturbation of the transverse velocity component in the sausage mode are given by:

$$U(x) = \frac{\sinh(x/a)}{\cosh^{\lambda}(x/a)}, \tag{3.3}$$

where

$$\lambda = \frac{\left(C_{\mathrm{Ae}}^2 - C_{\mathrm{p}}^2\right)^{1/2} ka}{C_{\mathrm{Ae}}} + 1, \tag{3.4}$$

and the phase speed $C_{\mathrm{p}} = \omega/k$ is in the range $C_{\mathrm{A0}} < C_{\mathrm{p}} < C_{\mathrm{Ae}}$ [Cooper et al., 2003].

Since C_{p} is typically a large fraction of C_{Ae} (for trapped modes) λ is usually of order 1. The phase speed C_{p} can be worked out analytically from the dispersion

relation:

$$\frac{ka}{C_{\rm A0}^2}\left(C_{\rm p}^2 - C_{\rm A0}^2\right) - \frac{2}{ka} = \frac{3}{C_{\rm Ae}}\sqrt{C_{\rm Ae}^2 - C_{\rm p}^2}. \tag{3.5}$$

This equation allows for the exact analytical solution for the phase speed $C_{\rm p}$. Unfortunately, this solution is only valid for zero-β plasmas.

For a realistic flaring loop the situation is likely to be more complex. A perfect pressure balance, for example, may not hold. Nor are the background plasma parameters likely to be uniform, or the amplitudes of oscillation sufficiently small to be considered linear. However, the global sausage mode is a very robust perturbation, and it remains desirable to examine its properties in a more idealised case before considering higher order effects. It is also likely that the choice of geometry is relatively unimportant for the MHD sausage mode. Part of the reason for this is its simplicity; a symmetric density perturbation about the loop axis independent of the azimuthal angle. This is in contrast to other MHD modes. In the following analysis, we simulate sausage modes using both a step-function density profile and a classical Epstein profile, noting the rationale in each case.

3.3 Numerical model

The numerical simulations of MHD sausage modes presented here were performed in slab geometry using Lare2d [Arber et al., 2001]. This code solves the MHD equations in normalised form. Thus in order to reconstruct physical values from the simulation results it is necessary to define several normalisation constants. In Lare2d, the three primary constants are length L_0, magnetic field strength B_0 and density ρ_0, such that:

$$L = L_0\hat{L},$$

$$B = B_0\hat{B},$$

$$\rho = \rho_0\hat{\rho},$$

where $\hat{L}$, $\hat{B}$ and $\hat{\rho}$ are the quantities actually used in the code. The exact values of the normalisation parameters are a matter of convenience. For the results presented here we have consistently used the following values:

$$L_0 = 1 \text{ Mm},$$

$$B_0 = 1 \times 10^{-3} \text{ T}(10 \text{ G}),$$

$$\rho_0 = 7.95 \times 10^{-13} \text{ kgm}^{-3}.$$

These primary definitions lead to the normalisations for several other parameters. For our chosen values, we subsequently find normalisation constants for time, velocity and temperature:

$$t_0 = 1 \text{ s},$$

$$v_0 = 1 \times 10^6 \text{ ms}^{-1},$$

$$T_0 = 6 \times 10^7 \text{ K}.$$

Dropping the accents for the normalised quantities, the MHD equations may then be written as:

$$\frac{D\rho}{Dt} = -\rho \nabla \cdot \vec{v}, \tag{3.6}$$

$$\rho \frac{D\vec{v}}{Dt} = \left(\nabla \times \vec{B}\right) \times \vec{B} - \nabla P, \tag{3.7}$$

$$\frac{D\vec{B}}{Dt} = \left(\vec{B} \cdot \nabla\right) \vec{v} - \vec{B} \left(\nabla \cdot \vec{v}\right), \tag{3.8}$$

$$\rho \frac{D\epsilon}{Dt} = -P \nabla \cdot \vec{v}, \tag{3.9}$$

where $\vec{v}$ is the plasma velocity, P is the gas pressure, $\vec{B}$ is the magnetic field, ρ is the mass density and $\epsilon = P/\rho(\gamma - 1)$ is the internal energy density.

An initial structure in equilibrium was set up as described in Section 3.2. The plasma nonuniformity is in the x-direction and is symmetric with respect to $x = 0$. In order to control the value of β, the magnetic field was reduced inside the loop as shown in Figure 3.3. All of the values in Figure 3.3 are normalised. The internal density of the loop, ρ_0, is also fixed. The internal gas pressure is left as a free parameter in order to maintain total pressure balance. As a result the plasma temperature varies with the internal gas pressure. Consequently, the simulated plasma structures are both hotter and denser than the surroundings, consistent with the known properties of physical coronal loops.

A convenient way to fulfill the equilibrium condition is to adjust the profile of the magnetic field, keeping all other parameters the same. This is the approach that will be used throughout this work, allowing us to consider the important case of flaring loops filled in with a hot and dense, relatively high-β plasma.

Throughout the remainder of this chapter, the values of plasma-β in the centre of the loop and at infinity are referred to as β_0 and β_e, respectively.

To simulate a sausage mode we set up an initial transverse velocity perturbation of the form:

$$v_x = AU(x)\sin(ky), \tag{3.10}$$

where A is an amplitude and x and y are the coordinates across and along the slab respectively. $U(x)$ is an odd function, normalised to unity and evanescent at infinity. This velocity distribution disturbs the loop at its centre and ensures that a global standing mode is developed. Alternatively, higher harmonics may be generated by choosing a different value of k. To avoid non-linear effects the amplitude of the perturbation must be small compared to the equilibrium parameters. We choose A = 0.002 in all cases, resulting in perturbations which are very small fractions of the equilibrium magnetic field and density (typically $\approx$ 0.1% of the internal density for example). As described in Section 3.2, the magnetic field is aligned in the y-direction, as is the loop itself. Reflective boundaries were applied in the y-direction, while open

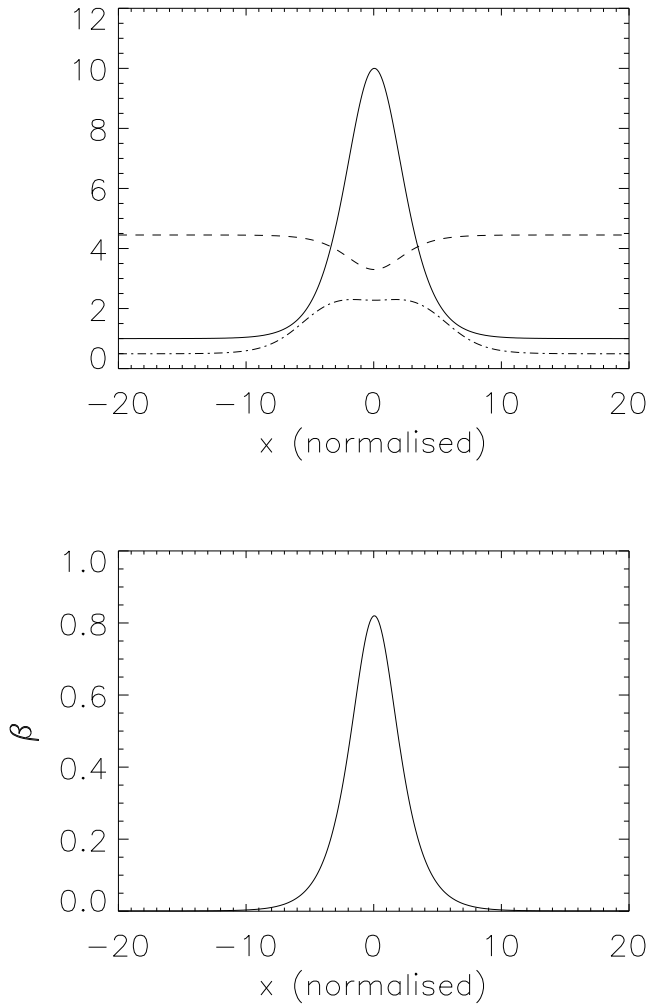

Figure 3.3: Top panel: plot of the normalised initial parameters as a function of the transverse coordinate. The solid line is the density, the dashed line is the magnetic field B_y, and the dot-dashed line is the temperature. The temperature has been multiplied by a factor of 5 for clarity. Bottom panel: the β profile resulting from the parameters shown in the top panel.

boundaries were applied in the transverse direction.

Theoretically, any excitation of a mode in this way would lead to the excitation of higher harmonics [Terradas et al., 2005]. However, the excitation we choose is always sufficiently close to the eigenmode that the amplitude of these harmonics is very small with respect to the fundamental oscillation, and they are quickly damped. Thus, by running the simulation for sufficient time, the dominance of the desired mode is ensured [Pascoe et al., 2007a].

In addition to generating the sausage mode, it is also possible that a longitudinal slow mode may be generated in the loop. Although this is not a significant factor when β_0 is low, the effects of this mode may become more important as β_0 is increased. However, in almost all cases it would be straightforward to distinguish between this slow mode and the desired sausage mode. The exception to this occurs when the sound speed and the Alfv'en speed in the plasma become equal, when $\beta_0 \approx 1.2$. In this scenario both the sausage mode and the slow mode would be excited, and both modes would have essentially the same properties.

To measure the periods of oscillation, the perturbation of the plasma parameters at the relevant anti-node are studied. For the global sausage mode this is the perturbation of the plasma density at the loop centre. The period is determined by applying a Fourier transform to the time series data from this point, thus the uncertainty in the measurement is connected with the half-width of the peak in the Fourier power spectrum.

3.4 Results

3.4.1 The period of the sausage mode

According to Nakariakov et al. [2003], the period of the global sausage mode in the trapped regime is given by:

$$P_{GSM} \approx \frac{2L}{C_{\rm p}}, \tag{3.11}$$

where L is the loop length and $C_{\rm p}$ is the phase speed, which ranges between the Alfvén speed at the loop centre and at infinity. More recently, this relation was shown to be a valid approximation in the leaky regime [Pascoe et al., 2007a] where $C_p \approx C_{Ae}$, and in a loop with variable cross-section Pascoe et al. [2009]. However, in both cases this relation was tested for very low values of β_0. It is unclear whether or not a significant value of β_0 would have a strong effect on the period of the mode. As a first step therefore, we reproduce the result of Pascoe et al. [2007a] showing the dependence of the period on the loop length L, but this time for a variety of β_0 values. This is achieved by simulating sausage oscillations in a loop with an Epstein density profile and a density contrast ratio of $\rho_0/\rho_e = 10$.

The results shown in Figure 3.4 are in excellent agreement with those presented in Pascoe et al. [2007a]. Above approximately 20 Mm the mode becomes leaky and the phase speed is slightly higher than the external Alfvén speed. Furthermore, the near-independence of the oscillation period on β_0 is clear. As a further illustration, we investigate the period dependence on β_0 at a fixed length L. The length of the loop was set at L=15 Mm - corresponding to trapped modes - and the value of β_0 was varied as described in Section 3.3. β_e was kept constant and small throughout. The result is displayed in Figure 3.5.

The period of the sausage mode should also depend on the loop width a. This is due to dispersion, since a change in a essentially corresponds to movement along the dispersion curve derived from Equation 3.5 (see Figure 2.2) and hence a change in phase speed C_p. To illustrate this, we performed numerical simulations of a sausage mode in a loop of fixed length L=15 Mm while varying the width of the Epstein profile. The results are illustrated in Figure 3.6. As expected, the period increases as a function of a within the trapped regime, whereas for leaky modes - corresponding to $a < 2.2$ Mm - the period tends to a constant value. This is a consequence of the phase speed

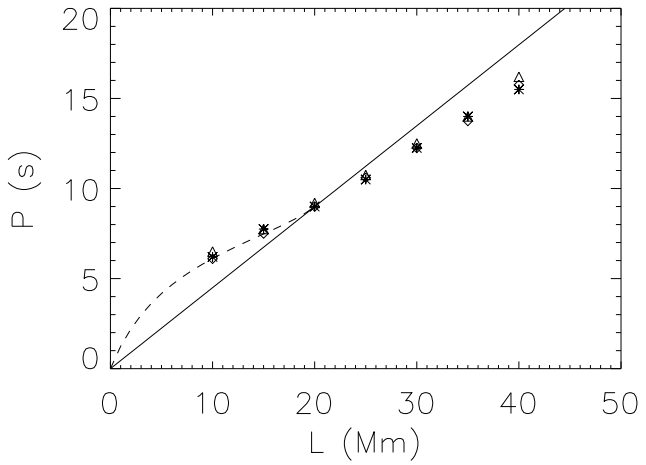

Figure 3.4: Period of the global sausage mode as a function of loop length L, for a number of β_0 values. The stars correspond to β_0=0.005, the diamonds to β_0=0.08 and the triangles to β_0=0.82. Other values of β_0 were omitted for clarity. The solid line corresponds to $2L/C_{\rm Ae}$, while the dashed line is the analytical solution to the dispersion relation for an Epstein density profile. The density contrast ratio is 10. The error bars here are too small to be visible.

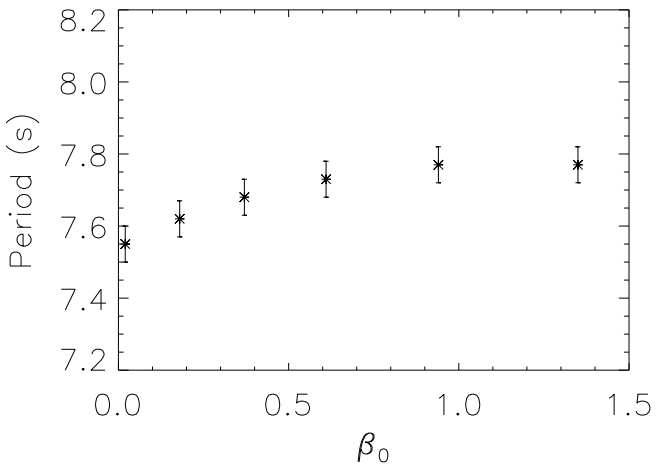

Figure 3.5: The sausage mode period dependence on β_0 for a trapped mode in a loop of length L=15 Mm. The density contrast ratio is 10.

remaining close to the external Alfvén speed in this regime.

It is clear from these results that, although there is a slight increase in the period with respect to β_0, the variation is very small (less than 5%) compared to the effect of other parameters such as loop length. Thus we may say that the period of the sausage mode is very stable with respect to the value of β_0.

3.4.2 The second longitudinal harmonic

An often-neglected aspect of sausage mode behaviour is the relationship between the periods of separate harmonics. For dispersionless standing modes in a resonator, the frequency of the N-th harmonic is simply N times that of the fundamental. Being strongly dispersive, the sausage mode harmonics deviate significantly from this pattern.

The true behaviour of the harmonic ratio is explored for the fundamental and second harmonic modes. For a given value of k_1 (the wavenumber corresponding to the fundamental mode), the period ratio $P_1/2P_2$ is measured from numerical simulations.

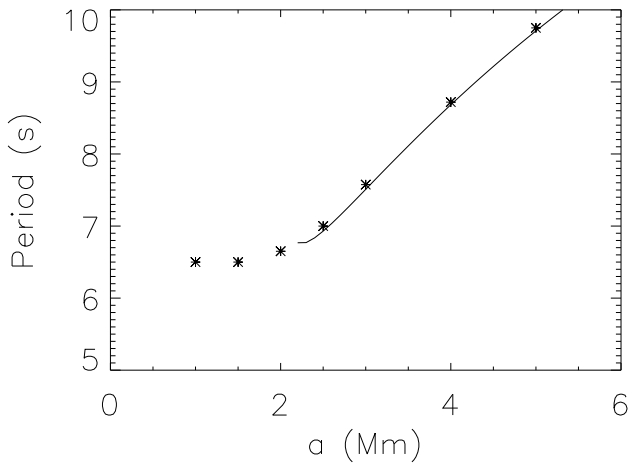

Figure 3.6: The sausage mode period dependence on width a for a loop of fixed length L=15 Mm, where the density contrast ratio is 10. The solid line corresponds to the solution of the dispersion relation for an Epstein profile.

By varying the loop length L, we control the wavenumber k_1 and subsequently measure the period ratio as a function of k_1. Figure 3.7 displays the results.

For non-dispersive waves, the expected ratio of $P_1/2P_2$ is 1. It is clear that the sausage mode harmonics do not follow this pattern. For large values of k_1 corresponding to the uniform plasma (and hence dispersionless) limit, the ratio does indeed tend towards the ideal value. However, for smaller k_1, the period of the second harmonic becomes a much greater fraction of the fundamental period, as illustrated in both panels of Figure 3.7. The top panel shows the quantitative difference between simulations of an Epstein profile (diamonds) and a step-function profile (stars). Although this deviation is noticeable at low k_1 values, the overall behaviour remains the same, as expected. The solid line shows the theoretical curve for a zero-β Epstein profile derived from the dispersion relation in Equation 3.5. The agreement between the theoretical and numerical results is impressive. The bottom panel of Figure 3.7 shows how the density contrast ratio between the loop and the surroundings effects the behaviour of the period

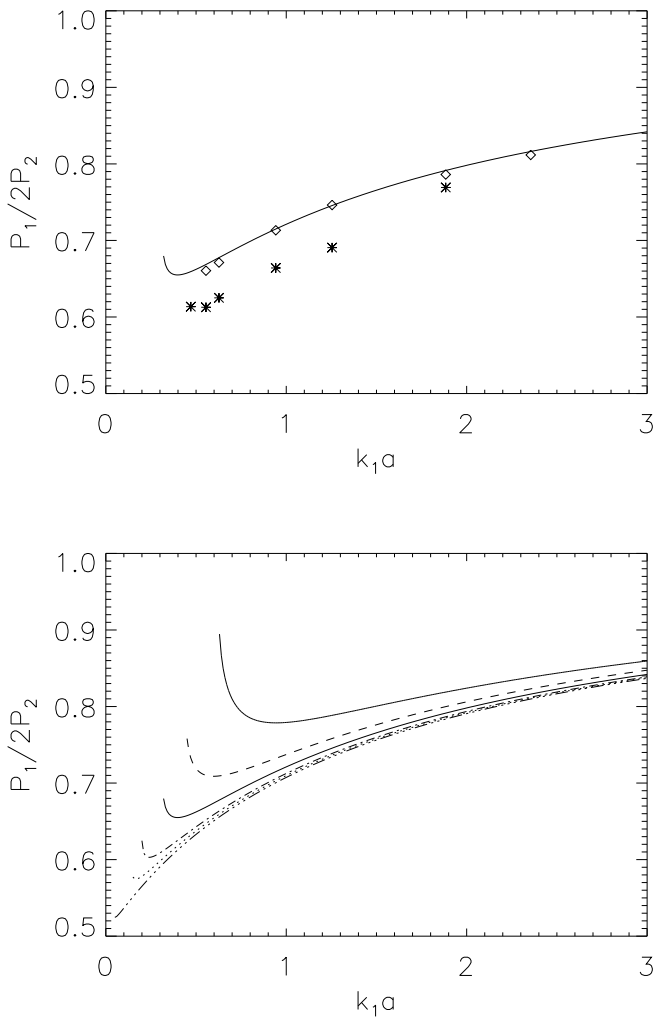

Figure 3.7: Top panel: The ratio $P_1/2P_2$ observed via full numerical simulation for the sausage mode as a function of the longitudinal wave number k_1 for both the step-function (stars) and Epstein profile (diamonds) geometries. The density contrast ratio is 20 and β_0=0.08. The solid line is the theoretical curve derived from the dispersion relation for the Epstein profile, also using a density contrast ratio of 20. Bottom panel: Illustration of the dependence of the analytical solution on the density contrast ratio. The solution is shown for contrast ratios of 5 (lower solid line), 10 (dashed line), 20 (solid line), 50 (dot-dashed line), 100 (dotted line) and 1000 (triple-dot-dashed line).

ratio; the denser the loop, the greater the deviation from the ideal, non-dispersive case. However, the range for the period ratio in all cases lies between 0.5 and 1, even for a density contrast ratio as high as 1000. The turnover of the period ratio curve seen at low k_1 is a product of being very close to the cut-off wavenumber k_c. More precisely, this effect is caused by the fact that, close to the wavenumber cut-off, the gradient of the dispersion curve for the Epstein profile actually becomes shallower, unlike in the cylindrical case shown in Figure 2.2. With reduced dispersion, the deviation of the period ratio $P_1/2P_2$ is actually less pronounced when P_1 is very close to the cut-off period.

In coronal seismology, the ratios of observed oscillatory periods - say, in a coronal loop or solar flare - may be used to make judgements about the underlying MHD modes. Figure 3.7 provides a powerful illustration of the dispersive nature of sausage mode harmonics, and that for entirely realistic values of k it is not expected that the harmonic ratio be close to 1 regardless of any non-uniformity in the longitudinal direction.

3.4.3 The cut-off wavenumber

According to Nakariakov and Roberts [1995a], the cutoff wavenumber for a sausage mode in a magnetic slab with a step-function profile of finite-β plasma is given by:

$$k_c a = \frac{\pi}{2}\sqrt{-\frac{\left(1+\frac{C_{\rm s0}^2}{C_{\rm A0}^2}\right)\left(\frac{C_{\rm s0}^2}{C_{\rm A0}^2+C_{\rm s0}^2}-\frac{C_{\rm Ae}^2}{C_{\rm A0}^2}\right)}{\left(1-\frac{C_{\rm Ae}^2}{C_{\rm A0}^2}\right)\left(\frac{C_{\rm s0}^2}{C_{\rm A0}^2}-\frac{C_{\rm Ae}^2}{C_{\rm A0}^2}\right)}}, \tag{3.12}$$

An analytical expression for the wavenumber cut-off does not exist in the finite-β case for the symmetric Epstein profile. The expression (Pascoe et al. 2007) can only be strictly derived when β=0. Therefore for consistency all analysis of the cut-off wavenumber is carried out in step-function geometry.

In order to investigate the dependence of this cut-off wavelength on the plasma-β, we write the sound speed as $C_{\rm s}^2/C_{\rm A}^2 = \gamma\beta/2$. Eq. 3.12 then becomes:

$$k_c a = \frac{\pi}{2}\sqrt{-\frac{\left(1-\frac{C_{\rm Ae}^2}{C_{\rm A0}^2}\right)\frac{\gamma\beta_0}{2}-\frac{C_{\rm Ae}^2}{C_{\rm A0}^2}}{\left(1-\frac{C_{\rm Ae}^2}{C_{\rm A0}^2}\right)\left(\frac{\gamma\beta_0}{2}-\frac{C_{\rm Ae}^2}{C_{\rm A0}^2}\right)}} \tag{3.13}$$

$$= \frac{\pi}{2}\sqrt{-1+\frac{\left(\frac{C_{\rm Ae}^2}{C_{\rm A0}^2}\right)^2}{\left(1-\frac{C_{\rm Ae}^2}{C_{\rm A0}^2}\right)\left(\frac{\gamma\beta_0}{2}-\frac{C_{\rm Ae}^2}{C_{\rm A0}^2}\right)}} \tag{3.14}$$

Using the equation for magnetostatic pressure balance (Eq. 3.2), we can eliminate $C_{\rm Ae}/C_{\rm A0}$ and write the expression for the cut-off wavelength in terms of the density contrast $\zeta = \rho_0/\rho_{\rm e}$ and the plasma-β. We find

$$\frac{C_{\rm Ae}^2}{C_{\rm A0}^2} = \zeta\left(1+\beta_0\right) - \beta_{\rm e}.$$

Inserting this expression into Eq. 3.14, we obtain

$$k_c a = \frac{\pi}{2}\sqrt{-1+\frac{\left(\zeta\beta_0-\beta_{\rm e}+\zeta\right)^2}{\left(\zeta\beta_0-\beta_{\rm e}+\zeta-1\right)\left((\zeta-\frac{\gamma}{2})\beta_0-\beta_{\rm e}+\zeta\right)}} \tag{3.15}$$

This dependence is shown in Figure 3.8. For any value of β_e, $k_c a$ is seen to decrease as a function of increasing β_0. Realistically, in a coronal plasma the external β_e is likely to be small. Thus we will concentrate on this region of the surface.

By comparison, we numerically evaluate Equation 3.12 for increasing values of β_0, while maintaining a fixed and low β_e. We maintain fixed external values of ρ and B. Inside the loop, the value of B is decreased, increasing the value of β_0. For the structure to remain stable, the internal gas pressure must be left a free parameter to maintain total pressure balance. As before, the temperature is allowed to vary with the gas pressure, ensuring that the simulated loops are hot and dense. The results are shown in Figure 3.9.

In both cases, the value of the cut-off wavenumber clearly decreases while β_0 is increased from 0 to 1. The bottom panel of Figure 3.9 shows the same result for a number of different density contrast ratios, illustrating that the density has a strong impact on the confinement of the sausage mode. Again though for any starting - and

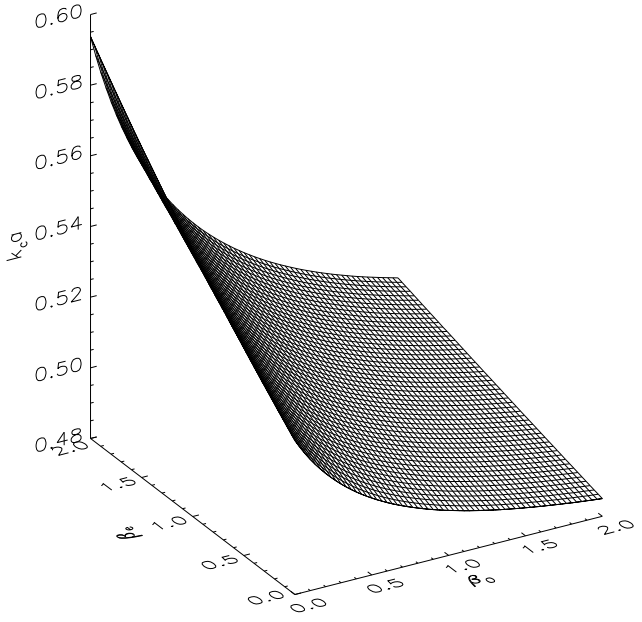

Figure 3.8: Surface showing the dependence of the cut-off wavenumber on β_0 and β_e. The density contrast ratio is 10.

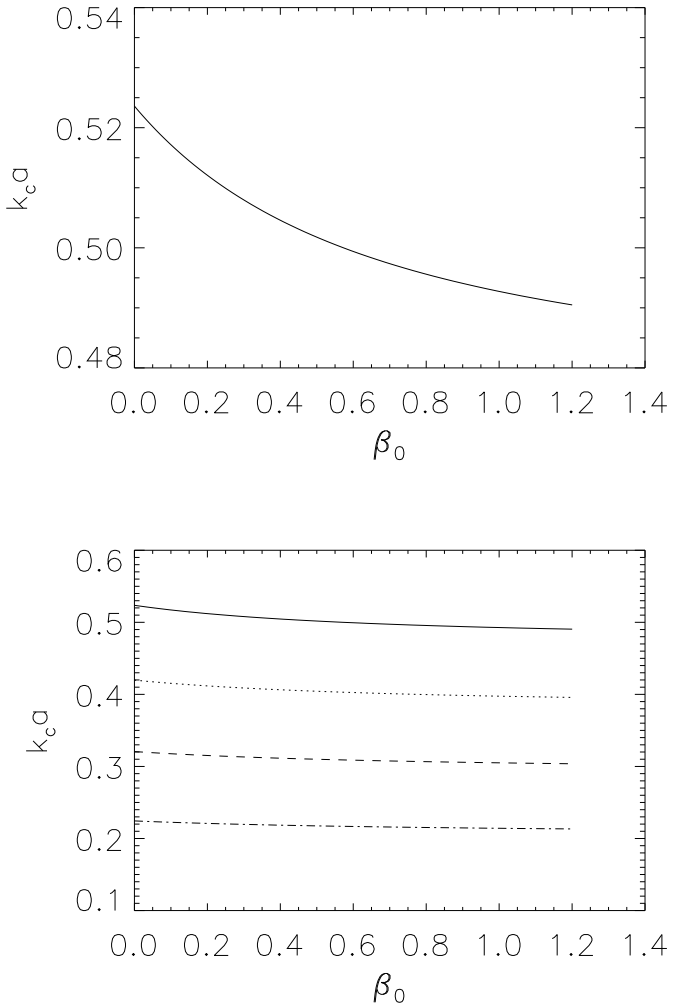

Figure 3.9: Plot showing the dependence of $k_c a$ on β_0 for a fixed value of β_e, where β_e is small. Top panel: for density contrast ratio of 10. Bottom panel: Density contrast ratios of 10 (solid line), 15 (dotted line), 25 (dashed line) and 50 (dot-dashed line).

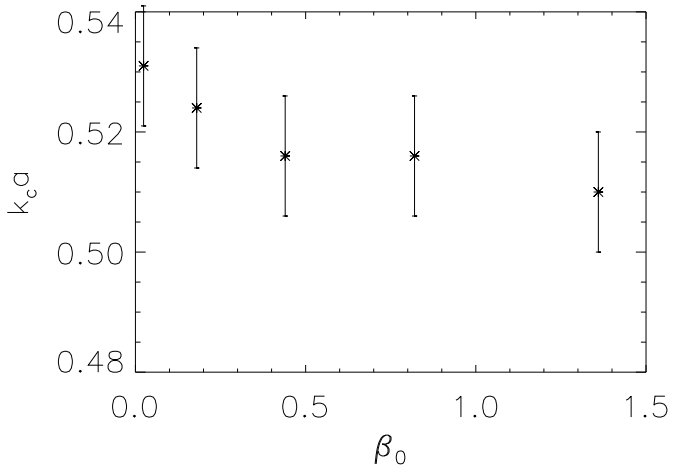

Figure 3.10: Full MHD simulations of the global sausage mode in slab geometry, showing the cut-off wavenumber as a function of β_0, where the density contrast ratio is 10.

fixed - value of the density contrast, the cut-off wavenumber will decrease as a function of β_0.

To further corroborate these results, we perform full numerical simulations of the global sausage mode for varying values of β_0. This is achieved by controlling the internal magnetic field as explained in Section 3.3.

To measure the cut-off wavenumber itself, we simulate the global mode for varying L (and hence k) and examine the time series of the loop anti-node as described in Section 3.3. Here the criterion for a mode to be leaky is that the amplitude of the oscillation inside the loop is damped. When far into the leaky regime, the damping effect is strong and evident [see for example Pascoe et al., 2007a]. However, closer to the trapped regime it can be difficult to ascertain whether significant damping is taking place. This effect is mitigated by running the simulations for a sufficiently long time. However an exact determination of the cut-off wavenumber k_c remains difficult.

The results of these MHD simulations are presented in Figure 3.10. The simula-

tions show the same general trend as the analytical and numerical solutions of equation 3.12, although the agreement is not exact. The curve of the simulated result is noticeably shallower than the theoretical predictions. In part this is likely due to the difficulty in determining exactly the transition between the trapped and leaky regimes, a problem that is reflected in the size of the error bars in Figure 3.10. In fact, despite the convention of referring to $k_c a$ as an absolute value, it may be better to consider the region near the cut-off wavenumber as a transitory area of finite width, where the mode is neither clearly trapped nor noticeably leaky.

3.5 Conclusions

Using numerical simulation and analytical study, we have carried out detailed analysis encompassing various aspects of MHD sausage mode behaviour. The key findings may be summarised as follows:

1. The period of the global sausage mode was found to be determined by the length of the loop L, which confirmed previous findings of Nakariakov et al. [2003] and Pascoe et al. [2007a].

2. In the trapped regime the period is also dependent on the loop width a due to dispersion, but becomes weakly dependent in the leaky regime.

3. The period of the global sausage mode is not significantly affected by finite values of β_0, with the variation remaining less than 5% for $0 < \beta_0 < 1$.

4. The ratio between the second longitudinal harmonic and the fundamental, $P_1/2P_2$, varies between approximately 0.5 and 1 for 'reasonable' values of k_1 and ρ, and is strongly dependent on both k_1 and ρ.

5. The cut-off wavenumber for the global mode is a function of β_0, β_e and the density contrast ratio ζ. For a given density and β_e, the $k_c a$ is a decreasing function with respect to β_0.

Analysis of the cut-off wavenumber k_c reveals the limiting factors dictating whether an MHD mode remains trapped or becomes leaky. The unambiguous result is that the density contrast between the loop itself and the surroundings is the most important factor. For extremely dense loops, a sausage mode may remain trapped even for very long loop lengths. Conversely, for loops of modest density, it is clear that trapped modes may only be supported for comparatively short lengths. The values of β_e and β_0, although also factors, are secondary ones. It was shown in Section 3.4.3 that k_c decreases as a function of β_0 when β_e and ζ are treated as constants. In more physical terms, this means that the maximum length supporting trapped modes, L_c, is increased. However, this variation is clearly small when compared to the effect of the density contrast ratio ζ (see Figure 3.9).

These results also have practical applications in the context of MHD coronal seismology. For multi-periodic oscillations, an understanding of the relationship between sausage mode harmonics enables informed judgements about the nature of the observed mode.

For example, in Srivastava et al. [2008] during observations of a post-flare loop in the $H\alpha$ range, a period ratio of $P_1/2P_2 \approx 0.83$ was reported, with the favoured interpretation being the fundamental and second harmonic of the sausage mode. From their estimates of the loop length ($L \approx 100$ Mm) and our independent estimate of the loop width ($a \approx 8$ Mm), it is possible to examine this conclusion. Given the values of L and a, we estimate that $k_1 a \approx 0.25$. It is clear from Figure 3.7 that, for the period ratio reported this is very much in the leaky regime for the sausage mode. However, the data presented in Srivastava et al. [2008] does not show significant evidence of damping. Therefore, although it must be pointed out that the uncertainty in $k_1 a$ is considerable, it seems that the observed $P_1/2P_2$ is an indication that another mode may be responsible.

We apply the same analysis to the event studied in Nakariakov et al. [2003], where a fundamental and possible second harmonic was reported while observing a flaring loop in the microwave range with the Nobeyama Radioheliograph. In this case the observed

period ratio is $P_1/2P_2 = 0.82 \pm 0.15$. Given the published estimates of the loop length ($L \approx$ 25 Mm) and width ($a \approx$ 6 Mm) we find that in this case $k_1 a \approx 0.75$. Again, we can compare this with the results shown in Figure 3.7. In this case, the observed period ratio and wavenumber are broadly consistent with a trapped fundamental and second harmonic of the sausage mode, provided the density contrast ratio is not too large, say 5 or perhaps even 10. These two examples show how the results obtained here can be readily applied to observational examples of multi-period QPP.

Nevertheless, significant scope for improvement remains, both in observational and theoretical terms. In general, the uncertainties in both P_2/P_1 and $k_1 a$ are substantial in observational studies of QPP. Additionally, as has been shown in Figure 3.7, the geometry of the theoretical model has a bearing on the quantitative values of the period ratio. Potentially important effects such as loop curvature and gravity have also been neglected in this study. Understanding the impact of these effects may prove an important next step in quantifying the characteristics of sausage modes.

Chapter 4

Spatially resolved observations of QPP in flares

4.1 Introduction

In Chapter 2 the concept of quasi-periodic pulsations (QPP) in flares was introduced, along with the various theories behind the phenomenon and possible interpretations. One of the main theoretical MHD modes that causes QPP, the sausage mode, was then examined in detail via numerical and analytical methods in Chapter 3. In this chapter we turn our focus to the observational aspects of QPP. It has already been emphasised in Section 2.3 that, where possible, spatially resolved analysis should be utilised to correctly interpret pulsations in flares, or at least to exclude some mechanisms. Here we justify this statement via analysis of a QPP event observed simultaneously in microwaves and hard X-rays. The ultimate intention is to gain insight into the mechanism responsible for the periodic modulation of the emission. The flare discussed here is a GOES M-class event which occurred on the 8th May 1998 on the solar limb. It was observed by the Nobeyama Radioheliograph and the Nobeyama Radiopolarimeters, and by the Yohkoh, SOHO and GOES satellites. This event was first analysed by Stepanov et al. [2004], who found a 16 s periodicity and suggested that it was caused by an MHD ballooning mode.

Here, detailed analysis and an alternative interpretation of this event are presented. The results of this analysis were published in Inglis et al. [2008].

4.2 Analysis of integrated light curves

4.2.1 The periodogram technique

Here it is convenient to introduce one of the robust and widely-used time series analysis techniques: the periodogram. Although not a recent innovation, the periodogram has been subject to detailed scrutiny, in particular by Lomb [1976] and Scargle [1982], and is consequently a well-understood and reliable method. The basic assumption of the periodogram is that a time series can be considered as the sum of a signal, $X(t)$ and random noise $R(t)$ as follows:

$$Y(t) = X(t) + R(t) \tag{4.1}$$

The Scargle periodogram [Scargle, 1982] is then defined as:

$$P_x(\omega) = \frac{1}{2}\left(\frac{\left[\sum_j Y_j \cos\omega(t_j-\tau)\right]}{\sum_j \cos^2\omega(t_j-\tau)} + \frac{\left[\sum_j Y_j \sin\omega(t_j-\tau)\right]}{\sum_j \sin^2\omega(t_j-\tau)}\right), \tag{4.2}$$

where

$$\tan(2\omega\tau) = \frac{\left(\sum_j \sin 2\omega t_j\right)}{\left(\sum_j \cos 2\omega t_j\right)}. \tag{4.3}$$

The advantage of this periodogram definition is that the power, P_x is exponentially distributed. It is important to remember however that, since the time series Y is a random variable, P_x is also a random variable. Therefore it follows statistical behaviour. This realisation leads to the concept of the **false alarm probability**, i.e. the likelihood that the peak in a periodogram spectrum is the result of random chance rather than a

real signal. Because the power in a periodogram is exponentially distributed, the power level corresponding to a particular false alarm probability fraction p_0 can be defined as

$$z_0 = -\ln[1 - (1 - p_0)^{1/N}], \tag{4.4}$$

where N is the number of frequencies in the spectrum. As pointed out by Horne and Baliunas [1986], this is applicable to correctly normalised signals only, i.e. signals normalised by the total variance. This definition has become a powerful tool for the analysis of noisy or limited-resolution data. Both such conditions are typical of observational flare data. Since the periodogram is noisy, cautious confidence levels are usually adopted when using this technique, typically 95% or 99%, corresponding to p_0 = 0.05 and p_0=0.01 respectively.

A further advantage of the periodogram is that it can be utilised on unevenly sampled data, unlike a Fast Fourier Transform (FFT). This is particularly convenient in an astronomical context, where observations are frequently interrupted or curtailed.

4.2.2 Microwave time profiles

The time profile of the microwave flux integrated over the whole flaring region (the light curve), recorded by NoRH at 17 GHz, is shown in Figure 4.1. The signal is averaged over 1 s. The time profile shows that this was a single burst event beginning at 01:57 UT. Quasi-harmonic oscillations of large modulation depth are evident immediately after the beginning of the flare. These oscillations do not appear in Nobeyama's complementary 34 GHz frequency band, most likely due to the low signal-to-noise ratio.

The presence of the pronounced periodicity is also seen in the lower frequency channels observed by the Nobeyama Radiopolarimeter (see Figure 4.1, bottom panel). The oscillations in different channels are seen to be coincident.

The high quality of the observed oscillation is confirmed by the spectrum of the analysed signal. Subtracting the running mean smoothed by 20 s from the signal recorded at 17 GHz by NoRH, and applying the periodogram technique described in Section 4.2.1,

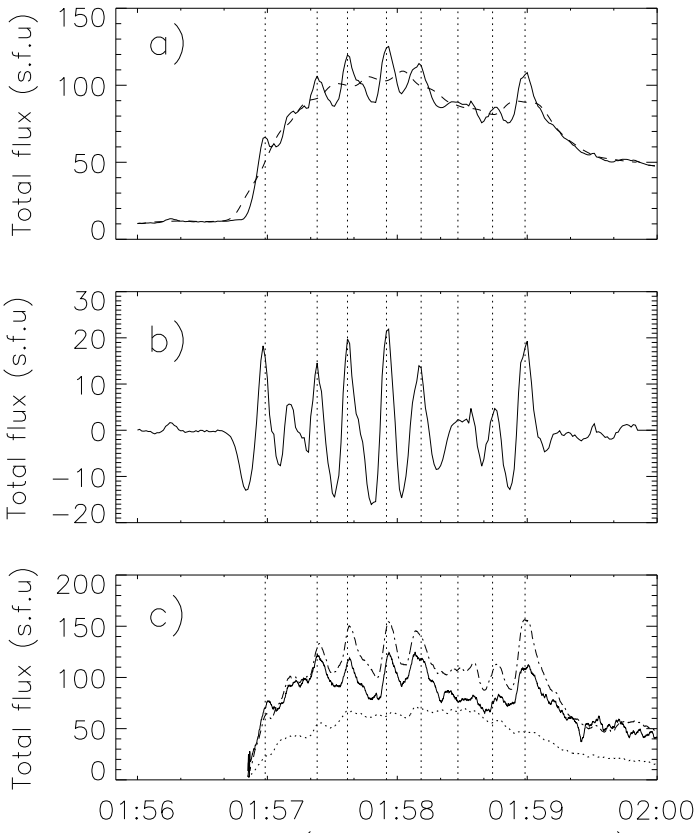

Figure 4.1: *a)*: Integrated flux time profile of microwave emission at 17 GHz for the solar flare of 8th May 1998, as observed by NoRH. Overlayed with the dashed line is the background emission profile obtained via 20 s smoothing of the integrated flux signal. *b)*: The signal after subtraction of the background profile from the integrated flux. *c)*: Solar flux time profiles of microwave emission at 9.4 GHz (dot-dashed line), 17 GHz (solid line) and 3.75 GHz (dotted line), obtained by the Nobeyama Radiopolarimeters.

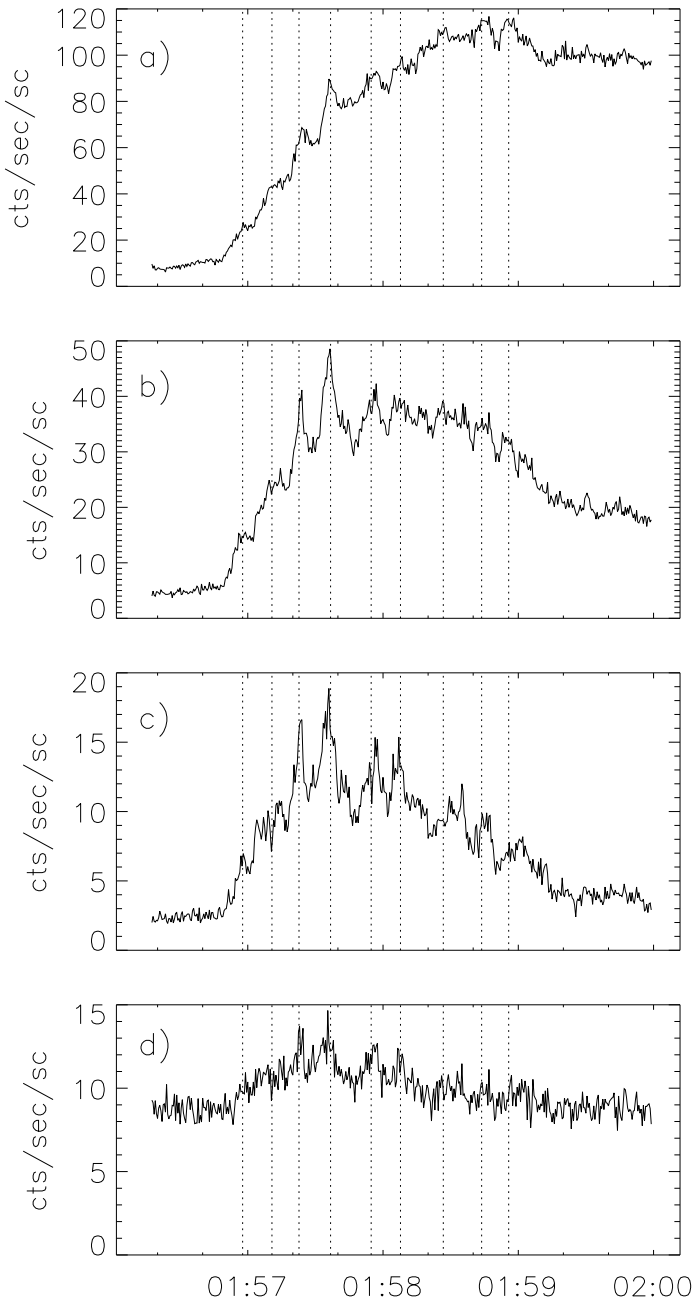

Figure 4.2: Hard X-ray light curves from the Yohkoh satellite, observing the solar flare of 8th May 1998. *a)*: X-ray counts in the L (13 - 23 keV) range, *b)*: X-ray counts in the M1 (23 - 33 keV) range, *c)*: X-ray counts in the M2 (33 - 53 keV) range, *d)*: X-ray counts in the H (53 - 93 keV) range.

we obtain the power spectrum with a pronounced peak of 16 s (Figure 4.3). The removal of the smoothed signal is equivalent to the removal of the low frequency component of the signal in the spectral domain, which is connected with the long period trend. The level of smoothing to be subtracted always represents a compromise between adequately removing the background signal and preserving the oscillatory pattern. Removal of this background trend is essential as it prevents the spectrum of the periodogram from being dominated by the lowest frequencies. One of many alternative approaches is to use a bandbass filter to suppress frequencies below a certain value in the frequency domain. This is the approach that we adopt later in Chapter 5.

The observed period concurs with the findings of Stepanov et al. [2004]. The peak is found to be well above the 99% confidence level calculated according to Horne and Baliunas [1986]. The main spectral peak is surrounded by secondary peaks. To check whether the secondary peaks appeared because of the finite duration of the sample, we calculated the spectra of the smoothed signals multiplied by the Hann and Blackman-Harris [Blackman and Tukey, 1959] window functions (see Figure 4.3). This increases the amplitude resolution of the spectrum on the expense of the frequency resolution. According to the Figure, the use of a window function clearly suppresses the spectral sidelobes of the peak, indicating that they may be artificial rather than real in nature.

4.2.3 Hard X-ray time profiles

The impulsive burst of emission from this flare was also detected by the Hard X-ray Telescope (HXT) on board Yohkoh. Microwave and hard X-ray time profiles often show strong correlation during flares [Asai et al., 2001]. Four light curves corresponding to the available Yohkoh energy bands are shown in Figure 4.2.

There is clear evidence of oscillations in the L (13-23 keV), M1 (23-33 keV) and M2 (33-53 keV) channels. A periodogram analysis on the modulation depth in hard X-rays reveals a period matching that of the microwave emission above the 90% confidence level in both the L and M1 energy channels. The Scargle periodogram of

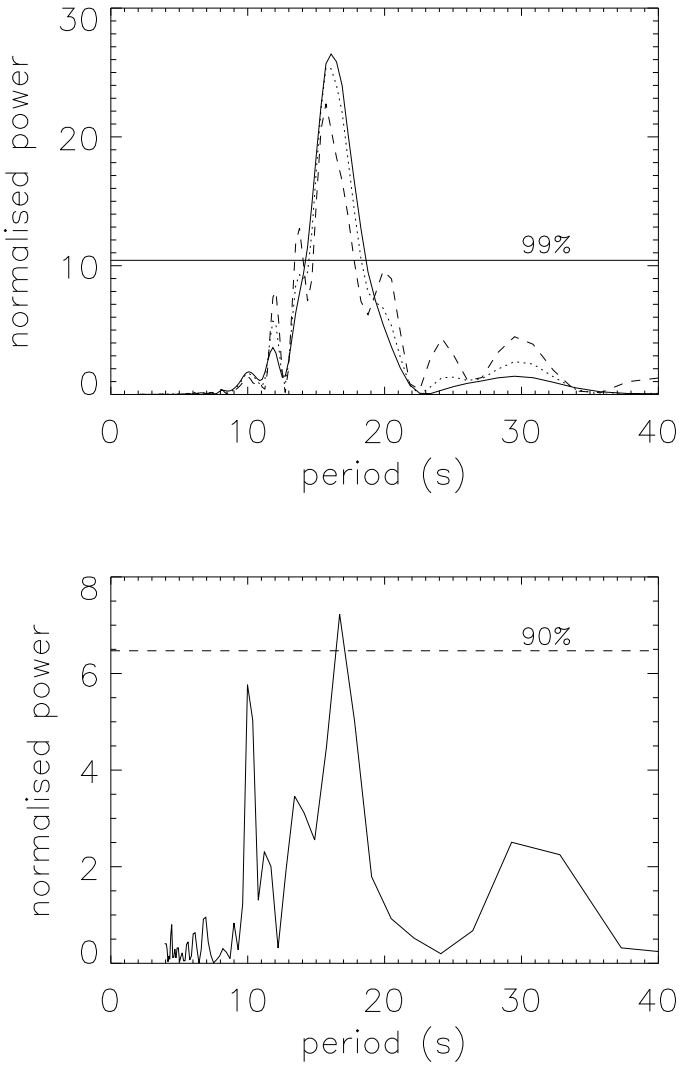

Figure 4.3: Top panel: Lomb-Scargle periodogram [Scargle, 1982] of the 17 GHz modulation depth from the Nobeyama Radioheliograph. *Dashed line*: periodogram without a window function; *dotted line*: periodogram using a Hann window function; *solid line*: periodogram using a Blackman-Harris window function. The periodogram reveals a oscillation period of 16 s, above the 99% confidence level. Bottom panel: Lomb-Scargle periodogram of the M1 (23-33 keV) X-ray modulation observed by the Yohkoh satellite.

the oscillation in the M1 channel is shown in figure 4.3. The count rate in the M2 band is too low for a reliable detection, while the H channel observes little above the background level, consistent with an M-class flaring event.

4.3 Locations of emission sources

Both the NoRH and HXT allow for spatial resolution of the microwave and hard X-ray emission sources, respectively. The location of the various types of emission from a flare have implications for the theoretical model. According to the standard flare model described in Section 1.3.1, magnetic reconnection is supposed to take place above the loop top. Hard X-ray emission is expected at the two footpoints of the flaring loop as a result of the interaction of non-thermal electrons accelerated in the flare with dense plasmas. A third source may also be present at or above the loop top [Masuda et al., 1994]. The source of the microwave emission generated by non-thermal electrons by the gyrosynchrotron mechanism is usually situated at a segment of the loop and is strongly dependent on the line-of-sight (LOS) angle with the local magnetic field. Soft X-rays from solar flares are due to thermal emission from the hot plasma which fills the flaring loop. Consequently, soft X-ray images can provide information about the geometry of the flaring region.

A soft X-ray image of the flare provided by the Yohkoh satellite using the Al12 filter is shown in Figure 4.4 with the 17 GHz microwave emission source from the same time overlayed. We perform the overlay in SolarSoftWare (SSW) using the `plot_map` procedure. The soft X-ray images from Yohkoh are prepared using the `sxt_prep` routine, while the Nobeyama Radioheliograph images are prepared using `fits2map`.

The microwave emission is seen to take the form of a single source. This source coincides with the maximum emission of the soft X-ray loop, near the southern footpoint. Figure 4.5 shows the soft X-ray images with the hard X-ray emission sources from the L (13 - 23 keV), M1 (23-33 kev), and M2 (33 - 53 kev) channels overlayed. The images indicate that the flare is located on the solar limb. This concurs with the observations

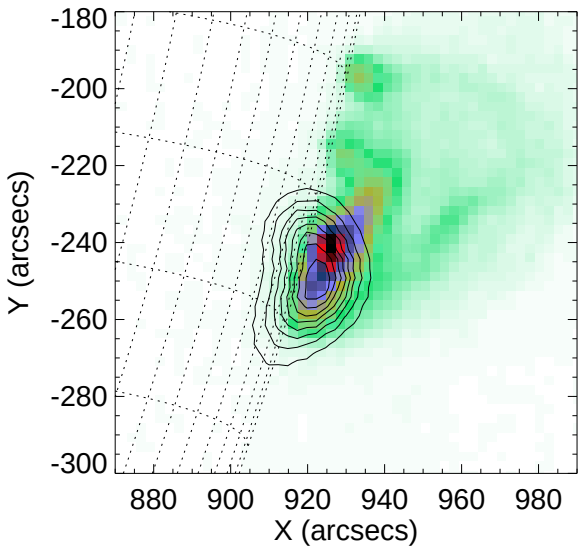

Figure 4.4: Image: Soft X-ray image from the Yohkoh satellite of the flare of 8th May 1998. Contour: microwave emission source for the same flare, observed by the Nobeyama Radioheliograph at 17GHz.

made by the Extreme Ultraviolet Imaging Telescope (EIT) on board SOHO, shown in Figure 4.6. For this image, the EIT data was prepared using the `eit_prep` routine, while the differing observation angle of SOHO was compensated for using `map2earth`.

The sources of different hard X-ray channels have different structures. The low energy channel emission is similar to the soft X-ray structure and is centred around a single maximum near and a little above the centre of the soft X-ray loop, indicating that this emission is thermal in nature. The higher energy channels however reveal the presence of multiple emission sources. The M1 and M2 channels both show a southern footpoint located at (920,-270) arcseconds. The presence of the second (northern) footpoint is also expected from the standard flare model. Although emission from the northern loop footpoint is tentatively seen in the M2 - and sometimes in the M1 - channel, centred at (920, -220) arcseconds, this emission is weak and not confidently observed. The reason for the weakness of the source may be explained by the main

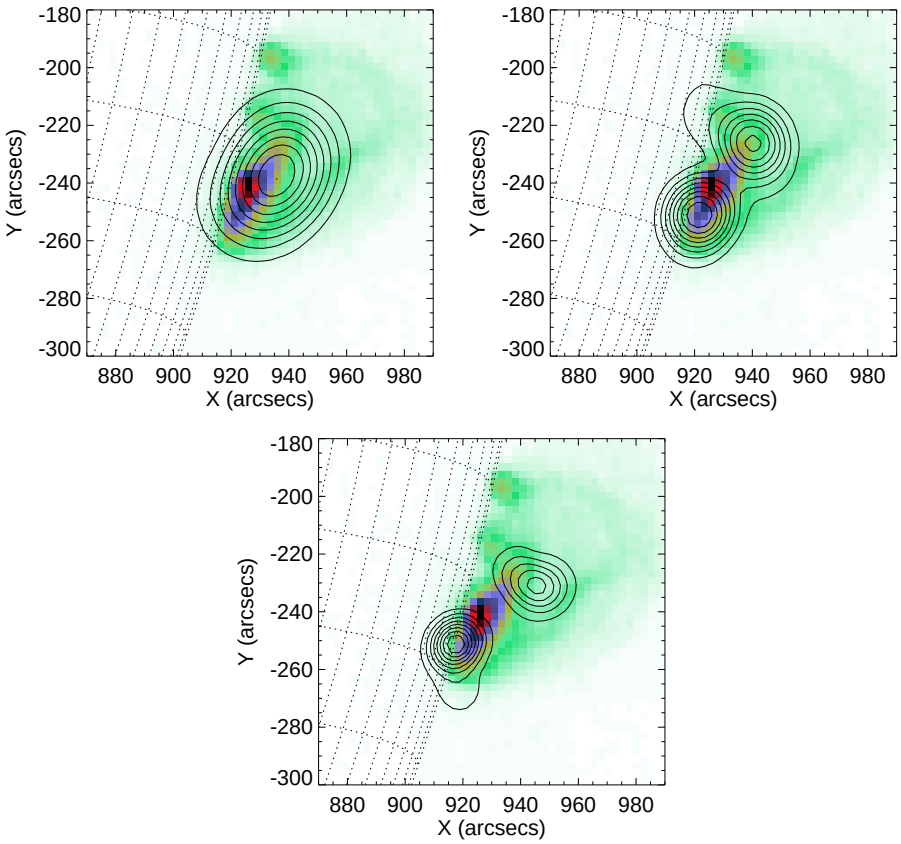

Figure 4.5: Contour maps of hard X-ray emission overlayed on a soft X-ray image of the flaring loop at 01:57:50 UT, during the oscillatory phase. Top: the L (13 – 23 keV) channel, centre: the M1 (23 – 33 keV) channel, bottom: the M2 (33 – 53 keV) channel.

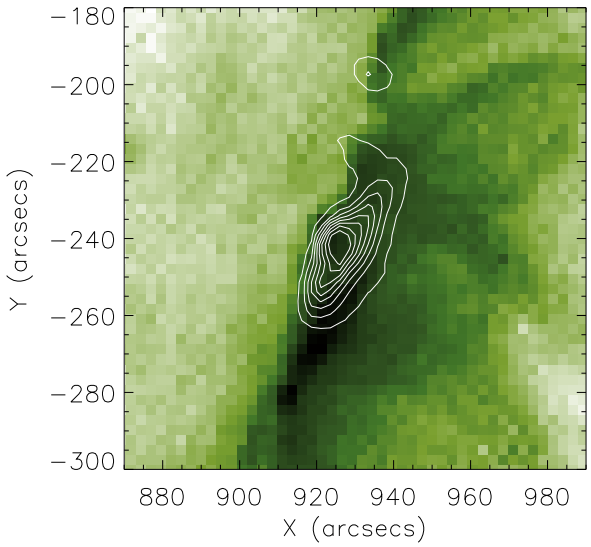

Figure 4.6: Image: SOHO/EIT image of the flare of 8th May 1998. Contour: Soft X-ray loop emission, obtained from the Yohkoh SXT using the Al12 filter.

northern emission site being hidden behind the solar limb. Both high energy channels are also indicative of an emission source coming from above the loop top. This source may be associated with the Masuda-type source [Masuda et al., 1994].

4.4 Spatial Correlation of Time Signals

Determinating of the cause of a QPP event - whether it be an MHD mode, a reconnection event, or any other mechanism - ideally requires the analysis of the spatial structure of the oscillation. An important aspect of this is the phase relationship between the oscillation at different parts of the flaring loop. Since different MHD modes will perturb a loop in different ways, valuable insight can be gained in this way. One of the first successful examples of this was presented in Melnikov et al. [2005], who were able to confirm the presence of an MHD sausage mode during a QPP event.

4.4.1 Periodmaps

The application of the periodmapping technique [Nakariakov and King, 2007] allows us to determine the distribution of the dominating periods in the time series of individual image pixels. Although this technique was originally applied to TRACE data, here we utilise it on 0.1 s time cadence images from the Nobeyama Radioheliograph at 17 GHz. As in this study we are interested in the mode with a period of about 16 s found in Section 2.1, we smooth the time signal of each pixel by 50 frames, which corresponds to 5 s, suppressing the high frequency noise, and then subtract the signal smoothed by 500 frames, which corresponds to 50 s. The latter operation removes the low frequency trend from the data. The periodmap of the data cube obtained in 17 GHz is shown in Figure 4.7. In the map, the colour of a pixel corresponds to the period of the highest peak in the frequency spectrum extracted from the time series of the pixel, provided the spectral power of the peak is 5 times greater than the power averaged over the spectrum. Otherwise, the pixel colour is white. In addition, pixels with integrated signal strengths lower than 7.5×10^{-3} that of the integrated signal from the "strongest" pixel are deemed to be not of interest and are left blank. This operation allows us to subtract the spatial interference pattern which is an artifact of the image synthesis.

The periodmap shows that the period of about 16 s dominates in almost all pixels with time integrated signals stronger than the set threshold. Some pixels near the edge of the region of 16 s oscillations show the presence of higher periodicity. Thus, almost all segments of the flaring loop oscillate with the same period of about 16 s. However, we emphasize that we have not applied a significance level test here - we are only mapping the most significant period for each pixel. Whether these values are truly significant is uncovered using a second test, described in the following section.

4.4.2 Correlation maps

To further investigate the spatial structure and phase of the oscillations, a cross-correlation analysis technique was developed and used. The first step in this process is

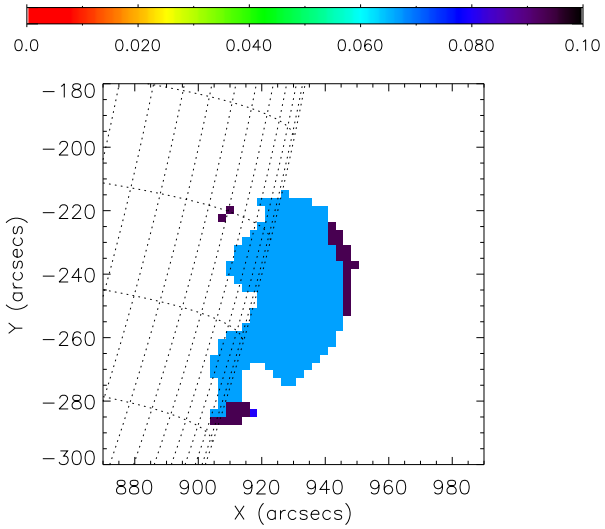

Figure 4.7: Periodmap of the microwave emission at 17 GHz, obtained by the Nobeyama Radioheliograph during the pulsating regime of the limb flare of 8th May 1998. The bar shows the colour coding of the frequencies in Hz.

to generate a relevant datacube. This takes the form of a series of 2D images, hence the result is a data sequence in x, y and t. Next, a pixel with the master (reference) signal is selected, which we shall refer to consistently as the "master" pixel. There is however more than one possible selection criterion for the master pixel. For example, the master pixel can be the pixel with the highest time variance of the signal. Alternatively it may be the pixel with the highest time-integrated intensity, or even the pixel most central to the region of interest. The choice of this pixel is a matter of judgement.

Once the master pixel is selected, for each pixel of the image we calculate the correlation coefficient between the time signal of the pixel and the time signal of the master pixel for a range of different time lags. The correlation coefficient is given by:

$$P_{xy}(L) = \begin{cases} \dfrac{\sum_{k=0}^{N-L-1}(x_{k+L}-\bar{x})(y_k-\bar{y})}{\sqrt{\left[\sum_{k=0}^{N-1}(x_k-\bar{x})^2\right]\left[\sum_{k=0}^{N-1}(y_k-\bar{y})^2\right]}} & \text{for L} < 0 \\ \dfrac{\sum_{k=0}^{N-L-1}(x_k-\bar{x})(y_{k+L}-\bar{y})}{\sqrt{\left[\sum_{k=0}^{N-1}(x_k-\bar{x})^2\right]\left[\sum_{k=0}^{N-1}(y_k-\bar{y})^2\right]}} & \text{for L} \geq 0, \end{cases} \tag{4.5}$$

where x and y are the two datasets, and L is the time lag. This definition is such that two completely uncorrelated signals would return P_{xy}=0, while anti-correlated signals would return negative values of P_{xy}. The total range for P_{xy} is between 1 and -1. Visualising the results obtained with this technique, one can take two approaches; plotting either a map showing the spatial distribution of the correlation coefficient value calculated at a specified time lag, or a map showing the time lags corresponding to the highest values of the correlation coefficient for each pixel.

The top panel of Figure 4.8 is a correlation power map of microwave emission, calculated with zero time lag - $P_{xy}(0)$. As the master pixel we choose the pixel with the maximum value of the time integrated intensity, found near the centre of the loop emission. Here, for clarity and to remove the background interference pattern, we have restricted our attention to areas showing a correlation coefficient power of 0.5 or greater. Pixels with P_{xy} less than 0.5 are blank. The strong correlation throughout the emitting region is evident. The map also reveals some evidence of a loop-like structure.

This power map already provides us with powerful information. It confirms that an oscillation is present throughout the body of microwave emission, which covers a significant spatial area. Since we have constrained the lag L to be zero, it also shows that the oscillation is strongly in phase throughout this area. A certain amount of correlation is to be expected, since the true width of the instrumental beam is much larger than a single pixel here. It automatically follows that nearby pixels will be strongly correlated as they are actually within the same beam diameter, which is approximately 10 arcseconds at 17 GHz. Hence it cannot be said that any structure is clearly resolved in the x-direction. In the y-direction though the spatial exent of the structure is much larger than the beam size of the instrument, so we can say that the loop was easily resolved in this direction.

However, we have not yet guaranteed that the strongest correlation values truly correspond to L=0. This can be tested using a second type of map. The bottom panel of Figure 4.8 shows the spatial distribution of time lags between the time signal from

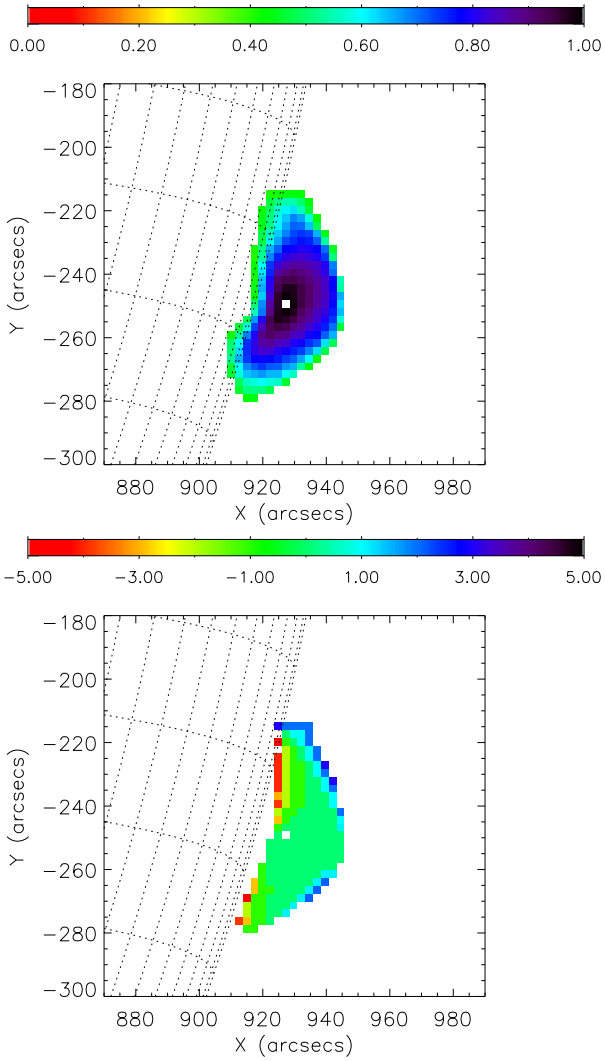

Figure 4.8: Top: Cross-correlation coefficient map for background subtracted microwave emission at 17 GHz, obtained by the Nobeyama Radioheliograph during the pulsating regime of the limb flare of 8th May 1998. The correlation coefficient is calculated with zero time lag. The master pixel is the pixel with the highest time-integrated intensity of the signal. The bar shows the colour coding of the correlation coefficient. Bottom: Correlation time-lag map for microwave emission. The bar shows the colour coding of the time lag in seconds. In both panels the central white point corresponds to the master pixel.

the master pixel and other pixels, which correspond to maximum correlation coefficients. We refer to this as a time lag map. The conclusion is clear; the emitting region appears to be strongly correlated in time, with a maximum shift in time of about 2 s occurring towards the very edge of the region. The vast majority of the emitting area corresponds to L=0.

These two types of map provide a powerful tool when used in tandem. In this example the presence of an oscillation throughout the loop, strongly correlated with zero time lag, has been demonstrated. This information can be used to discriminate between different theoretical QPP mechanisms.

A cross-correlation analysis of the hard X-ray sources was also attempted, but did not succeed in either the M1 or M2 bands. The northern footpoint source is too weak to be meaningfully analysed. The image reconstruction algorithm used by the Yohkoh satellite is also a possible cause of problems, as the satellite relied on collimating optics to pinpoint emission sources. However, in principle the application of this technique to hard X-ray data could yield further interesting information.

4.5 Flare evolution

In order to examine the consistency of this event with standard theoretical models, it is useful to investigate the evolution of the flare emission. Both hard and soft X-ray images can be used for this purpose.

The presence of a stable hard X-ray footpoint throughout the impulsive phase of the flaring emission is clearly illustrated by Figure 4.9. The emission from the loop top is observed to shift in location and become more complex in structure over the same period. After the end of the impulsive phase - at 01:59 - the southern footpoint disappears, leaving only the loop top emission. This emission decays slowly over time, much like the thermal emission in the L (13 - 23 keV) energy channel.

The disappearance of the southern footpoint can be explained by established theory. If hard X-ray footpoints are indeed caused by particles accelerated by energy

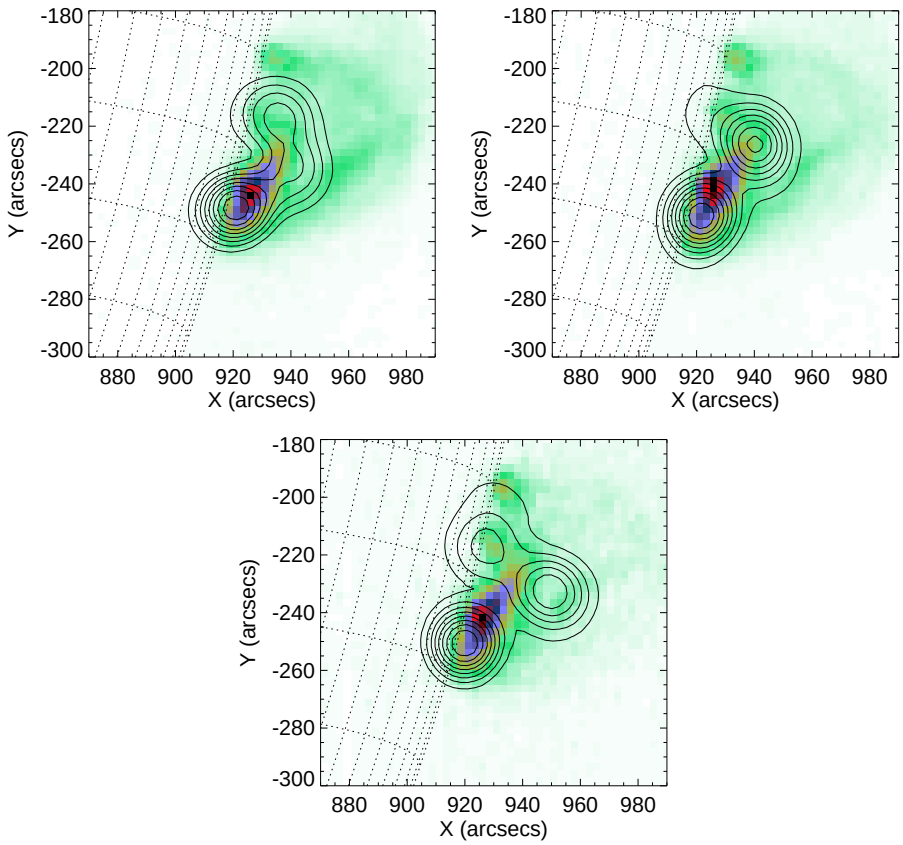

Figure 4.9: Hard X-ray contours from the M1 (23-33 keV) channel overlayed on an SXT image, at 01:57:11, 01:57:49 and 01:58:28 respectively.

release above the loop top and interacting with the photosphere, then it is not surprising that this emission source peters out once the main flare event is concluded. In fact, this observation is entirely consistent with the standard theoretical model described in Chapter 1.

Magnetograms of the active region prior to this event indicate the presence of a single sunspot, without any other obviously connected region, making it difficult to establish whether this was an emergent phenomenon. Yohkoh SXT images do show a slight but steady outward expansion of the flaring loop over time, which would be consistent with such an event.

4.6 Discussion

Quasi-periodic pulsations were clearly observed in both microwaves and hard X-rays for this event. It was also possible to spatially resolve at least two different hard X-ray sources in the higher energy bands of the HXT, located at the southern loop footpoint and the loop top respectively. There is also some evidence of a hard X-ray source at the primary flare's northern footpoint. This is weak and only present at the onset of the impulsive phase. According to the standard flare model two footpoint sources are expected, although these are not necessarily of the same strength. Significant disparities in strength may result from having one footpoint with a strong magnetic field presence while it's counterpart is weak, for example. In this case we opt for the most straightforward explanation and postulate that the main emission site for the northern footpoint is hidden behind the limb of the sun.

In Stepanov et al. [2004] this event was considered as an MHD ballooning mode. The original analysis was based on observed plasma 'tongues' in the microwave images, which were interpreted as ballooning mode perturbations. However, more detailed analysis presented here does not support this interpretation. Periodmapping and the cross-correlation analysis of the microwave emission show that well-correlated oscillations with a period of about 16 s are distributed over the bulk of the loop. Also, evidence of the

characteristic ballooning mode "tongues" was not found in either X-ray or microwave emission, and we believe that the tongues reported in Stepanov et al. [2004] were in fact data analysis artifacts. Thus, we conclude that the observed oscillation is caused by another reason.

We also exclude the interpretation of the observed quasi-periodic pulsations in terms of flare-induced slow magnetoacoustic waves (see, e.g. McAteer et al. [2005]). The observed emission is clearly connected with the non-thermal electrons. It is not clear how a slow wave which is mainly acoustic in nature could affect the dynamics of the non-thermal electrons and hence their precipitation rate. Slow waves can produce the variations of the microwave emission by modulation of the ratio of the plasma frequency to the electron gyro-frequency (see Nakariakov and Melnikov [2006]). However there are no known mechanisms which would link the modulation of the hard X-ray emission with slow waves. A similar problem takes place with interpretation of the observed oscillations of the hard X-ray emission in terms of a kink or torsional mode; they are not thought to significantly affect the non-thermal electron dynamics, although the discussion on this point has recently been re-opened by Fletcher and Hudson [2008].

On the other hand, the sausage mode can produce modulation of the microwave [Nakariakov et al., 2003] and hard X-ray [Zaitsev and Stepanov, 1982] emission. In particular, the global or fundamental mode is a simple broadening and compression of the flare flux tube, with a maximum amplitude at the loop top and nodes at the footpoints. Thus the entire structure would oscillate in phase in this case. The results obtained using the periodmapping technique and the cross-correlation mapping point strongly to this interpretation.

The period of the sausage mode is determined by the loop length. For this event, the loop length was estimated to be between 40–80 Mm. Unfortunately, due to the position of the flare on the limb measurement of the line-of-sight angle is difficult. Soft X-ray and EUV images indicate that there may be more than one loop in this region. In particular, there is some evidence of a second, cool loop above the primary

loop. The northern footpoint of appears from time to time in the soft X-ray band at about (930,-200) arcseconds, although it is not generally a source of hard X-ray emission. Additionally, magnetograms of the active region in the days preceding this event show only a single sunspot. As a result a sunspot pair cannot be used as an alternative length estimate. However, the characteristic period of the oscillations, 16 s, together with this rough length estimate, is consistent with the sausage mode interpretation (see [Nakariakov et al., 2003]). Since we established in Chapter 3 (see equation 3.11) that the period of the global sausage mode - with the wavelength equal to double the loop length - is reasonably estimated by the loop length L and the external Alfv'en speed C_{Ae}, this interpretation yields an estimate of the external Alfvén speed in the range from 5 to 10 Mm/s.

An alternative interpretation of the observed quasi-periodic pulsations could be a periodic regime of magnetic reconnection. In this case, the acceleration of non-thermal electrons is periodically modulated, causing the periodic variation of the non-thermal electron density, and hence the periodic modulation of the microwave and hard X-ray emission. However, it is not clear what would determine the period of the oscillations in this case. One possibility is the periodic triggering of magnetic reconnection by an external oscillating loop ([Nakariakov et al., 2006]). In either case, the theory of this phenomenon needs to be developed. Hence, we cannot exclude this mechanism from consideration.

Useful additional information could in principle be provided by spectroscopic instruments. Unfortunately, the spectral information available for this event is very limited. As mentioned previously, the Nobeyama Radioheliograph registers little above background noise at 34 GHz. Similarly, useful data is only available from the Nobeyama Radiopolarimeters at 3.75, 9, and 17 GHz. The strongest emission is in the 9 GHz band, indicating that the gyrosynchotron turnover frequency is somewhere in this part of the spectrum.

Hard X-ray spectral information is equally limited, as the Yohkoh satellite oper-

ated using only four energy bands, the highest of which observed little above background levels. Therefore, no meaningful spectral analysis is possible.

4.7 Conclusions

In this chapter we have studied in detail an M-class solar flare exhibiting QPP. Imaging studies indicate that it may be considered as a Masuda-type event, as evidenced by a hard X-ray emission source above the loop top. In high energy bands a strong southern footpoint is also observed. The absence of a noticeable northern footpoint in hard X-ray emission is attributed to the footpoint being obscured behind the solar limb. Magnetograms from the SOHO satellite provide evidence that this event was an emergent phenomenon leading to magnetic reconnection. Yohkoh SXT images also show an expansion of the loop over time. These observations are consistent with the standard theoretical model for solar flares.

The analysed flare has perhaps the most pronounced flaring QPP since the famous 8 s period oscillatory event observed on the 7th of June, 1980 [Kane et al., 1983] with ISEE-3 in X-rays and with the Nobeyama Radiopolarimeter in microwaves. In the event analysed here, the high quality 16 s periodicity is seen to be very stable during the flare, and was found to be present in the data with more than 99% confidence. In contrast with the event on 7th of June, 1980, this time spatial information is available, allowing us to determine the MHD mode responsible for the oscillation.

Accordingly, we have developed and applied the technique of cross-correlation mapping. This allowed us to take advantage of the spatial resolution available for this event, and subsequently show that the oscillation was present and highly correlated in all parts of the loop emitting microwaves. The combination of correlation power maps and time lag maps showed that there was little or no phase difference between different loop segments. This helps us to exclude many of the possible interpretations of QPP.

The observed period of 16 s together with an estimate of the loop length is consistent with the interpretation of the QPP in terms of the MHD sausage mode,

which periodically changes the loop cross-section and the magnetic field. In this case the microwave emission is modulated by the periodic variation of the magnetic field in the emitting plasma. As the global sausage mode is a fundamental standing oscillation in the flux tube, all parts of the loop would oscillate in phase, consistent with the observations.

The periodic modulation of the hard X-ray emission can be caused by the periodic modulation of the mirror ratio (the ratio of the magnetic field strength at the apex and the footpoints) because of the variation of the loop cross-section. An alternative interpretation is the periodic modulation of the flaring energy release (either a periodic regime of magnetic reconnection, or periodic triggering of reconnection by an external waves), and hence the particle acceleration by some external oscillation. However, the lack of theoretical models for such mechanisms does not allow us to include or exclude its possible role in the observed phenomenon.

The observed period of 16 s is perhaps a typical period for the global sausage oscillations in flaring regions (e.g. with a similar value obtained in Nakariakov et al. [2003]). This period is significantly shorter than the periods of quasi-periodic pulsations associated with slow magnetoacoustic modes [McAteer et al., 2005; Mitra-Kraev et al., 2005] and those possibly triggered by an external kink oscillation [Foullon et al., 2005]. Confident discrimination between the flaring oscillations caused by global sausage modes and by oscillatory regimes of magnetic reconnection is impossible until the theory of the latter is understood.

Chapter 5

Observations of QPP in flares without spatial resolution

5.1 Introduction

Advances in solar imaging and spectroscopy - in particular the launch of satellites like RHESSI (2002) and Hinode (2006) - have made concrete analysis of solar oscillations, such as those described in Chapter 4, a more realistic possibility. However, even in the solar corona spatial information is not always available, and in the stellar context this information is absent in all cases. In view of this, we address the question of what progress can be made in the study of QPP events in the absence of such seemingly crucial information. As has already been discussed in Chapter 4, a further source of information includes the multi-wavelength approach, where QPP is observed in different bands simultaneously [Melnikov et al., 2005; Inglis et al., 2008]. Microwave or X-ray spectral resolution [Fleishman et al., 2008] is also potentially useful, but is not always available.

In addition, the detection of several periodicities in the same signal can provide us with valuable knowledge (see Chapter 3). Different periodicities can either be associated with different MHD modes of the emitting plasma structure, or with different temporal

harmonics of the same nonlinear oscillation. In both cases, the ratios of different periods can be used to reveal the physical mechanism responsible for the pulsations and hence become a tool for diagnostics [Andries et al., 2005]. There have been several studies revealing the simultaneous presence of several periodicities in flaring light curves. For example, Stepanov et al. [2004] found 2.4 s, 7 s, and 14 s oscillations in the flare observed on 1999 August 28 using the Nobeyama Radioheliograph (NoRH); Melnikov et al. [2005] detected periodicities of 8-11 s and 14-17 s in the flare on 2000 January 12 observed with NoRH and Yohkoh/HXT, and the study of Mészárosová et al. [2006] revealed the presence of multiple periodicities in the range from one to five minutes in the flares observed on 2000 July 14, 2001 April 12, and 2001 April 15 in radio (0.8-4.5 GHz) and X-ray bands using the Ondrejov radiospectrograph and Yohkoh/HXT. The traditional technique for the detection of multiple periodicities is the search for significant peaks in the Fourier time spectrum. However, it is non-trivial to estimate the confidence level of the detection when there are multiple peaks in the spectrum, as the techniques for the estimation of the confidence level give the result applicable to the highest spectral peak only (see the discussion in Horne and Baliunas [1986]). To the best of our knowledge, there have not been attempts to use multi-periodic information as a tool for determining the mechanism responsible for flaring QPP.

In this chapter we seek to illustrate that, even in the absence of spatial resolution, concrete conclusions about flaring QPP may be drawn by taking advantage of the presence of multiple significant periods. We analyse a flaring QPP event from 3rd July 2002 which contains several periodicities, estimate the significance of different peaks in time spectra, determine the period ratios, and also demonstrate that ratios of different periods can contribute to the determination of the physical mechanism responsible for the periodic behaviour. The text is organised as follows: in Section 5.3 the lightcurves of the flaring event are presented at multiple wavelengths and the fundamental nature of the flare is described. Section 5.4 details the time series analysis illustrating the multi-periodic nature of the event. In Section 5.5 we concentrate on the available

imaging information for this event, using data from RHESSI, SOHO and the Nobeyama Radioheliograph. Finally, in Section 5.6 we discuss our findings in terms of the underlying mechanisms that may be responsible for the observed QPP.

5.2 The wavelet transform

At this juncture we briefly introduce the wavelet transform. Wavelets are a popular tool for the analysis of time series data [Weng and Lau, 1994; Lau and Weng, 1995; Torrence and Compo, 1998]. The main advantage of the technique is that it provides local information, rather than the global results returned by classical techniques such as the Fourier transform and the Scargle periodogram. A comprehensive description of wavelets may be found in Torrence and Compo [1998], thus we will discuss only the key points here. The basic procedure is to select a 'master' function which must be of zero mean and localised in both time and frequency, and to mesure the correlation of this function with the time series of interest as a function of t. For oscillatory process, the most commonly used master function is known as the Morlet wavelet and is described by

$$\psi_0(\eta) = \pi^{-1/4} \exp^{i\omega_0\eta} \exp^{-\eta^2/2} . \tag{5.1}$$

Here η is a time parameter, and ω_0 is the nondimensional frequency associated with it. This function is equivalent to a sine wave multiplied by a gaussian, thus it represents a localised wavetrain, an ideal function for studying suspected oscillatory processes. The wavelet transform is then given by

$$W_n(S) = \sum_{n'=0}^{N-1} x'_n \psi^* \left[\frac{(n'-n)\delta t}{s} \right] , \tag{5.2}$$

where N is the number of points in the time series x, and s is the wavelet scale. This expression is the convolution of the time series x with a translated version of the wavelet function $\psi_0(\eta)$. The reason for the popularity of this technique is that the

amplitude and frequency of signal components can be measured as a function of time. Later in this chapter, and in Chapter 6, we will utilise this method to our advantage.

5.3 Analysis of integrated light curves

The flare analysed here was a GOES X1.5 class event. It occurred on 3rd July 2002 at 02:10 UT and was observed by the Reuven Ramaty High Energy Solar Spectroscopic Imager (RHESSI) and the Solar and Heliospheric Observatory (SOHO) satellites. It was also observed by the ground-based Nobeyama Radioheliograph and Radiopolarimeter in Japan, but was missed by the TRACE satellite. According to the lightcurves in X-ray and radio wavelengths, the flare consisted of two distinct phases; a sharp initial energy release, followed shortly afterwards by a suspected oscillatory phase between 02:11 and 02:13 UT. The period analysis presented here is concerned entirely with this second phase. This event is interesting in the context of this study as its time spectrum contains several pronounced peaks which are possibly connected with multi-periodic oscillations. Also, it was observed with good time resolution by three different instruments, which minimises possible instrumental artifacts.

The total flux time profiles of the radio emission from the entire event region, at the dual frequencies of 17 GHz and 34 GHz used by the Nobeyama Radioheliograph, are shown in Figure 5.1. The time cadence of the signal is 1 s.

The flux at 17 GHz is stronger than that at 34 GHz, a typical observation for solar flares. The time profiles clearly illustrate a strong impulsive emission spike at approximately 02:10 UT. The emission drops off rapidly before rising again at 02:11 UT in what we will consider to be the second phase of the flaring event. The flux time profiles (light curves) during this second phase are suggestive of the presence of quasi-periodic pulsations. Similar quasi-periodic features are seen in the lightcurves obtained with the Nobeyama Radiopolarimeters at 9 GHz, 17 GHz and 35 GHz.

The emission time profiles for this event registered by RHESSI in different energy channels are shown in Figure 5.2. Here the time resolution is 4.2 s, coinciding with the

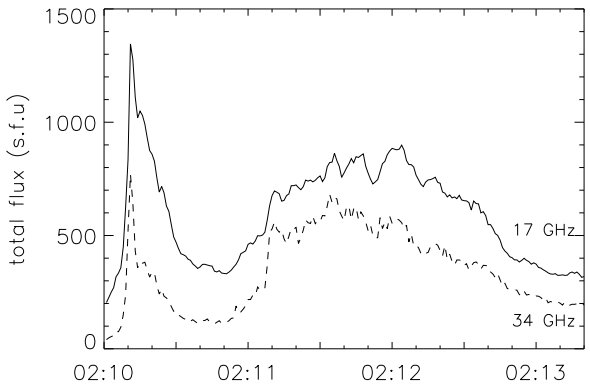

Figure 5.1: Time profiles of the emission from the solar flare of 3rd July 2002, as observed by the Nobeyama Radioheliograph at 17 GHz and 34 GHz. The first emission spike is seen just after 02:10 UT, followed by an oscillatory phase between 02:11 and 02:13 UT.

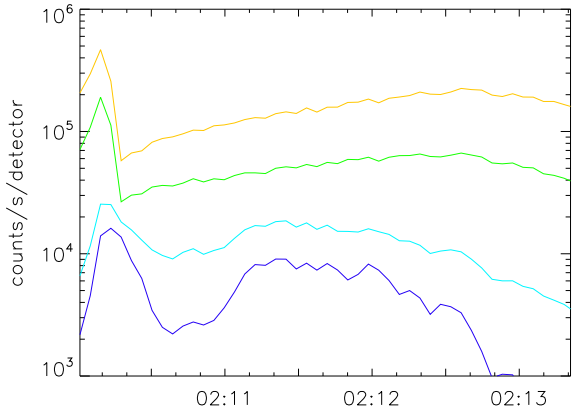

Figure 5.2: Time profiles of X-ray emission from the solar flare of 2002 July 3, observed by the photometric detectors on board RHESSI. Yellow (top): 6-12 keV emission, green: 12-20 keV emission, light blue: 20-40 keV emission, dark blue (bottom): 40-60 keV emission. To avoid overlapping the light curves have been scaled by arbitrary factors.

spinning period of the RHESSI spacecraft. The flux levels shown in Figure 5.2 have been arbitrarily scaled to avoid overlap and preserve the clarity of the temporal behaviour. The comparison of microwave and X-ray fluxes shows that the same behavioural trend is exhibited by both the microwave and X-ray time profiles, i.e. an initial spike followed by a second event phase. This is significant as X-rays and microwaves are generated by different mechanisms, and implies that some additional common physics is present. In the X-ray data, there is also an attenuator state change at the flare onset, visible as a jump in X-ray counts at approximately 02:10:10. This is the result of an automated process whereby shutters are activated in front of the RHESSI detectors to reduce count rates. This avoids problems associated with high detector dead-time and limited spacecraft memory (see the discussion of RHESSI in Chapter 1).

The phase relationship between oscillatory signals observed with different instruments is important for understanding the underlying physics behind a QPP event. Hence, we begin with consideration of the correlation between the light curves observed in microwave and X-ray bands by calculating the correlation coefficients between signals. First, we utilise a high pass filter with a frequency cutoff of 0.03 Hz to remove the background trend of the flaring lightcurve. Subsequent analysis of the time series data showed a strongly in-phase relationship between 17 GHz microwave data and the RHESSI counts at 20-40 keV and 40-60 keV. The highest value of the correlation coefficient was 0.83 between the 17 GHz signal and RHESSI counts at 40-60 keV, and corresponded to zero lag between the signals. Similarly, at 20-40 keV the correlation value with the microwave signal was 0.67, again corresponding to zero time lag. The same analysis showed that the RHESSI counts in the 12-20 keV band and the 17 GHz microwave data were largely uncorrelated. This is not surprising since the X-ray counts in this energy range are generally thermal in origin, while the signals in the other analysed bands are associated with nonthermal emission. Since different physical mechanisms are responsible for the generation of pulsations in thermal X-rays, non-thermal X-rays and microwaves, it does not follow that pulsations in microwaves would necessarily be

reproduced in the thermal X-ray regime.

In order to investigate whether oscillations are occurring in this event, the time profiles must be carefully analysed. One of the most robust and commonly used techniques for this is the Lomb-Scargle periodogram method introduced in Chapter 4 [Scargle, 1982], which also provides estimates for the confidence level of spectral peaks as defined by Horne and Baliunas [1986]. In the context of solar flares, because of their short duration and evolutionary nature it is necessary to prepare the signal prior to utilising the periodogram. Spectral filtering is used to remove the lowest frequencies in the Fourier spectrum, corresponding to the long term evolutionary trend of the flaring emission. The Lomb-Scargle periodogram is then performed on the remaining signal. It is important however that only the minimum necessary level of filtering is applied, and as much as possible of the original signal is preserved.

The Lomb-Scargle periodogram method was applied to the data obtained by the Nobeyama Radioheliograph during the second phase of the flare, between 02:11 and 02:13. The resulting periodogram is shown in Figure 5.3.

A period of approximately 28 s is revealed with greater than 99% confidence in both the 17 GHz and 34 GHz channels. There are also other spectral peaks that may be significant, but require careful analysis. According to Horne and Baliunas [1986] the significance levels of secondary peaks in a Lomb-Scargle periodogram are not accurately defined, since spectral leakage from the primary peak effects the remainder of the spectrum. In order to examine the significance of secondary peaks, this effect must be accounted for.

This technique can also be applied to RHESSI time series data. The RHESSI satellite rotates on its axis with a period of approximately 4 s, an action essential to its imaging process. This artificial period could have a significant impact on any frequency analysis technique. The simplest solution is to utilise the X-ray data with time bins of 4 s, thus eliminating the rotation period from the data. However, for short events such as this flare the resulting frequency resolution is poor. If a greater number of datapoints

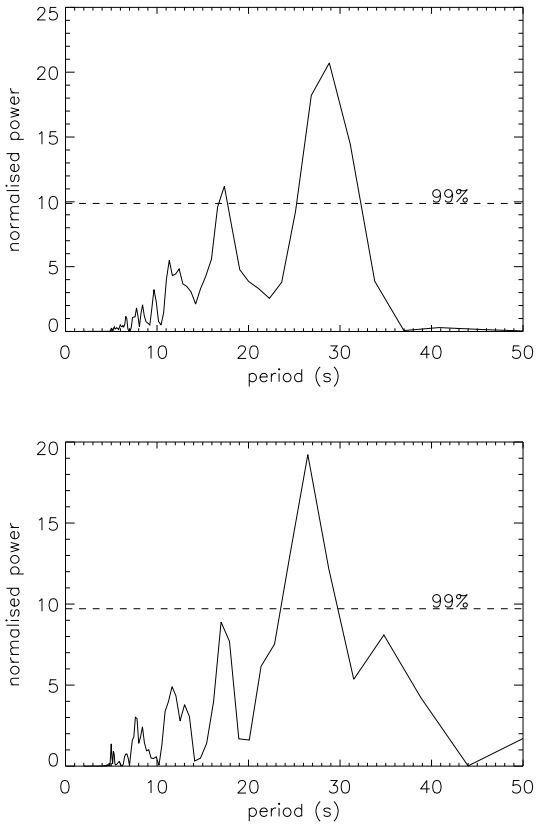

Figure 5.3: Lomb-Scargle periodogram of the 17 GHz (top) and 34 GHz (bottom) signals from the Nobeyama Radioheliograph during the second flaring phase. The periodogram reveals a dominant period of 28 s at 17 GHz, well above the 99% confidence level defined by Horne and Baliunas [1986]. This period is also present in the 34 GHz data above 99%.

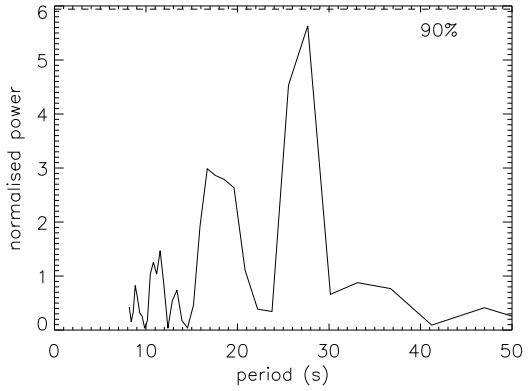

Figure 5.4: Lomb-Scargle periodograms of RHESSI time series data in the 40-60 keV range using 4.2s time bins. The dominant peaks are broadly consistent with those observed in Nobeyama Radioheliograph data.

are required it is possible to employ shorter time bins. In this case the artificial period can be removed by spectrally filtering all periods of 4 s or less from the data.

The periodogram of RHESSI counts between 02:11 and 02:13 in the 6-12keV and 40-60 keV X-ray ranges is illustrated in Figure 5.4 for this event using time bins of 4.2s.

The Lomb-Scargle periodograms of the RHESSI data shows a peak near the 90% confidence level at roughly the same location as the primary Nobeyama Radioheliograph peak. In fact, the shape of the hard X-ray fourier spectrum is very similar to that obtained from the radio data. However, for the 17 GHz and 34 GHz spectra the peaks are substantially above the 99% confidence level. The lower amplitude RHESSI spectral peaks can be attributed to the reduced number of data points available for sampling and to the fact that different mechanisms operate in the microwave and X-ray regimes. Nevertheless, this correlation between independent instruments at different energies is significant and should be explored.

5.4 Analysis of multiple periods

The presence of multiple significant peaks in a QPP event can shed light on the physical mechanism responsible for QPP. In both the Nobeyama and RHESSI periodograms shown in Figures 5.3 and 5.4 there is a suggestion of more than one significant peak. Periodogram analysis is notoriously noisy [Scargle, 1982], and the presence of multiple peaks must be analysed with care, as they may be artificial in origin. For example, spurious strong peaks may be generated due to sidelobes and spectral leakage from a genuine strong peak. Misapplication of spectral filtering may also cause peaks to be artificially enhanced.

Fortunately, the nature of secondary periodogram peaks may be tested. The technique is based on selective use of spectral filtering, whereby the principal peak is filtered out down to the background noise level. The periodogram is then recalculated on the remaining signal. Using this method one would expect genuine periods to increase or remain steady in spectral power, while artificial peaks would be reduced in power. This is because a strong primary peak can cause spectral leakage to other frequencies.

An advantage to using the Lomb-Scargle periodogram technique is that there is a robust and well-understood procedure for the estimation of the statistical significance of each spectral peak. As pointed out in Horne and Baliunas [1986], the confidence levels in the Lomb-Scargle periodogram are only strictly valid for the most powerful peak in the spectrum. When this primary peak is carefully removed from the signal, the recalculated periodogram confidence levels are defined as the probability of a real signal being present at the secondary frequency, given that a signal already exists at the primary frequency. We achieve this signal removal by transforming the time signal into frequency space, and suppressing the frequencies corresponding to the most powerful peak detected by the Scargle periodogram. These frequency values are replaced by background noise values and the signal is transformed back into time space. The periodogram is then performed on this modified signal. Here the power corresponding to a certain confidence level will remain the same however the heights of the spectral peaks in this iterated periodogram

will be different.

This process can be iterated if there are multiple significant secondary peaks. The peaks are simply filtered in order of significance until no more peaks remain above the specified confidence level. The method is purely statistical however, and the onus is on the researcher to interpret the results and account for systematic effects. For example, in Muglach and Balthasar [2005] it was noted that confident artificial oscillations in TRACE data were observed as a result of the satellite's image compression algorithms.

With these provisos in mind, this analysis method was applied to 17 GHz Nobeyama Radioheliograph data and Nobeyama Radiopolarimeter data at 9 GHz, 17 GHz and 35 GHz. The results of the iterative spectral filtering are shown in Figure 5.5. The top panel of each column shows the original periodogram, while the subsequent panels show the effects of filtering the primary peak and recalculating the periodogram. The iteration process reveals the same three significant periods at multiple frequencies for two separate instruments; $P_1 = 28 \pm 2$ s, $P_2 = 18 \pm 1$ s and $P_3 = 12 \pm 1$ s. Here the error has been estimated using the peak half-widths shown in Figure 5.5. We have averaged the individual measurements from each frequency band to arrive at the combined values we have stated. The implication is that these peaks are real, rather than a result of spectral leakage.

To corroborate this result, the same technique was applied to the RHESSI hard X-ray light curves. The original periodograms of the RHESSI data did not reveal any periods significant to the 99% confidence level. However, as a further test we re-bin the RHESSI time series into 2 s intervals to improve the resolution. To compensate for potential spacecraft rotation effects all periods of 5 s or less are then spectrally filtered from the data. Figure 5.6 shows the resulting iterations of the hard X-ray periodograms in the 40-60 keV range. The dashed line in the top panel corresponds to the original periodogram obtained using 4.2s time bins. From this the presence of both the 28 s and 18 s periodicities are revealed in hard X-rays. The 12 s period seen in the radio data is not detected at a statistically significant level in the RHESSI light curve.

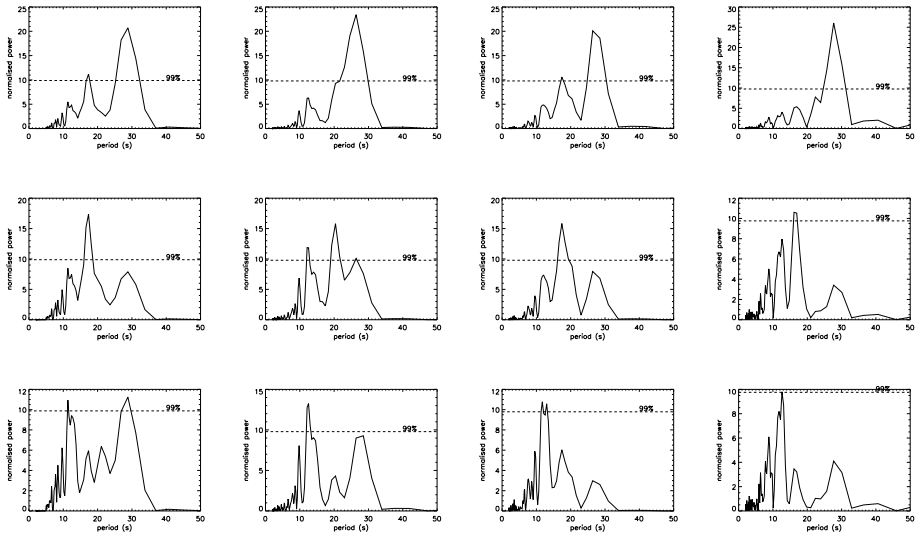

Figure 5.5: Lomb-Scargle periodograms showing the effects of iterative peak suppression at different frequencies. Columns from left to right: Nobeyama Radioheliograph data at 17 GHz and Nobeyama Radiopolarimeter data at 9 GHz, 17 GHz, 35 GHz. In all cases the same three peaks are found above the 99% confidence level.

The fact that the peaks illustrated here coincide in period with those detected using the original 4.2s time bins brings confidence to the result. That they also coincide with the periods obtained via two other separate instruments is a further indication that the RHESSI spectra are not compromised by instrumental artifacts.

Having established the presence of several significant periods, another point of interest is whether these multiple harmonics co-exist in the same time range. The possibility that an oscillation period evolves over time - thus giving the impression of multiple harmonics - must be considered. To test this, Morlet wavelet analysis was employed [Torrence and Compo, 1998]. Unlike the Scargle periodogram, the wavelet technique allows for analysis of dominant periods in a data set as a function of time.

The top panel of Figure 5.7 shows the Morlet wavelet of the 17 GHz Nobeyama Radioheliograph signal after background subtraction. The short duration of this event dictates that the overall resolution of the wavelet in both period and time is poor. Although significant periods are present (in particular 28 s and 18 s), it is also unclear from this plot whether the multiple harmonics are indeed co-temporal.

To study the time localisation of the three detected significant periodicities in more detail, we filtered out signals in the frequency bands determined by the periodogram analysis (namely 0.03 - 0,04 Hz, 0.045 - 0.065 Hz and 0.08 - 0.11 Hz). It is worth emphasising that we have assumed - based on the periodogram analysis - that these periods are significant for the purpose of clarifying their temporal nature. The three narrowband signals were separately synthesised, normalised to their maximum amplitudes, and then summed up into a combined new signal. This approach allows us to amplify the signals of the second and third spectral peaks, making them more pronounced in the wavelet spectrum. Clearly, this method does not spoil the spectral information only if there is no frequency shift across the boundaries of applied spectral filters, which is consistent with the wavelet spectrum shown in the top panel of Figure 5.7. The wavelet spectrum of the combined time signal is shown in the bottom panel of Figure 5.7. The three significant periodicities detected in the periodogram are seen to occur with a significant

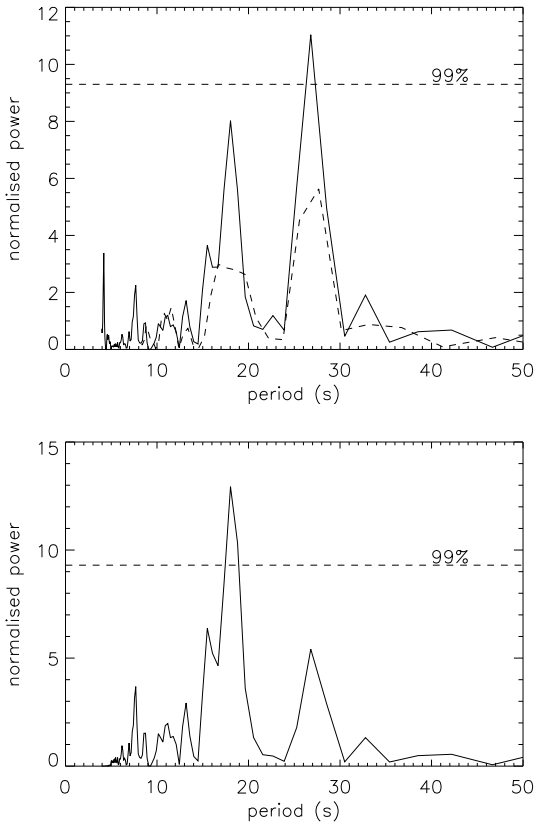

Figure 5.6: Iterated Lomb-Scargle periodograms of RHESSI time series data between 40-60 keV using 2 s bins. Top panel: original periodogram, showing the dominant 28 s period at 99% confidence. The original 4.2s periodogram is shown as a dashed line for comparison. Bottom panel: Periodogram after suppression of the 28 s peak. The 18 s period is now resolved above the 99% confidence level.

overlap in time. Thus we consider the possibility of a single, rapidly evolving oscillation less likely.

5.5 Imaging

As was shown in Chapter 4, information useful for the interpretation of the observed QPP could in principle be obtained from imaging observations. The Nobeyama Radioheliograph and the RHESSI satellite are both equipped with imaging capabilities that allow this solar event to be clearly resolved at various energies. In the case of the RHESSI satellite, collimating optics is used in order to reconstruct images of high energy emission, with a maximum resolution of approximately 2.5". The Nobeyama Radioheliograph is also capable of generating images, with a more modest maximum resolution of 5" at 34 GHz (10" at 17 GHz).

SOHO MDI images prior to the flaring event show the active region from which this flare originated. The image in Figure 5.8 is taken around two hours before the onset of the flare. Based on this and Figure 5.9, it appears that the primary emission source at both radio and X-ray wavelengths is centred between two sunspots.

Figure 5.9 contains a SOHO EIT image of this event with RHESSI overlays at thermal and non-thermal energies. The implication is that this was a consistently compact structure, with only a single clear emission source resolved. The 6-12 keV thermal emission is broadly consistent with the EIT 195 Å structure, bearing in mind that different temperatures are observed and that the EIT image is necessarily taken before the onset of flaring activity because of image saturation during the flare itself. The 40 - 60 keV emission is non-thermal in origin, but appears to originate from the same source as the thermal component. In general, hard X-ray sources are expected at flaring loop footpoints and at the loop apex [Krucker and Lin, 2008], or occasionally above the loop apex [Masuda et al., 1994], while thermal X-rays (such as the 6-12 keV range) are sourced from the body of the flaring loop. In this case it appears that any flare structure is too compact to be reliably resolved.

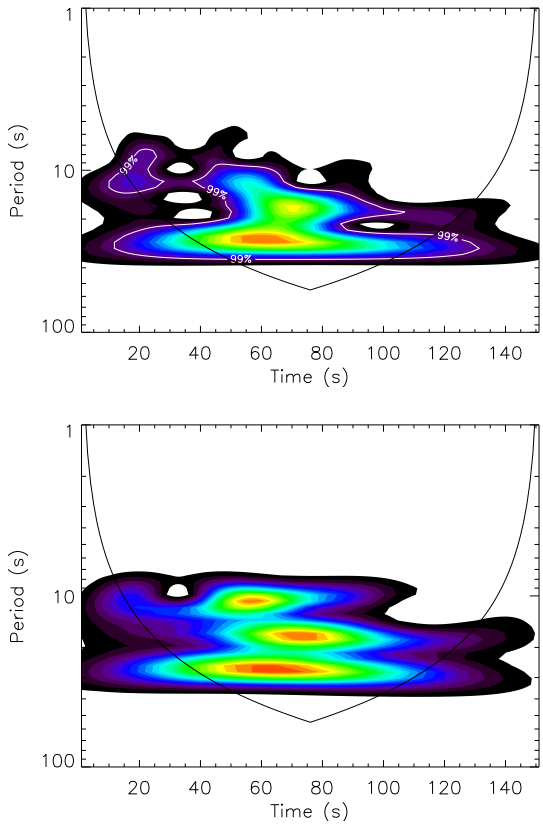

Figure 5.7: Top: Morlet wavelet of the 17 GHz Nobeyama Radioheliograph signal after background subtraction. Bottom: A combined plot showing the result of taking wavelets in three frequency bands, corresponding to 0.03 - 0.04 Hz, 0.045 - 0.065 Hz, and 0.08 - 0.11 Hz. The start time is 02:10:50.

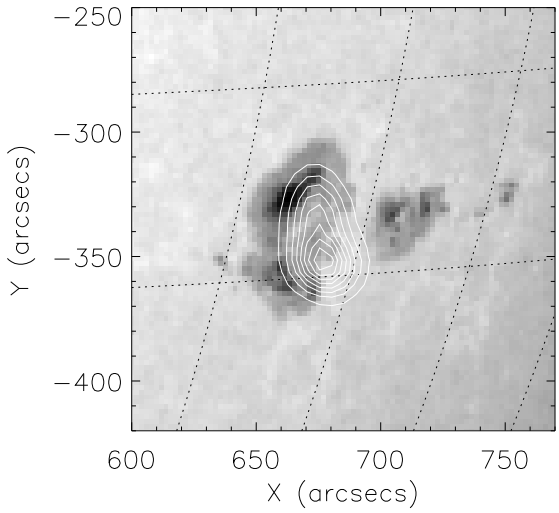

Figure 5.8: SOHO MDI image of the active region from which the solar flare originated. This MDI image was taken at 23:59:00 on 2002 July 2. Overlay: Microwave emission at 17 GHz during the flare, observed by the Nobeyama Radioheliograph.

Microwave images from the Nobeyama Radioheliograph are also centred on this region. The main emission source at 34 GHz is located at (680, -360) arcseconds, cospatial with the X-ray sources. Prior to the flare onset there is a second microwave source resolved at (670, -330) arcseconds. This quiet region is dominated by the southern source during the flare itself. At 17 GHz, only a single source is visible, most likely due to limited spatial resolution.

In Chapter 4 (see also Inglis et al. [2008]) we demonstrated the use of a cross-correlation mapping technique in an oscillatory solar flare from 8th May 1998. This method illustrates the cross-correlation values of the oscillatory signal component over different parts of the loop. It is also capable of revealing the phase relationship between different loop segments. Unfortunately, for the event of 3rd July 2002 use of this method was compromised by instrumental effects, due to the excessive strength of the signal. The Nobeyama Radioheliograph data is affected by jitter because of the high levels of flux from this flare. At peak flux levels the Radioheliograph is unable to properly resolve

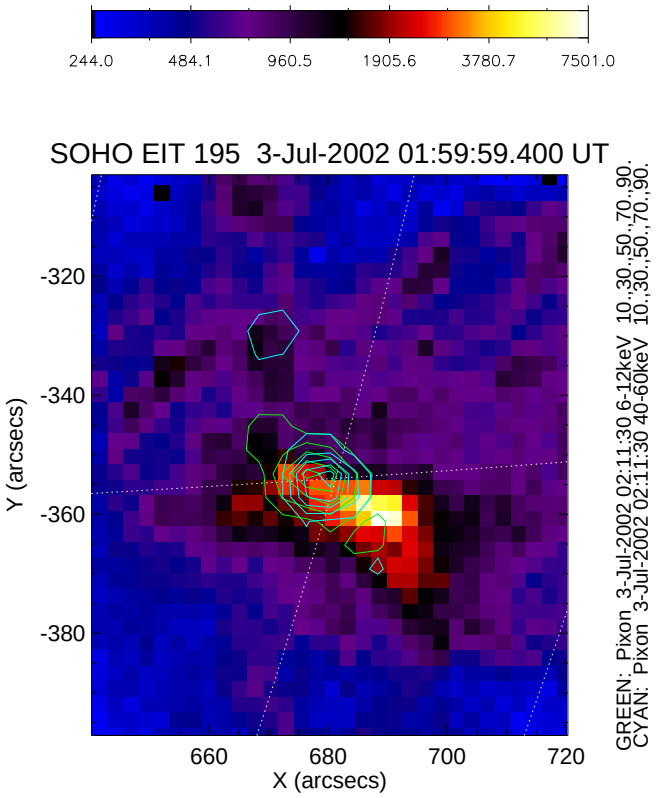

Figure 5.9: SOHO EIT image of the flare region just prior to the onset of the flare. The overlays are RHESSI pixon reconstructions of x-ray emission during the oscillatory phase of the flare in the 6 - 12 kev (green contours) and 40 - 60 kev (cyan contours) bands.

the solar disk, resulting in a loss of pointing accuracy. The spatial artifacts arising from this cannot be easily overcome. The pointing system of the RHESSI satellite proved more robust than that of the Nobeyama Radioheliograph in this case. However, for the hard X-ray sources, no evidence of an extended spatial structure was found using cross-correlation analysis. As with its predecessor Yohkoh, RHESSI imaging relies on collimating optics and complex image reconstruction algorithms which may limit the applicability of the cross-correlation mapping technique. It is also possible that the emitting region is simply too small to be reliably mapped.

5.6 Discussion

In this chapter we analysed a multi-periodic flaring event and estimated the significance of different spectral peaks in the time spectra. Pulsations were observed during the second phase of the analysed flaring event in microwaves and in a range of hard X-ray bands. Although initial study indicated only a single period, careful analysis revealed that three distinct periods were significant above 99% confidence in the microwave data, obtained with NoRH and NoRP: $P_1 \approx 28 \pm 2$ s, $P_2 \approx 18 \pm 1$ s and $P_3 \approx 12 \pm 1$ s. The 28 s and 18 s oscillations were also detected in the RHESSI lightcurves in the 40-60 keV energy range. The 12 s period was not detected in the X-ray flux. We postulate that this is due primarily to the reduced temporal resolution of the X-ray data, a consequence of our desire to avoid complications introduced by RHESSI spacecraft rotation.

The presence of multiple significant periods in solar flare pulsations is a significant finding and poses interesting questions about the theoretical mechanisms that may be responsible. The fact that microwaves and hard X-rays share the same oscillatory behaviour is also important; microwave emission is generated mostly through the gyrosynchrotron mechanism, while hard X-rays usually arise via non-thermal bremsstrahlung and particle interactions at the photosphere. The presence of multiple periods in light curves obtained via different instruments also ensures that the periods are not instrumental, atmospheric or magnetospheric artifacts.

Spatially resolved analysis of the flaring oscillation was not possible on this occasion, due to instrumental problems. However, event images show that the spatial extent of this flaring structure is very limited in any case.

Due to the lack of information about the spatial structure of the oscillation, the interpretation of the observed oscillation should be based upon the analysis of the ratios between different periods, $P_2/P_1 \approx 0.64 \pm 0.07$ and $P_3/P_1 \approx 0.43 \pm 0.06$. If the multiple periodicity is caused by temporal harmonics of a nonlinear oscillation, because of the nonlinear doubling of frequency the resultant spectrum should be equidistant, i.e. the frequencies corresponding to different peaks are divisible by integer. This corresponds to the ratios of periods $P_N/P_1 = 1/N$, where N is an integer representing the harmonic number. The ratios of the lowest harmonics are $P_2/P_1 \approx 0.5$ and $P_3/P_1 \approx 0.33$. Such a spectrum would be a characteristic feature of an anharmonic oscillation, for example the periodic generation of plasmoids by magnetic reconnection [Kliem et al., 2000]. However, we can see that the observed P_2/P_1 ratio is not exactly consistent with the $1/N$ pattern. A certain discrepancy could be attributed to the error in determinating the spectral peak position, however the error of about 30% is perhaps a bit too large. Thus, the interpretation of the observed periodicities in terms of a oscillatory regime of magnetic reconnection does not seem to be consistent with our findings. Another option could be the presence during magnetic reconnection of several simultaneous but independent oscillatory processes. However, we are not aware of any theoretical or numerical predictions of such an effect. Hence, although we certainly cannot exclude this interpretation of the observed event, we consider it to be a less likely explanation.

Similar P_N/P_1 ratios appear if the frequencies are connected with different spatial harmonics of a resonator, e.g. a coronal loop. However, in this case the ratios deviate from the $1/N$ pattern because of dispersion, as waves with different wave numbers have different phase speeds, and the ratio becomes $P_N/P_1 = (V_1/V_N)/N$, where V_1 and V_N are the phase speeds of the global mode and the N-th harmonics, respectively. We exclude the longitudinal and torsional modes of a magnetic flux tube from considera-

tion as they are not able to produce the observed modulations of the microwave and hard X-ray emission simultaneously [Nakariakov, 2007]. Two other modes, sausage and kink, are able to produce the observed modulation: the sausage mode by the Zaitsev - Stepanov mechanism [Zaitsev and Stepanov, 1982], and the kink mode by the periodic triggering of reconnection [Nakariakov et al., 2006]. Both sausage and kink modes of a plasma cylinder are known to be dispersive [Edwin and Roberts, 1983]. For both sausage and kink modes, the phase speed monotonically decreases with the decrease in the wavelength, making the P_N/P_1 ratio greater than $1/N$ (for a more detailed analysis of this ratio for the sausage mode, see Chapter 3, and see also the dispersion diagram shown in Figure 2.2). Phrased differently, this means that NP_N/P_1 should always be greater than 1, but also that as N increases, this deviation from unity should become less pronounced. Taking the values of the period ratios determined in this chapter, we obtain that $2P_2/P_1 \approx 1.13 - 1.46$ and $3P_3/P_1 \approx 1.1 - 1.5$ which gives the monotonic decrease in the phase speed within the error bar, consistent with the theory.

Thus, both sausage and kink modes could produce the observed time spectrum. On the other hand, the observed lack of correlation between the light curves of thermal and nonthermal emission indicates that the observed periodic modulations are not likely to be produced by the sausage mode. Indeed, the sausage mode is an essentially compressible perturbation, and hence it should produce the modulation of thermal emission. The thermal emission produced by sausage waves is associated with the variation of plasma density caused by the oscillation of the magnetic field (through the frozen-in condition), and is then different from the change in the plasma density caused by field aligned flows of matter, e.g. chromospheric evaporation. Consequently, the variations of thermal emission induced by the sausage mode should be superimposed with the variations of the thermal emission, caused by evaporation. In our study this was not found. It is also not clear how the Zaitsev-Stepanov mechanism would work for multiple spatial harmonics of the sausage mode. However, based on the available data a viable possibility is that the observed QPP be interpreted as a multi-modal kink oscillation of

an external coronal structure, which periodically triggers magnetic reconnection in the flare. The period ratios we have measured are consistent with previous numerical studies of the period ratio for the kink mode, for example Andries et al. [2005] and McEwan et al. [2008]. Thus, the observed period ratios coupled with the lack of thermal QPP make this, in our view, the most probable explanation.

In this chapter we made an attempt to identify the mechanism responsible for QPP generation without the benefit of spatial resolution. Our analysis was based upon the assessment of the ratios of different periodicities found in the event light curves. This approach is necessary in cases where the spatial information is unavailable. As the same periodicities were detected in the data obtained with different instruments and in different bands, we claim confidently that these periodicities have natural origins in the solar corona. A similar approach can be applied to the interpretation of QPP in stellar flares (see for example Mathioudakis et al. [2003], Zaitsev et al. [2004] for recent findings), in which imaging information is intrinsically unavailable.

Chapter 6

Empirical mode decomposition as a tool for coronal wave studies

6.1 Introduction

Various established techniques already exist for analysing the time series of impulsive flaring events. Some of the most popular of these are the Scargle periodogram [Lomb, 1976; Scargle, 1982; Horne and Baliunas, 1986], the wavelet [Torrence and Compo, 1998], and the classical Fourier transform. Many of these have been utilised in the preceeding observational chapters and we have demonstrated that, properly used, these techniques can produce powerful results. However they are all also subject to certain limitations. The periodogram and Fourier transform are designed to operate on data which is assumed both stationary and linear, whereas flaring time series generally produce lightcurves which are both nonlinear and non-stationary.

In order to be considered stationary, a signal $X(t)$ must satisfy the condition

$$C(X(t_1), X(t_2)) = C(X(t_1 + \tau), X(t_2 + \tau)), \tag{6.1}$$

for all t, where C is the covariance function and τ is a time interval. In other words, the signal $X(t)$ must be strictly periodic. For realistic data signals this condition

is never truly satisfied. The Fourier transform is also particularly affected by nonlinearity since it is based on trigonometric functions. As a result, extra harmonics are introduced to the Fourier spectrum in order to attempt to describe signals which include deformed sine and cosine waves. Another critical issue is the necessity of subtracting a background function. Since flares are usually short, impulsive events, any oscillations are inevitably accompanied by a long-term evolution of the flaring flux. Untreated, this trend causes the Fourier spectrum of the flare to be dominated by the lowest available frequencies. As such, accounting for this trend is a necessity for any period analysis, and consequently a source of error is introduced at an early stage. A technique that does not require such human intervention at the pre-processing stage would be highly advantageous.

A main advantage of the wavelet transform over the Fourier transform is that it is able to deal with nonstationary signals. This makes it a useful tool for analysing gradual frequency modulation, although the resolution is still limited by the width of the basic wavelet function (for oscillatory processes this is usually a sine wave multiplied by a gaussian, known as the Morlet wavelet). Additionally, the short nature of most flaring events usually ensures that both the Scargle periodogram and the Morlet wavelet suffer from poor overall frequency resolution. This problem continues to undermine attempts to gain quantitative results via coronal seismology. For the Morlet wavelet frequency resolution can sometimes be improved at the expense of the time resolution of the wavelet, but a method which grants excellent resolution in both time and frequency remains an elusive but desirable goal.

In this chapter we explore the application of a new technique in the context of the solar corona, empirical mode decomposition [Huang et al., 1998] and the associated Hilbert spectrum, which together promise to negate these issues. Although a relatively new method, it has been successfully employed in geophysics and other fields. Here we explore the possible applications of EMD to pulsations in solar flares and compare with established techniques such as the wavelet.

6.2 Empirical mode decomposition and the Hilbert spectrum

The technique of empirical mode decomposition (EMD), designed for the analysis of nonlinear and nonstationary signals, was thoroughly described by Huang et al. [1998]. Thus we will limit ourselves to the key points here. The essence of the technique is to represent a real input signal - such as a flaring lightcurve - as a series of intrinsic mode functions (IMFs). These IMFs must possess certain characteristics. Firstly, they must contain the same number of maximal and minimal extrema, or at most a difference of 1 in number. The same rule applies to the number of zero crossings in either direction. Thirdly, at any point in the function, the mean of the envelopes defined by the local maxima and the local minima must be zero. This means that, in the IMF, maxima cannot be negative nor minima positive. In general, a real signal is decomposed into a number of such functions, accompanied by a final component which represents a long-term trend. The first step in the decomposition process is to estimate the shortest timescale of interest in the original data. This is done by measuring the time lapse between sucessive extrema. The upper and lower envelopes are then defined by connecting all maximal extrema via a cubic spline, and similarly all minimal extrema. From this the local mean m is defined. To extract the first component, the local mean is subtracted from the original data $X(t)$, i.e.

$$h_1 = X(t) - m. \tag{6.2}$$

The function h_1 is not yet guaranteed to be an IMF. Therefore, this process is repeated where h_1 is treated as the new 'data', a process called *sifting*. The data is sifted iteratively until the first IMF is obtained. This IMF is therefore the local mode with the shortest characteristic period that exists in the data. To continue the process the IMF is subtracted from the original time series $X(t)$. The result is known as the *residue*. To continue searching for IMFs, this residue is treated as the data, and the

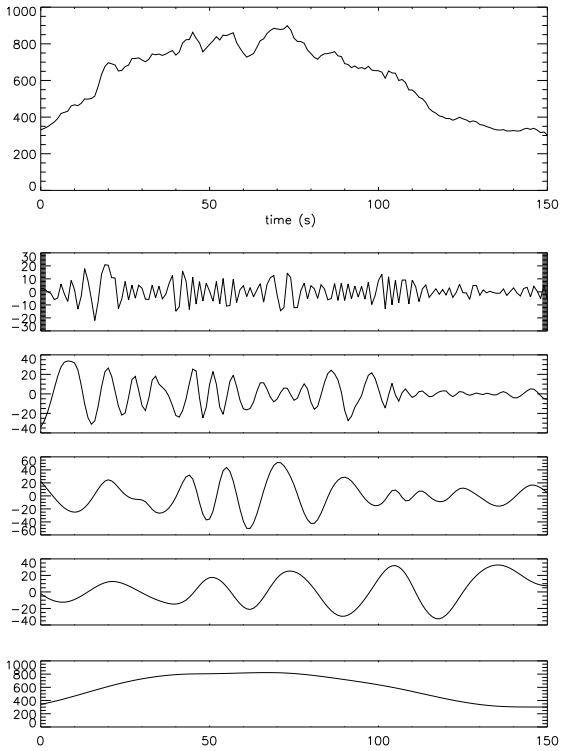

Figure 6.1: Result of empirical mode decomposition as applied to the solar flare of 3rd July 2002. The start time is 02:11 UT. The top panel shows the original flare signal in the microwave regime at 17 GHz, obtained from the Nobeyama Radioheliograph. The following four panels are IMFs derived from the decomposition process. The final panel represents a long-term trend.

process described above is repeated until no more IMFs can be extracted. The final result is a number of signal components which are IMFs and a final component which is residue. An example of this decomposition process is shown in Figure 6.1.

Huang et al. [1998] proposed that the period analysis of the IMF signal be carried out using the Hilbert spectrum. This spectrum is defined as:

$$H(t) = \frac{P}{\pi} \int \frac{X(t)}{t - t'} dt', \tag{6.3}$$

for a time series $X(t)$, where P is the Cauchy principal value. This spectrum

is essentially a convolution of $X(t)$ with $1/t$, thus it emphasises the local properties of $X(t)$. An analytic signal can then be written as follows:

$$Z(t) = X(t) + iH(t), \tag{6.4}$$

and

$$\theta = \arctan\left(\frac{H(t)}{X(t)}\right), \tag{6.5}$$

where θ is the phase of the complex signal $Z(t)$. Given this, the instantaneous frequency can subsequently be defined as:

$$\omega = \frac{d\theta}{dt}. \tag{6.6}$$

This definition of frequency is counter-intuitive. According to Equation 6.6, the instantaneous frequency is calculated as the derivative of the phase difference between the signals $X(t)$ and $H(t)$. Conventional logic dictates that at least one full wave is required to define the frequency of a signal, but according to the definition in the Hilbert spectrum this is not the case. The result is that the frequency can be calculated at every point in the signal, simply by computing the derivative of the phase. Hence the output Hilbert spectrum contains extremely high resolution in both frequency and time.

Although a novel approach in the context of solar flares, this method has been utilised in geophysics and other fields. For example, the application of this technique to the diagnostics of automobile gearbox faults was investigated in Liu et al. [2006], while ozone levels in the Earth's atmosphere were analysed by Jánosi and Müller [2005]. More relevantly, this technique was used in helioseismology by Komm et al. [2001] to study the solar convection zone, and application of EMD to solar coronal data was first attempted by Terradas et al. [2004] during the study of propagating EUV waves. The properties of the technique should in principle make it an ideal tool for the study of short, impulsive events such as solar flares, a hypothesis we explore in the following observations.

6.3 Synthetic and observational examples

To investigate the effectiveness of EMD, we apply the technique to three prominent examples of QPP. These are the solar flares of 3rd July 2002, 14th August 2004 and 22nd August 2005. These events were observed in the microwave band at 17 GHz by the Nobeyama Radioheliograph. In addition to investigating empirical mode decomposition, we also compare the Hilbert transform against more conventional wavelet analysis.

However, prior to analysing real data it is useful to examine a simple test problem. This helps us to understand the properties of the Hilbert spectrum under controlled conditions. For this purpose, we examine a simple signal composed of two sine waves, with periods of P_1=30 s and P_2 = 15 s. This signal is displayed in Figure 6.2 along with the associated wavelet and Hilbert transforms.

Naturally, the two periods are easily detected using both methods. Perhaps the most striking aspect of the wavelet is the uncertainty in period of the signals. Even for such an idealised signal, the short overall duration of 150 s results in a large wavelet width in the frequency domain. For example, the period of 30 s could be interpreted as lying anywhere in the range 25-35s based on the centre panel of Figure 6.2. The Hilbert spectrum appears to perform reasonably well in comparision. Both periods are present and the uncertainty in frequency is much smaller. However, even for a perfect sine wave it can be seen that the Hilbert spectrum experiences fluctuations in time. It also suffers from significant end effects. Hence, when applying this technique to more practical examples containing significant noise, one must be cautious. The best approach is to look for regions of continuous, relatively stable power in the Hilbert spectrum. It is also recommended that the edges of the spectrum are neglected, as these must be considered compromised by end-effects.

6.3.1 The flare of 3rd July 2002

The solar flare of 3rd July 2002 was a GOES-class X1.5 event and was observed by the Nobeyama Radioheliograph and the RHESSI satellite. This event was studied in detail

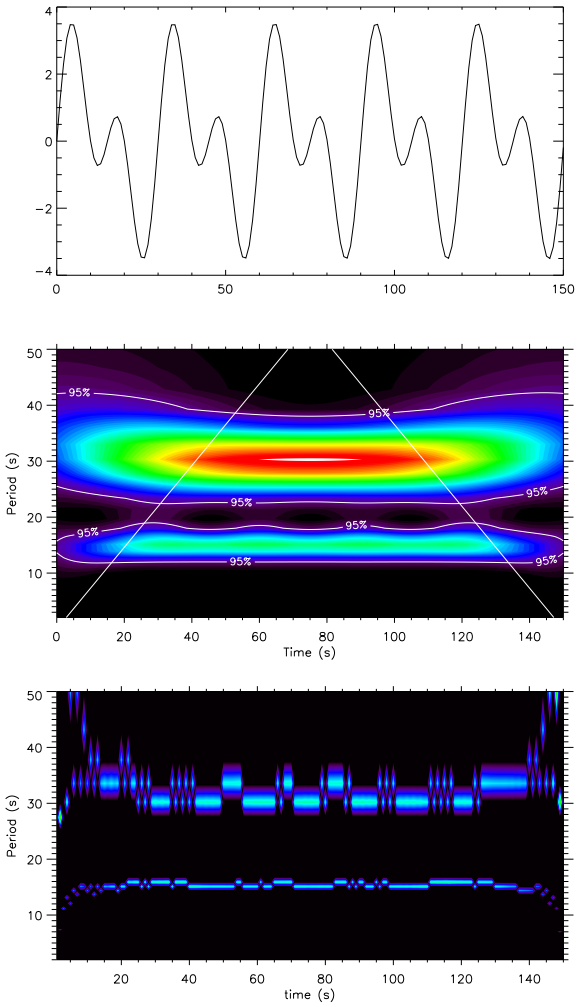

Figure 6.2: Top: A simple test signal composed of two sine waves, with periods 30s and 15s respectively. Centre: The Morlet wavelet transform of the timeseries. Bottom: The Hilbert transform of the timeseries.

in Chapter 5 (see also Inglis and Nakariakov [2009]), where multiple significant periods were reported in both microwave and hard X-ray wavelengths. Thus it makes an ideal event with which to begin the testing of a new technique, particularly one that should confidently detect multiple periods. The time series for this flare was previously shown in Figure 5.1 and Figure 6.1.

The quasi-periodic pulsations are associated with the second phase of this event, between 02:11 and 02:13 UT. It is this region where we apply the empirical mode decomposition. As Figure 6.1 shows, this results in five distinct components, the last of which represents the background trend. To provide a reference via a known technique, we apply the Morlet wavelet to the signal consisting of the first four IMFs. Then, following the recommendations of Huang et al. [1998] we apply the Hilbert spectrum method to these same components. The results of both methods are shown in Figure 6.3.

The most obvious aspect of the wavelet spectrum is the extremely coarse resolution. In fact, the abundance of power in the spectrum makes it difficult to draw any conclusions from the wavelet. Perhaps the only assertion that can be confidently made is that there are significant frequencies present in the data. Quantifying the relevant periods based on the wavelet spectrum is a difficult task. However, in Chapter 5 it was shown that this wavelet can at least be used in conjunction with the Scargle periodogram to help determine whether multiple frequencies or a single evolving mode are present (see Section 5.4).

Let us contrast this with the Hilbert spectrum (Figure 6.3, centre panel). It is immediately apparent that the spectrum has much finer resolution, and also shows a great deal of local variation in frequency. This reinforces an important fact about flaring QPP; such events are not stationary, harmonic waves, but rather anharmonic, noisy, evolutionary events. However, in a sense the Hilbert spectrum is overly sensitive to these local variations, a problem which may be compounded by noise in the signal. In an attempt to improve the results of the Hilbert spectrum, the original signal (shown

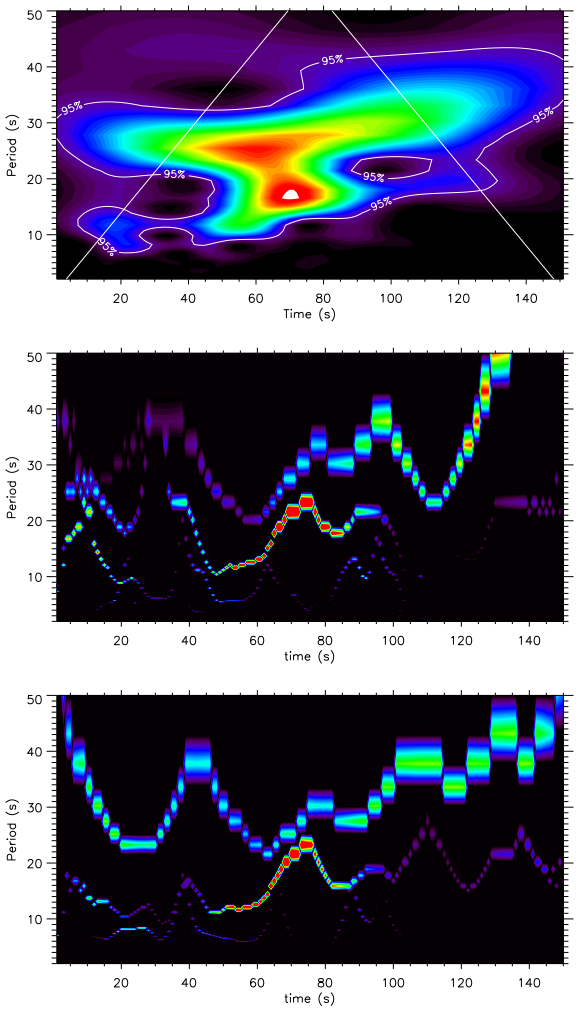

Figure 6.3: Top: Morlet wavelet of the microwave flux from the flare of 3rd July 2002, where EMD has been used to de-trend the signal. Centre: Hilbert spectrum of the IMFs derived from the flare of 3rd July 2002, minus the long-term trend. Bottom: The same as the centre panel, except the original signal has been filtered to remove high-frequency noise. The start in all cases is 02:11:00 UT.

in Figure 6.1) was filtered to remove high-frequency noise. To achieve this, the shortest significant periods were determined from the original Hilbert spectrum shown in the centre panel of Figure 6.3. A bandpass filter was then applied to remove periods that were significantly shorter than this. For the event shown periods less than 5 s were suppressed. Empirical mode decomposition and the Hilbert spectrum is then applied to the remaining signal. The result is shown in the bottom panel of Figure 6.3. From this we can conclude that the exclusion of high-frequency noise has significantly increased the clarity of the spectrum.

A close examination of the modified Hilbert spectrum reveals the presence of two relatively clear tracks, corresponding to different IMFs. Broadly speaking, these lie in the ranges 18 - 22s, and 25 - 35 s. There is also a third track in the range 7 - 12 s, but its amplitude is much smaller than the dominant two, and is barely visible. We can compare this spectrum to the results reported in Chapter 5, where periods of 28 $\pm$ 2 s, 18 $\pm$ 1 s and 12 $\pm$ 1 s were observed. Although the two sets of results are not inconsistent, the intrinsic local modulations in the Hilbert spectrum can make it more difficult interpret than a global technique such as the periodogram, where any local variations are averaged out. However, what the Hilbert spectrum does show unambiguously is that at least two periods, consistent with previous observations, occured simultaneously. This is an important result which supports the conclusion that multiple harmonics of an MHD mode may be present here, rather than a single, rapidly evolving oscillation.

6.3.2 The flare of 14th August 2004

The solar flare of 14th August 2004 was observed by the Nobeyama Radioheliograph in Japan, and by the TRACE satellite. Unfortunately, it was not observed at X-ray wavelengths by RHESSI, which was in the night-time phase of its orbit. The time profile of the radio signature at 17 GHz is shown in Figure 6.4. The flux profile is suggestive of the presence of QPP. Ideally a complete study would consist of time series analysis

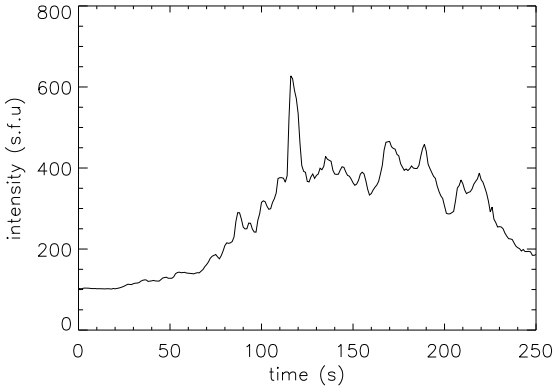

Figure 6.4: Microwave flux from the flare of 14th August 2004 as observed by the Nobeyama Radioheliograph at 17 GHz. The start time is 05:42 UT.

in both radio and X-ray regimes, as well as examining the spatial distribution of any observed significant periods.

In this study however we concentrate on time series analysis of the available radio data. Following the same procedure as for the previous event, both the Morlet wavelet and the Hilbert spectrum are applied to the IMFs resulting from empirical mode decomposition. We subsequently apply high-frequency noise filtering and produce the revised Hilbert spectrum. All three results are shown in Figure 6.5.

From the wavelet spectrum it is clear that some significant frequencies are present in the data, however as before it is difficult to localise them in time or frequency, a consequence of limited data. It does appear that the dominant periods at the beginning of the QPP phase and at its end are very different, varying from around 20 s to 40 s.

Again, we compare this with the result of the Hilbert spectrum. Although some dominant frequencies appear to be present, these are subject to large local variation. In both the unfiltered and filtered spectra, there is a clear track at approximately 20 s, which remains present throughout the QPP phase. Other significant periods are harder to quantify. There appears to be a second significant period of around 30 s present at the

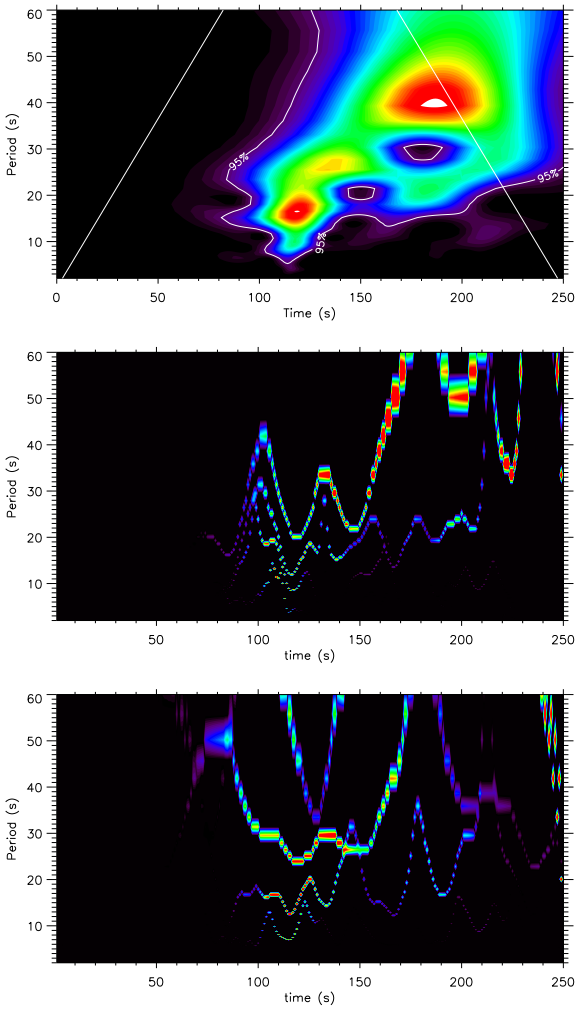

Figure 6.5: Top: wavelet spectrum of the de-trended signal from the flare of 14th August 2004, observed at 17 GHz by the Nobeyama Radioheliograph. Centre: Hilbert spectrum of the significant IMFs derived from the EMD process for the same event. Bottom: Hilbert spectrum of the same event, where high-frequency noise filtering has been applied to the original signal.

beginning of the QPP phase, which then evolves into a long period oscillation consistent with the wavelet spectrum, although it is unclear whether this is a residual background trend that has not been removed via the mode decomposition process. Interestingly, it does not seem that in this case the high-frequency noise filtering has significantly improved the Hilbert spectrum.

Both the wavelet and the Hilbert spectrum suggest that the flare of 14th August 2004 was a multi-periodic QPP event, cerainly including periods of approximately 20 s and 30 s. Other periods may be present but are difficult to quantify using either method. This event merits further study, but we have shown that the Hilbert spectrum is at least comparable with the established wavelet technique in this case.

6.3.3 The flare of 22nd August 2005

Unlike the previous two events, the flare of 22nd August 2005 was associated with single-period quasi-periodic pulsations over long timescales. The microwave flux at 17 GHz is shown in Figure 6.6. This event was studied by Li and Gan [2008], who reported the presence of a period of approximately 240 s. In this context the empirical mode decomposition process can be useful in investigating evolutionary trends in an oscillation period. Such evolutionary information is intrinsically unavailable using methods such as the Scargle periodogram or Fourier transform, which provide global information only. The wavelet on the other hand should detect significant evolution in the signal, as should the Hilbert spectrum. This provides us with an excellent opportunity to compare the two methods.

In Li and Gan [2008] a fitting technique was used to estimate the period of the oscillation. However, the drawback of this technique is that the presence of a single period is implicitly assumed. Here we utilise EMD and apply the Morlet wavelet and the Hilbert transform by way of comparison. The result is shown in Figure 6.7, where for brevity we have reproduced only the noise-filtered Hilbert spectrum. Note that in this case, due to the number of IMFs derived from this signal, it is necessary to discard

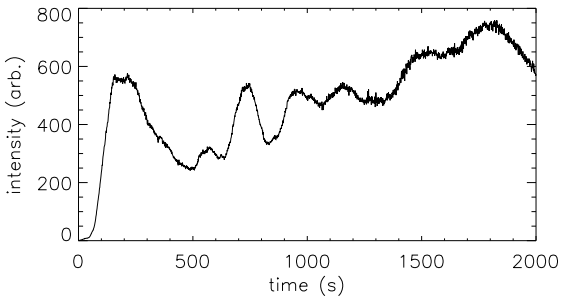

Figure 6.6: Total microwave flux from the solar flare of 22nd August 2005, as observed by the Nobeyama Radioheliograph. The start time is 23:42 UT.

several in order to view the time range of interest.

In both spectra the initial rise of microwave flux is mistakenly treated as an oscillatory signal, with a period in the range 300 - 400s. The Hilbert spectrum is especially affected by this. However, both techniques also correctly detect the signal reported in Li and Gan [2008] from approximately $t = 500$ s onwards. The Hilbert spectrum suggests a slight lengthening of the dominant period as the flare progresses, until the signal peters out at around t=1300 s. Interestingly, the Hilbert spectrum shows a clear diminution in spectral amplitude, corresponding well to the damping of the signal that may be seen in Figure 6.6 and was noted by Li and Gan [2008]. Although the wavelet and Hilbert spectra are consistent, the wavelet does not indicate the presence of signal damping, even though it is visible by eye.

Utilising empirical mode decomposition, the Morlet wavelet and the Hilbert spectrum, we have confirmed the findings of Li and Gan [2008] for the solar flare of 22nd August 2005. By simply discarding IMFs corresponding to time ranges longer than that of interest, we were able to focus on the spectral region of interest and identify the period of 240 s. The Hilbert spectrum also succesfully detected a slight evolution of the dominant period, as well as evidence of signal damping, neither of which were evident from the wavelet. Interestingly, in De Moortel et al. [2002] and De Moortel et al. [2004]

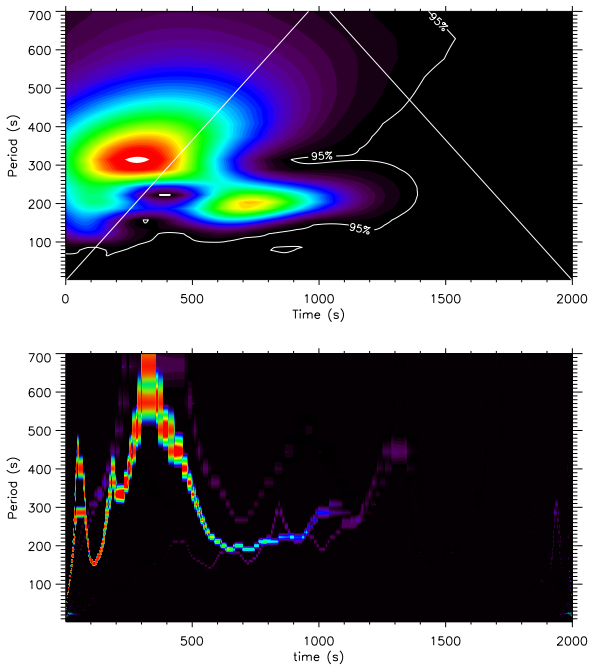

Figure 6.7: Wavelet and Hilbert spectra of the significant IMFs derived from the microwave flux at 17 GHz from the solar flare of 22nd August 2005.

is was suggested that wavelet analysis should be able to distinguish between a damped signal and a continuous one, or an abruptly curtailed signal. Unfortunately we were unable to achieve this here, although these authors also emphasised the sensitivity of the wavelet to many parameters. Thus the failure to detect damping in one example should not be taken as a general indictment of the method. In any case, this event demonstrates that EMD and the Hilbert spectrum are applicable not only to fast QPP events, but also to long-period oscillations.

6.4 Discussion

In this chapter we have examined the applicability of empirical mode decomposition and the Hilbert spectrum to the analysis of coronal wave studies, in particular solar flares. Although a relatively new tool in the context of solar physics, this method has been successfully utilised in other fields, such as mechanical engineering and atmospheric science. As a first task, the consistency of EMD was tested by using a flaring event with known multiple periods. The event in question was the solar flare of 3rd July 2002, examined in detail in Chapter 5. Encouragingly, we found that the decomposition of the original signal into multiple components or IMFs revealed the presence of two of the three periods reported in the previous chapter. To show this, we applied two separate visualisation methods. The first of these was the Hilbert spectrum, comprehensively described in Huang et al. [1998] and covered in Section 6.2. The second was the more conventional Morlet wavelet. The two techniques were shown to be in good agreement, both with each other and with the previous results detailed in Chapter 5. Furthermore, the Hilbert spectrum supported the conclusion that the detected periods occurred simultaneously and that by extension multiple harmonics of an MHD mode may be present.

The same analysis was applied to the powerful flare of 14th August 2004. As before, the empirical mode decomposition technique was used to remove background trends and the remaining signal was visualised using both the wavelet and the Hilbert

spectrum. Both methods suggested the presence of multiple potentially significant periods. A conservative estimate gave periods of approximately 20 s and 30 s, with a possible longer period of 40 - 50 s present during the latter stages of the flare. It is unclear whether this is simply a residual background trend or a genuine oscillation.

Finally, we tested the effectiveness of EMD and the Hilbert spectrum on an event exhibiting long-period QPP. This event was previously analysed by Li and Gan [2008], who used a wave fitting technique to illustrate the presence of a damped oscillation of $P \approx 240$ s. By selecting the relevant IMFs this period was confirmed by both the wavelet and the Hilbert spectrum. However, unlike the wavelet, the Hilbert spectrum was also able to detect a slight modulation of the dominant period over the course of the flare. It also clearly showed a diminution in amplitude corresponding to the signal damping.

The potential of empirical mode decomposition and the Hilbert spectrum can be clearly seen from these examples. One of the principal advantages is the automatic processing of background trends, which are simply stored in extra IMF components. This removes the necessity for the user to judge the trend manually, as is the case with existing methods such as the Scargle periodogram and the wavelet. Further, the Hilbert spectrum has been demonstrated to give results consistent with those obtained using other methods, in particular the wavelet. Multiple periods in the flares of 3rd July 2002 and 14th August 2005 were detected, consistent with previous studies for the former. The previously published results of Li and Gan [2008] were confirmed for the flare of 22nd August 2005. This highlights the suitability of empirical mode decomposition for future studies of oscillations in flares and coronal loops.

However, significant questions remain and further work needs to be undertaken to prove the value of this method. In particular, although the process of decomposing a real, impulsive signal into components is robust and effective, aspects of the Hilbert transform remain counter-intuitive. The definition of instantaneous frequency, for example, is not obviously physical. An accurate estimation of the significance of detected frequencies

also remains problematic. Additionally, the Hilbert spectrum, as demonstrated in this chapter, is very susceptible to noise, a problem reflected in the large local variations in frequency shown in both Figure 6.3 and 6.5. In some cases this problem can be mitigated by careful suppression of high-frequency noise. Provided that this noise is sufficiently far from the frequency range of interest, the stability of the Hilbert spectrum is improved, as was shown in Figure 6.3.

Despite these outstanding questions, EMD and the Hilbert spectrum can be used in conjunction with existing methods to enhance observational studies. In the future both methods are potentially powerful tools in their own right, and are particularly relevant in the context of pulsations in solar flares, typically short, impulsive events with large evolutionary trends. Their use in tandem with established methods may lead to significant advances in the study of solar and stellar oscillations.

Chapter 7

Summary and discussion

In this work we have engaged in detailed analysis and discussion of many aspects of quasi-periodic pulsations in solar flares. In Chapter 1 we introduced the background physics and most important concepts of the Sun itself. Of particular importance is the solar activity cycle, which dictates the number of sunspots, flares, CMEs and other phenomena occurring in the solar atmosphere. Fortunately, the Sun is under constant observation by a wide range of scientific instruments. In the context of flares, the most important of these are the Nobeyama Radioheliograph in Japan, and the RHESSI satellite in low earth orbit.

In Chapter 2 we introduced one of the main theoretical mechanisms used to describe the behaviour of plasma, the theory of magnetohydrodynamics (MHD). A combination of electromagnetism and fluid dynamics, this framework treats a plasma as a single electrically conducting fluid. Thus it is ideal for studying large-scale, relatively slow plasma dynamics without the necessity of describing individual particles. In addition, MHD predicts the existence of waves. These waves are a plausible explanation for long-standing problems in solar physics, such as the coronal heating problem. They are also likely sources of many oscillatory phenomena observed in the corona, including flaring QPP. This can be shown via the magnetic cylinder model, introduced in Section 2.2.1. This is a popular tool for modelling real coronal structures, such as loops, flares, various

filaments and plumes. From this model, wave equations and dispersion relations can be derived, showing the existence of several wave modes, including the sausage, kink, and Alfvén modes. These modes can either be trapped (i.e confined to the interior of the cylinder), or leaky (where the wave energy disappates into the surrounding plasma over time). In either case, these waves have the potential to act as drivers for observable pulsations in flares. In Section 2.3 we introduce the concept of pulsations in flares in detail. This phenomenon has been a feature of solar flare observations for decades, yet they have remained poorly understood until relatively recently. Advances in technological capability in the last decade have led to more concrete analysis of such events. From this it is possible to conclude that flaring QPP is not the result of a single mechanism, but of several equally viable mechanisms.

Chapter 3 begins the exposition of original work. Here we focus on one of the main types of MHD waves, the fast magnetoacoustic sausage mode. This mode is very interesting in the context of flaring QPP because it is capable of generating variations in both microwave, soft X-ray and hard X-ray emission. Microwave emission may be generated via the gyrosynchotron mechanism [Ramaty, 1969; Dulk and Marsh, 1982]. Soft X-rays are in general sourced from the body of the loop itself, thus the compressibility of the sausage mode leads to density and temperature variations and by extension fluctuations in soft X-rays. The modulation of hard X-rays occurs differently, and is thought to be the result of periodic precipitation of particles towards the flare footpoints [Zaitsev and Stepanov, 1982]. Previous numerical studies of the sausage mode have already established many of the mode's fundamentals. However, all of these studies have been carried out using low β values, and it is unclear whether a large β, typical for hot and dense flaring loops, would have a strong impact on the results. Moreover, although the study of period ratios has already been carried out for the kink mode [Andries et al., 2005; McEwan et al., 2008], the relationship between sausage mode harmonics remains unclear. In this chapter, we established that the inclusion of a finite value of β inside a loop structure does have a noticeable, though small, effect

on both the period of the global sausage mode and its cut-off value. For the period, the variation remained less than 5% for β values of order 1. Thus we were able to confirm that, even in the significant-β regime, the period of the sausage mode remains primarily a function of loop length L. For the cut-off wavenumber, it was found that increasing the value of β led to a small increase in the confinement of the sausage mode. However, as with the mode period, this variation was small compared with the effects of other parameters. In particular, the density contrast ratio between the loop centre and the surroundings was shown to have a very strong effect on the cut-off wavenumber, meaning that for very dense loops a trapped mode may remain supported for very large L. For a density contrast ratio of 1000 and a loop width of 3 Mm, a trapped mode could conceivably be supported for loops as long as 300 Mm. Finally, we performed a detailed study of the $P_1/2P_2$ ratio for the sausage mode. As a result of dispersion, these harmonics are expected to deviate from the simple $1/N$ pattern of a simple resonator. This was confirmed both numerically and analytically. We have illustrated that as the wavenumber decreases, the deviation from the ideal case increases, such that at very low values of ka the $P_1/2P_2$ ratio can approach 0.5 for very dense loops. As ka increases, the value of the harmonic ratio approaches the ideal value of unity regardless of the density contrast in the loop. The power of this result was briefly illustrated using two observational examples, where we were able to use the reported period ratios to make judgements on the probable cause.

In Chapter 4 we switch the emphasis to observational study of QPP events. Recent advances in observational instruments have broadened the possibilities for remote diagnostics of coronal phenomena. We illustrate this by performing spatially resolved analysis on a M3.1-class flare from 8th May 1998, using microwave and X-ray data from the Nobeyama Radioheliograph and Yohkoh satellite respectively. Using the Scargle periodogram method, a period of P=16 s was discovered in both microwave and X-ray time profiles. To carry out the spatially resolved analysis, the technique of cross-correlation mapping was developed. This mapping allowed us to visualise the correlation

in time of all the pixels in the microwave images with respect to a master, or reference pixel. The result unambiguously showed that for this flare the entire loop was oscillating in phase with the same dominant period of $P = 16$s. These results lead naturally to several conclusions. Firstly, the fact that the oscillation has a significant spatial extent indicates that it may be a trapped MHD mode. Secondly, the in-phase relationship of different parts of the loop suggests the presence of a global sausage mode, which symmetrically perturbs the loop axis. The observed period is perhaps typical of this mode, and consistent with previous observations [Melnikov et al., 2005]. Also, the presence of oscillations in the thermal X-ray range (13-23 keV) is another factor in favour of the sausage mode interpretation, since by its very nature the flaring flux tube is periodically expanded and compressed. Therefore, although the possibility of a periodic magnetic reconnection event cannot be ruled out, we conclude that the QPP observed on 8th May 1998 are likely the result of a magnetoacoustic sausage mode.

Although the power of spatially resolved analysis is clear, realistically there remain many circumstances where it is not possible. In particular, studies of stellar oscillations clearly lack this capability. Therefore in Chapter 5 we addressed the question of what progress may be achieved in the study of flaring QPP when spatial resolution is unavailable. In this context we studied an X1.5-class flare from 3rd July 2002 using the Nobeyama Radioheliograph and the RHESSI satellite. This event was powerful enough to compromise the pointing accuracy of the Nobeyama Radioheliograph, thus rendering our cross-correlation mapping technique unreliable. Using detailed time series analysis, we discovered the presence of three distinct periods in this flare, with $P_1 = 28$ s, $P_2 = 18$ s and $P_3 = 12$ s. As was shown in Chapter 3 from a theoretical perspective, period ratios can potentially be used to discriminate between QPP mechanisms. Thus we sought to apply this technique from an observational point of view. The period ratios of $P_2/P_1 = 0.64$ and $P_3/P_1 = 0.43$ are consistent with the effects of dispersion on fast magnetoacoustic modes. This information already allows us to conclude that the observed oscillations are spatial harmonics of a resonator, i.e. a coronal loop. Furthermore,

unlike the flare from 8th May 1998, there is no evidence of QPP in the thermal X-ray range. In this case, oscillations are only seen in microwaves and in non-thermal X-rays. This makes the presence of a sausage mode unlikely. This led us to the conclusion that the observed QPP is the result of a kink mode leading to magnetic reconnection.

The observational results presented in Chapters 4 and 5 can make a significant contribution to further coronal oscillation studies. However, the time series analysis techniques employed here and throughout the community, in particular the Scargle periodogram and wavelet analysis, suffer from certain limitations. Principal among these is the need for manual background subtraction, whether via a fitting function or frequency filtering. Therefore, in Chapter 6 we investigate a promising technique that may remove the need for this process, and further is designed explicitly for the study of non-linear, impulsive events. This technique is known as empirical mode decomposition (EMD). To test the potential of EMD and the associated Hilbert spectrum, it was applied to the time series of three suspected QPP events, including the previously studied multi-periodic flare of 3rd July 2002. Without any direction from the user, we were able to reproduce the periods $P_1 = 28$ s and $P_2 = 18$ s found in Chapter 5, although the presence of the third period was not confirmed. Similarly, we were able to show the probable presence of multiple periods in the flare from 14th August 2004, and confirm the presence of long period oscillations for the flare of 22nd August 2005 as reported by Li and Gan [2008]. The potential of empirical mode decomposition and the Hilbert spectrum is clear, although some important questions remain. The lack of a need to manually subtract a background function from an input signal is a distinct advantage. Further, we have proven the consistency of this technique with robust existing methods. Thus, these methods may play an important role in future studies of coronal waves and flaring QPP, especially when used in conjunction with existing methods.

The work presented in this thesis demonstrates that significant progress is being made in our understanding of flaring QPP. The new techniques that we have developed and applied have enabled us make informed judgements about the causes of QPP in

specific events, and will provide new insights in the future. However, the study of flaring QPP remains a complex and challenging subject in which significant questions remain.

Perhaps the next stage in the study of flaring QPP is to establish a statistical picture of the phenomenon. In this thesis, and throughout the literature, QPP events have been studied in interesting but isolated cases. In part this is due to the difficulty in identifying and confidently analysing such events. However as a consequence of this, although we are able to estimate coronal parameters and identify MHD mode mechanisms in isolated cases, as we have done in this thesis, it remains essential to build up a body of complementary evidence so that we can be truly confident in our assertions.

For example, in our study of a multi-periodic event in Chapter 5, we observed a period ratio consistent with the dispersive effects of MHD modes. An important study would be an extension of this idea to many such events, i.e. a statistical survey of as many multi-periodic events as possible. In this way we would be able to establish whether such ratios are a general characteristic of QPP events or not. This would greatly help us to determine whether flaring QPP can always be considered consistent with MHD wave modes. Similarly, surveys of this kind could provide multiple estimates of coronal parameters such as the magnetic field strength and answer such basic questions as how common QPP events are in solar flares.

In any case, further development of techniques and advances in instrumentation are still needed to fully understand and appreciate this phenomenon.

Bibliography

J. Andries, I. Arregui, and M. Goossens. Determination of the Coronal Density Stratification from the Observation of Harmonic Coronal Loop Oscillations. *The Astrophysical Journal Letters*, 624:L57–L60, May 2005. doi: 10.1086/430347.

T. D. Arber, A. W. Longbottom, C. L. Gerrard, and A. M. Milne. A Staggered Grid, Lagrangian-Eulerian Remap Code for 3-D MHD Simulations. *Journal of Computational Physics*, 171:151–181, July 2001. doi: 10.1006/jcph.2001.6780.

A. Asai, M. Shimojo, H. Isobe, T. Morimoto, T. Yokoyama, K. Shibasaki, and H. Nakajima. Periodic Acceleration of Electrons in the 1998 November 10 Solar Flare. *The Astrophysical Journal Letters*, 562:L103–L106, November 2001. doi: 10.1086/338052.

M. J. Aschwanden. *Physics of the Solar Corona. An Introduction with Problems and Solutions (2nd edition)*. December 2005.

R. B. Blackman and J. W. Tukey. *The measurement of power spectra, from the point of view of communications engineering*. 1959.

H. Carmichael. A Process for Flares. *NASA Special Publication*, 50:451–+, 1964.

F. C. Cooper, V. M. Nakariakov, and D. R. Williams. Short period fast waves in solar coronal loops. *Astronomy & Astrophysics*, 409:325–330, October 2003. doi: 10.1051/0004-6361:20031071.

I. De Moortel, A. W. Hood, and J. Ireland. Coronal seismology through wavelet analysis. *Astronomy & Astrophysics*, 381:311–323, January 2002. doi: 10.1051/0004-6361:20011659.

I. De Moortel, S. A. Munday, and A. W. Hood. Wavelet Analysis: the effect of varying basic wavelet parameters. *Solar Physics*, 222:203–228, August 2004. doi: 10.1023/B:SOLA.0000043578.01201.2d.

I. De Moortel, P. Browning, S. J. Bradshaw, B. Pintér, and E. P. Kontar. The way forward for coronal heating. *Astronomy and Geophysics*, 49(3):030000–3, June 2008. doi: 10.1111/j.1468-4004.2008.49321.x.

A. J. Díaz and B. Roberts. Slow MHD oscillations in density structured coronal loops. *Astronomy & Astrophysics*, 458:975–985, November 2006. doi: 10.1051/0004-6361:20065923.

V. Domingo, B. Fleck, and A. I. Poland. SOHO: The Solar and Heliospheric Observatory. *Space Science Reviews*, 72:81–84, April 1995. doi: 10.1007/BF00768758.

G. R. Donnelly, A. J. Díaz, and B. Roberts. Effect of coronal structure on loop oscillations. *Astronomy & Astrophysics*, 457:707–715, October 2006. doi: 10.1051/0004-6361:20065524.

G. A. Dulk and K. A. Marsh. Simplified expressions for the gyrosynchrotron radiation from mildly relativistic, nonthermal and thermal electrons. *The Astrophysical Journal*, 259:350–358, August 1982. doi: 10.1086/160171.

M. V. Dymova and M. S. Ruderman. Resonantly damped oscillations of longitudinally stratified coronal loops. *Astronomy & Astrophysics*, 457:1059–1070, October 2006. doi: 10.1051/0004-6361:20065051.

J. A. Eddy. The Maunder Minimum. *Science*, 192:1189–1202, June 1976.

P. M. Edwin and B. Roberts. Wave propagation in a magnetically structured atmosphere. III - The slab in a magnetic environment. *Solar Physics*, 76:239–259, March 1982. doi: 10.1007/BF00170986.

P. M. Edwin and B. Roberts. Wave propagation in a magnetic cylinder. *Solar Physics*, 88:179–191, October 1983.

R. Erdélyi and V. Fedun. Sausage MHD Waves in Incompressible Flux Tubes with Twisted Magnetic Fields. *Solar Physics*, 238:41–59, October 2006. doi: 10.1007/s11207-006-0217-z.

G. D. Fleishman, T. S. Bastian, and D. E. Gary. Broadband Quasi-periodic Radio and X-Ray Pulsations in a Solar Flare. *The Astrophysical Journal*, 684:1433–1447, September 2008. doi: 10.1086/589821.

L. Fletcher and H. S. Hudson. Impulsive Phase Flare Energy Transport by Large-Scale Alfvén Waves and the Electron Acceleration Problem. *The Astrophysical Journal*, 675:1645–1655, March 2008. doi: 10.1086/527044.

C. Foullon, E. Verwichte, V. M. Nakariakov, and L. Fletcher. X-ray quasi-periodic pulsations in solar flares as magnetohydrodynamic oscillations. *Astronomy & Astrophysics*, 440:L59–L62, September 2005. doi: 10.1051/0004-6361:200500169.

V. V. Grechnev, S. M. White, and M. R. Kundu. Quasi-periodic Pulsations in a Solar Microwave Burst. *The Astrophysical Journal*, 588:1163–1175, May 2003. doi: 10.1086/374315.

T. Hirayama. Theoretical Model of Flares and Prominences. I: Evaporating Flare Model. *Solar Physics*, 34:323–338, February 1974. doi: 10.1007/BF00153671.

J. H. Horne and S. L. Baliunas. A prescription for period analysis of unevenly sampled time series. *The Astrophysical Journal*, 302:757–763, 1986.

N. E. Huang, Z. Shen, S. R. Long, M. C. Wu, H. H. Shih, Q. Zheng, N.-C. Yen, C. C. Tung, and H. H. Liu. The empirical mode decomposition and the Hilbert spectrum for nonlinear and non-stationary time series analysis. *Royal Society of London Proceedings Series A*, 454:903–+, March 1998.

A. R. Inglis and V. M. Nakariakov. A multi-periodic oscillatory event in a solar flare. *Astronomy & Astrophysics*, 493:259–266, January 2009. doi: 10.1051/0004-6361:200810473.

A. R. Inglis, V. M. Nakariakov, and V. F. Melnikov. Multi-wavelength spatially resolved analysis of quasi-periodic pulsations in a solar flare. *Astronomy & Astrophysics*, 487: 1147–1153, September 2008. doi: 10.1051/0004-6361:20079323.

A. R. Inglis, T. van Doorsselaere, C. S. Brady, and V. M. Nakariakov. Characteristics of magnetoacoustic sausage modes. *Astronomy & Astrophysics*, 503:569–575, August 2009. doi: 10.1051/0004-6361/200912088.

I. M. Jánosi and R. Müller. Empirical mode decomposition and correlation properties of long daily ozone records. *Physical Review E*, 71(5):056126–+, May 2005. doi: 10.1103/PhysRevE.71.056126.

S. R. Kane, K. Kai, T. Kosugi, S. Enome, P. B. Landecker, and D. L. McKenzie. Acceleration and confinement of energetic particles in the 1980 June 7 solar flare. *The Astrophysical Journal*, 271:376–387, August 1983. doi: 10.1086/161203.

B. Kliem, M. Karlický, and A. O. Benz. Solar flare radio pulsations as a signature of dynamic magnetic reconnection. *Astronomy & Astrophysics*, 360:715–728, August 2000.

R. W. Komm, F. Hill, and R. Howe. Empirical Mode Decomposition and Hilbert Analysis Applied to Rotation Residuals of the Solar Convection Zone. *The Astrophysical Journal*, 558:428–441, September 2001. doi: 10.1086/322464.

R. A. Kopp and G. W. Pneuman. Magnetic reconnection in the corona and the loop prominence phenomenon. *Solar Physics*, 50:85–98, October 1976. doi: 10.1007/BF00206193.

Y. G. Kopylova, A. V. Melnikov, A. V. Stepanov, Y. T. Tsap, and T. B. Goldvarg. Oscillations of coronal loops and second pulsations of solar radio emission. *Astronomy Letters*, 33:706–713, October 2007. doi: 10.1134/S1063773707100088.

S. Krucker and R. P. Lin. Hard X-Ray Emissions from Partially Occulted Solar Flares. *The Astrophysical Journal*, 673:1181–1187, February 2008. doi: 10.1086/524010.

K.-M. Lau and H. Weng. Climate Signal Detection Using Wavelet Transform: How to Make a Time Series Sing. *Bulletin of the American Meteorological Society*, 76:2391–2402, December 1995. doi: 10.1175/1520-0477(1995)076¡2391:CSDUWT¿2.0.CO;2.

Y. P. Li and W. Q. Gan. Observational Studies of the X-Ray Quasi-Periodic Oscillations of a Solar Flare. *Solar Physics*, 247:77–85, January 2008. doi: 10.1007/s11207-007-9092-5.

R. P. Lin, B. R. Dennis, G. J. Hurford, D. M. Smith, A. Zehnder, P. R. Harvey, D. W. Curtis, D. Pankow, P. Turin, M. Bester, A. Csillaghy, M. Lewis, N. Madden, H. F. van Beek, M. Appleby, T. Raudorf, J. McTiernan, R. Ramaty, E. Schmahl, R. Schwartz, S. Krucker, R. Abiad, T. Quinn, P. Berg, M. Hashii, R. Sterling, R. Jackson, R. Pratt, R. D. Campbell, D. Malone, D. Landis, C. P. Barrington-Leigh, S. Slassi-Sennou, C. Cork, D. Clark, D. Amato, L. Orwig, R. Boyle, I. S. Banks, K. Shirey, A. K. Tolbert, D. Zarro, F. Snow, K. Thomsen, R. Henneck, A. McHedlishvili, P. Ming, M. Fivian, J. Jordan, R. Wanner, J. Crubb, J. Preble, M. Matranga, A. Benz, H. Hudson, R. C. Canfield, G. D. Holman, C. Crannell, T. Kosugi, A. G. Emslie, N. Vilmer, J. C. Brown, C. Johns-Krull, M. Aschwanden, T. Metcalf, and A. Conway. The Reuven Ramaty High-Energy Solar Spectroscopic Imager (RHESSI). *Solar Physics*, 210:3–32, November 2002. doi: 10.1023/A:1022428818870.

B. Liu, S. Riemenschneider, and Y. Xu. Gearbox fault diagnosis using empirical mode decomposition and Hilbert spectrum. *Mechanical Systems and Signal Processing*, 20: 718–734, April 2006. doi: 10.1016/j.ymssp.2005.02.003.

N. R. Lomb. Least-squares frequency analysis of unequally spaced data. *Astrophysics and Space Science*, 39:447–462, February 1976. doi: 10.1007/BF00648343.

J. T. Mariska. Characteristics of Solar Flare Doppler-Shift Oscillations Observed with the Bragg Crystal Spectrometer on Yohkoh. *The Astrophysical Journal*, 639:484–494, March 2006. doi: 10.1086/499296.

S. Masuda, T. Kosugi, H. Hara, S. Tsuneta, and Y. Ogawara. A loop-top hard x-ray source in aa compact solar flare as evidence of magnetic reconnection. *Nature*, 371: 495–497, 1994.

M. Mathioudakis, J. H. Seiradakis, D. R. Williams, S. Avgoloupis, D. S. Bloomfield, and R. T. J. McAteer. White-light oscillations during a flare on II Peg. *Astronomy & Astrophysics*, 403:1101–1104, June 2003. doi: 10.1051/0004-6361:20030394.

R. T. J. McAteer, P. T. Gallagher, D. S. Brown, D. S. Bloomfield, R. Moore, D. R. Williams, M. Mathioudakis, A. Katsiyannis, and F. P. Keenan. Observations of Hα Intensity Oscillations in a Flare Ribbon. *The Astrophysical Journal*, 620:1101–1106, February 2005. doi: 10.1086/427084.

M. P. McEwan, A. J. Díaz, and B. Roberts. Analytical determination of coronal parameters using the period ratio P1/2P2. *Astronomy & Astrophysics*, 481:819–825, April 2008. doi: 10.1051/0004-6361:20078016.

D. E. McKenzie. Signatures of Reconnection in Eruptive Flares [Invited]. In P. C. H. Martens and D. Cauffman, editors, *Multi-Wavelength Observations of Coronal Structure and Dynamics*, pages 155–+, January 2002.

J. A. McLaughlin, I. de Moortel, A. W. Hood, and C. S. Brady. Nonlinear fast magnetoacoustic wave propagation in the neighbourhood of a 2D magnetic X-point: oscillatory reconnection. *Astronomy & Astrophysics*, 493:227–240, January 2009. doi: 10.1051/0004-6361:200810465.

V. F. Melnikov, V. E. Reznikova, K. Shibasaki, and V. M. Nakariakov. Spatially resolved microwave pulsations of a flare loop. *Astronomy & Astrophysics*, 439:727–736, 2005.

H. Mészárosová, M. Karlický, J. Rybák, F. Fárník, and K. Jiřička. Long period variations of dm-radio and X-ray fluxes in three X-class flares. *Astronomy & Astrophysics*, 460: 865–874, December 2006. doi: 10.1051/0004-6361:20065750.

U. Mitra-Kraev, L. K. Harra, D. R. Williams, and E. Kraev. The first observed stellar X-ray flare oscillation: Constraints on the flare loop length and the magnetic field. *Astronomy & Astrophysics*, 436:1041–1047, June 2005. doi: 10.1051/0004-6361:20052834.

K. Muglach and H. Balthasar. Influence of Instrumental Effects on High Frequency Oscillations Observed with Trace. In D. E. Innes, A. Lagg, and S. A. Solanki, editors, *Chromospheric and Coronal Magnetic Fields*, volume 596 of *ESA Special Publication*, November 2005.

M. J. Murray, L. van Driel-Gesztelyi, and D. Baker. Simulations of emerging flux in a coronal hole: oscillatory reconnection. *Astronomy & Astrophysics*, 494:329–337, January 2009. doi: 10.1051/0004-6361:200810406.

H. Nakajima, M. Nishio, S. Enome, K. Shibasaki, T. Takano, Y. Hanaoka, C. Torii, H. Sekiguchi, T. Bushimata, S. Kawashima, N. Shinohara, Y. Irimajiri, H. Koshiishi, T. Kosugi, Y. Shiomi, M. Sawa, and K. Kai. The Nobeyama radioheliograph. *IEEE Proceedings*, 82:705–713, May 1994.

V. M. Nakariakov. MHD oscillations in solar and stellar coronae: Current re-

sults and perspectives. *Advances in Space Research*, 39:1804–1813, 2007. doi: 10.1016/j.asr.2007.01.044.

V. M. Nakariakov. Magnetohydrodynamic seismology of solar and stellar coronae. *Journal of Physics Conference Series*, 118(1):012038–+, October 2008. doi: 10.1088/1742-6596/118/1/012038.

V. M. Nakariakov and D. B. King. Coronal Periodmaps. *Solar Physics*, 241:397–409, April 2007. doi: 10.1007/s11207-007-0348-x.

V. M. Nakariakov and V. F. Melnikov. Modulation of gyrosynchrotron emission in solar and stellar flares by slow magnetoacoustic oscillations. *Astronomy & Astrophysics*, 446:1151–1156, February 2006. doi: 10.1051/0004-6361:20053944.

V. M. Nakariakov and B. Roberts. Magnetosonic Waves in Structured Atmospheres with Steady Flows, I. *Solar Physics*, 159:213–228, July 1995a. doi: 10.1007/BF00686530.

V. M. Nakariakov and B. Roberts. On Fast Magnetosonic Coronal Pulsations. *Solar Physics*, 159:399–402, July 1995b. doi: 10.1007/BF00686541.

V. M. Nakariakov and E. Verwichte. Coronal Waves and Oscillations. *Living Reviews in Solar Physics*, 2:3–+, July 2005.

V. M. Nakariakov, V. F. Melnikov, and V. E. Reznikova. Global sausage modes of coronal loops. *Astronomy & Astrophysics*, 412:L7–L10, December 2003. doi: 10.1051/0004-6361:20031660.

V. M. Nakariakov, T. D. Arber, C. E. Ault, A. C. Katsiyannis, D. R. Williams, and F. P. Keenan. Time signatures of impulsively generated coronal fast wave trains. *Monthly Notices of the Royal Astronomical Society*, 349:705–709, April 2004. doi: 10.1111/j.1365-2966.2004.07537.x.

V. M. Nakariakov, C. Foullon, E. Verwichte, and N. P. Young. Quasi-periodic modulation of solar and stellar flaring emission by magnetohydrodynamic oscillations in a nearby

loop. *Astronomy & Astrophysics*, 452:343–346, June 2006. doi: 10.1051/0004-6361:20054608.

M. Ossendrijver. The solar dynamo. *Astronomy and Astrophysics Review*, 11:287–367, 2003. doi: 10.1007/s00159-003-0019-3.

D. J. Pascoe, V. M. Nakariakov, and T. D. Arber. Sausage oscillations of coronal loops. *Astronomy & Astrophysics*, 461:1149–1154, January 2007a. doi: 10.1051/0004-6361:20065986.

D. J. Pascoe, V. M. Nakariakov, and T. D. Arber. Sausage Oscillations in Multishell Coronal Structures. *Solar Physics*, 246:165–175, November 2007b. doi: 10.1007/s11207-007-9055-x.

D. J. Pascoe, V. M. Nakariakov, T. D. Arber, and K. Murawski. Sausage oscillations in loops with a non-uniform cross-section. *Astronomy & Astrophysics*, 494:1119–1125, February 2009.

R. Ramaty. Gyrosynchrotron Emission and Absorption in a Magnetoactive Plasma. *The Astrophysical Journal*, 158:753–+, November 1969. doi: 10.1086/150235.

J. D. Scargle. Studies in astronomical time series analysis ii: Statistical aspects of spectral analysis of unevenly spaced data. *The Astrophysical Journal*, 263:835–853, 1982.

K. Shibasaki. High-Beta Disruption in the Solar Atmosphere. *The Astrophysical Journal*, 557:326–331, August 2001. doi: 10.1086/321651.

A. K. Srivastava, T. V. Zaqarashvili, W. Uddin, B. N. Dwivedi, and P. Kumar. Observation of multiple sausage oscillations in cool post-flare loop. *Monthly Notices of the Royal Astronomical Society*, 388:1899–1903, August 2008. doi: 10.1111/j.1365-2966.2008.13532.x.

A. V. Stepanov, Y. G. Kopylova, Y. T. Tsap, K. Shibasaki, V. F. Melnikov, and T. B. Goldvarg. Pulsations of Microwave Emission and Flare Plasma Diagnostics. *Astronomy Letters*, 30:480–488, July 2004. doi: 10.1134/1.1774400.

P. A. Sturrock. Model of the High-Energy Phase of Solar Flares. *Nature*, 211:695–697, August 1966. doi: 10.1038/211695a0.

K. F. Tapping. A torsional wave model for solar radio pulsations. *Solar Physics*, 87: 177–186, August 1983.

J. Terradas, R. Oliver, and J. L. Ballester. Application of Statistical Techniques to the Analysis of Solar Coronal Oscillations. *The Astrophysical Journal*, 614:435–447, October 2004. doi: 10.1086/423332.

J. Terradas, R. Oliver, and J. L. Ballester. On the excitation of trapped and leaky modes in coronal slabs. *Astronomy & Astrophysics*, 441:371–378, October 2005. doi: 10.1051/0004-6361:20053198.

J. Terradas, R. Oliver, and J. L. Ballester. Damping of Kink Oscillations in Curved Coronal Loops. *The Astrophysical Journal Letters*, 650:L91–L94, October 2006. doi: 10.1086/508569.

S. M. Tobias. The solar dynamo. *Royal Society of London Philosophical Transactions Series A*, 360:2741–2756, December 2002. doi: 10.1098/rsta.2002.1090.

Christopher Torrence and Gilbert P. Compo. A practical guide to wavelet analysis. *Bulletin of the American Meteorological Society*, 79:61–78, 1998.

Y. Uchida. Diagnosis of Coronal Magnetic Structure by Flare-Associated Hydromagnetic Disturbances. *Publications of the Astronomical Society of Japan*, 22:341–+, 1970.

G. Verth and R. Erdélyi. Effect of longitudinal magnetic and density inhomogeneity on transversal coronal loop oscillations. *Astronomy & Astrophysics*, 486:1015–1022, August 2008. doi: 10.1051/0004-6361:200809626.

H. Weng and K.-M. Lau. Wavelets, Period Doubling, and Time-Frequency Localization with Application to Organization of Convection over the Tropical Western Pacific. *Journal of Atmospheric Sciences*, 51:2523–2541, September 1994. doi: 10.1175/1520-0469(1994)051¡2523:WPDATL¿2.0.CO;2.

V. V. Zaitsev and A. V. Stepanov. On the Origin of the Hard X-Ray Pulsations during Solar Flares. *Soviet Astronomy Letters*, 8:132, April 1982.

V. V. Zaitsev, A. G. Kislyakov, A. V. Stepanov, B. Kliem, and E. Furst. Pulsating Microwave Emission from the Star AD Leo. *Astronomy Letters*, 30:319–324, May 2004. doi: 10.1134/1.1738154.